

Cardiac regeneration in ischaemic cardiomyopathy

Cell-free cardiac regeneration in ischaemic cardiomyopathy: The paracrine regenerative effect of the secretome of apoptotic peripheral blood mononuclear cells (APOSEC)

Doctoral thesis at the Medical University of Vienna

for obtaining the academic degree

Doctor of Philosophy

Submitted by

Dipl.-Ing. Dr.med.univ. Noemi Pavo

Supervisor:

Univ.-Prof. Dr.med.univ. Hendrik Jan Ankersmit, MBA
Department of Thoracic Surgery
Christian Doppler Laboratory for Cardiac and
Thoracic Diagnosis and Regeneration
Medical University of Vienna
Währinger Gürtel 18-20
1090 Vienna, Austria

Vienna, 03/2016

WE NEVER ADVANCE ONE STEP BEYOND OURSELVES

David Hume

TABLE OF CONTENTS

1. Declaration	iv
2. List of Figures	v
3. List of Tables.....	vi
4. Abstract.....	vii
5. Zusammenfassung	ix
6. Publications arising from this thesis.....	xi
7. Abbreviations	xii
8. Acknowledgments.....	xiv
1. INTRODUCTION	1
1.1. Concept of cardiac tissue regeneration	1
1.2. Cell-based cardiac tissue regeneration	2
1.2.1. Cell types and clinical cardiac regeneration studies	2
1.2.2. Controversies in cell-based cardiac repair mechanisms.....	6
1.2.3. Recent disappointing results of cardiac cell–based clinical therapies and meta-analyses.....	7
1.3. Turning from the concept from cell-based regeneration to the paracrine hypothesis.....	10
1.3.1. Secretome of living cells in cardiac repair	10
1.3.2. Secretome of apoptotic cells in cardiac repair	17
1.3.3. Paracrine regenerative effect of the secretome of apoptotic peripheral blood mononuclear cells (APOSEC)	18
1.3.3.a. Mechanisms of action of APOSEC	18
1.3.3.b. Cardiac regenerative effect of APOSEC in rodents and pigs with acute MI	25
2. AIM.....	30
A. Methodological study: the NOGA endocardial mapping system	30
B. Cardiac regeneration using APOSEC in chronic myocardial infarction.....	30
3. MATERIALS AND METHODS	31
3.1. Experimental chronic left ventricular dysfunction post MI	31
3.2. cMRI-LE acquisitions.....	31
3.3. Analysis and visualization of cMRI images.....	32
3.4. NOGA® electroanatomical mapping of the LV.....	33
3.5. Evaluation of the NOGA® maps	34
3.6. Overlap ratio.....	40
3.7. Histology for the NOGA-MRI study.....	42
3.8. Generation of cell culture medium from irradiated porcine PBMC for in vivo experiments (APOSEC)	42
3.9. Percutaneous intramyocardial delivery of APOSEC or medium solution using 3D NOGA guidance	43
3.10. Cardiac magnetic resonance imaging (cMRI) for area at risk, microvascular obstruction 3 days post-AMI	43
3.11. LV hemodynamic measurements	43
3.12. Myocardial viability, infarct transmuralty and regional functional assessment by NOGA	43
3.13. Histology for the APOSEC study	44
3.14. Gene expression analysis using RNA microarrays and real time PCR (rtPCR).....	44

3.15. RNA microarrays.....	44
3.16. rtPCR of selected genes.....	45
3.17. Statistics.....	46
4. RESULTS.....	48
4.1. COMPARISON OF NOGA ENDOCARDIAL MAPPING AND CARDIAC MAGNETIC RESONANCE IMAGING FOR DETERMINING INFARCT SIZE AND INFARCT TRANSMURALITY FOR INTRAMYOCARDIAL INJECTION THERAPY USING EXPERIMENTAL DATA	48
4.2. LONG-ACTING BENEFICIAL EFFECT OF PERCUTANEOUSLY INTRAMYOCARDIALLY DELIVERED SECRETOME OF APOPTOTIC PERIPHERAL BLOOD CELLS ON PORCINE CHRONIC ISCHEMIC LEFT VENTRICULAR DYSFUNCTION	63
5. DISCUSSION.....	89
5.1. Limitations	91
5.2. Conclusions	91
6. REFERENCES	92

1. Declaration

This work was performed at the Department of Surgery (Medical University of Vienna) in cooperation with the Department of Cardiology (Medical University of Vienna). The large animal experiments were performed at the University of Kaposvar, Hungary (Dr Petrás Z, Dr Petneházy Ö). The porcine cardiac magnetic resonance imaging and the mathematical comparison with the NOGA endocardial mapping polar maps was analyzed by the collaborator from the Radiology Department of the Medical University of Vienna (Dr Jakab A). The intramyocardial injection study was performed in collaboration with the University Hospital of Zürich (Dr Emmert M, Wolint P and Prof. Hoerstrup S). The in vitro work was performed in the histology laboratory of Prof. Gyöngyösi M (Department of Cardiology), and in cooperation with Michael Mildner (Department of Dermatology), Medical University of Vienna. The gene array and associated bioinformatic analysis was done in cooperation with Dr Pils D, Department of Obstetrics and Gynecology, Comprehensive Cancer Center (CCC), Medical University of Vienna. The APOSEC was produced under the supervision of HJ Ankersmit and W Sipos under non-GLP conditions at the Surgical Research Laboratory. The studies were designed by DI Dr med Noemi Pavo, under the supervision of Hendrik Jan Ankersmit (Department of Surgery, Medical University of Vienna). Similarly, the analysis of data, interpretation and the writing of the papers was done by DI Dr med Noemi Pavo, with the supervision of Hendrik Jan Ankersmit (Department of Surgery, Medical University of Vienna).

2. List of Figures

Figure 1. Cell types and delivery routes in human stem cell clinical trials.

Figure 2. In vitro bioluminescence imaging of tissues of a pig, who received intracoronary delivery of porcine MSCs transfected with luciferase.

Figure 3. Meta-Analysis of Cell-based CaRdiac studies: cardiac and cerebrovascular events.

Figure 4. Meta-Analysis of Cell-based CaRdiac studies: ejection fraction.

Figure 5. The evolution of the stem cell theory for heart failure.

Figure 6. Secretome of MSCs.

Figure 7. Secretome of MSCs and their regenerative function

Figure 8. Summary of miRNAs in cardiovascular repair mechanisms mediated by MSCs.

Figure 9. . Role of circulating miRNAs and long noncoding RNAs in cardiovascular diseases.

Figure 10. Summary of paracrine factors used in clinical trials.

Figure 11. The dying cell hypothesis.

Figure 12. Cellular response of PBMC to irradiation.

Figure 13. Effect of irradiated and non-irradiated PBMC on rat myocardial infarction.

Figure 14. Content of secretome of living and apoptotic PBMCs.

Figure 15. Changes in PBMC transcriptome following irradiation at 2h, 4h and 20h of cultivation.

Figure 16. Ionizing radiation induces the release of microparticles.

Figure 17. Membrane array showing up-regulated proteins in response to radiation exposure.

Figure 18. Time-dependent induction of release of cytoprotective substances of human cardiomyocytes after co-culture with APOSEC.

Figure 19. Effect of Aposec administered in the acute phase of myocardial infarction in a closed-chest reperfused myocardial infarction translational model.

Figure 20. Decrease of microvascular obstruction (MVO) after administration of APOSEC in the acute phase of MI

Figure 21. Time-dependent decrease of circulating platelet activation markers measured in plasma of APOSEC or medium control treated pigs.

Figure 22. Antiplatelet activity of APOSEC proven by light transmittance aggregometry.

Figure 23. Vasodilatory effect of APOSEC.

Figure 24. NOGA® endocardial mapping and cardiac magnetic resonance imaging (cMRI) of a pig with chronic myocardial ischemia.

Figure 25. Magnet resonance imaging-derived NOGA® bipolar threshold values for infarct transmural.

Figure 26. Determination of the bipolar voltage (BiPV) cut-off value for calculating the transmural and non-transmural infarct size using unipolar voltage values.

Figure 27. Schematic illustration of the planimetric calculation of the size of the infarct core and the size of the border zone of the infarction with decreased viability in the NOGA® endocardial mapping.

Figure 28. Schematic illustration of the planimetric calculation of the transmural and non-transmural infarct sizes as shown in polar maps from cardiac magnetic resonance imaging (cMRI) and NOGA® endocardial mapping.

Figure 29. Calculation of the overlapping ratio of the transmural plus the non-transmural infarction by cardiac magnetic resonance imaging (cMRI) and NOGA® endocardial mapping.

3. List of Tables

Table 1. NOGA® endocardial unipolar and bipolar map-derived cut-off values.

Table 2. List of the primers used for rtPCR.

4. Abstract

The expectation 10 years ago was that stem or progenitor cell research would lead us to human myocardium regeneration that might ultimately repair or rescue injured myocardium and ischemic damage and enhance vascular density. Since that first burst of anticipation, however, evidence has shown that the cells hold only modest promise therapeutically and that using them as a basis for tissue regeneration involves greater-than-expected complexity. The likeliest mechanism underlying the effect of myocardial transplanted cells in cardiac regeneration is paracrine signaling, involving mesenchymal stem cells known to release growth factors, cytokines, and other small molecules. One class of cells, in addition to stem cells, that produces a large array of paracrine factors is the apoptotic peripheral blood mononuclear cells (PBMCs). We have shown that the factors these cells produce can be cytoprotective, anti-inflammatory, or antithrombotic and even have vasodilatory effects. These discoveries suggest that treatment relying on cell therapy might make way for cell-free approaches that target angiogenesis and protecting tissues subjected to ischemic injury, as occurs with myocardial infarction (MI).

In fact, our group has shown that infusing the secretome of apoptotic PBMCs, called the APOSEC, during acute MI results in a reduced infarct size and an increase in the measure of left ventricle (LV) function, the ejection fraction (EF). Data are lacking, however, on the effects such an injection might have in the chronic phase. To address this gap, we have used percutaneous intramyocardial APOSEC injections in the late infarction phase, relying on the same method used in regenerative cell therapy studies targeting human ischemic cardiomyopathy (iCMP).

The primary aims of this doctoral thesis were to (1) evaluate the regenerative effect of APOSEC in a translational model of chronic ischemic LV dysfunction and demonstrate this effect in cardioprotection and inhibition of cardiac remodeling; (2) explore the cardioprotective effect of APOSEC using gene expression analysis in iCMP; and (3) validate the diagnostic value of a percutaneous intramyocardial navigation system that has been used for cell-based regeneration in iCMP, comparing it to a magnetic resonance imaging (MRI) approach (cardiac MRI; cMRI) with late enhancement (cMRI+LE).

To achieve these aims, we developed a model of chronic iCMP in pigs, inducing closed-chest reperfused MI and randomizing the animals at day 30 to porcine APOSEC or control injection (medium solution), administered intramyocardially into the border zone of the MI under three-dimensional (3D) NOGA guidance. Thirty days later (at 60 days), we performed diagnostic NOGA to assess the viability of the myocardium and also performed cMRI+LE.

For evaluation at the molecular level, we used microarray analysis to profile the gene expression of three separate areas – the border zone of the infarct, the infarct core, and the normal myocardium – confirming the results using quantitative real-time PCR.

Compared to controls, the APOSEC injection was associated with a decrease in infarct size, improved cardiac index, and improved myocardial viability. We found that in areas exposed to APOSEC, caspase-1, tumor necrosis factor, and other inflammation-related genes were downregulated, confirming APOSEC-related downregulation of caspase genes and upregulated myogenic factor Mefc2 by RT-PCR in pigs.

Overall, under APOSEC treatment, increased MEF2c expression and reduced caspase were both associated with a decrease in the size of the infarct and with an improvement in cardiac function. We also confirmed persistence of these changes in gene expression at one month after treatment, demonstrating that the effects of this cell-free paracrine factor therapy were long-lasting. Furthermore, we showed that the 2D NOGA unipolar voltage mapping results significantly correlated with 3D MRI results for infarct measurement and that the mean difference in left ventricular surface between the two was 2.82%. With the combination of unipolar with bipolar voltage maps, the endocardial mapping was comparable to cMRI-LE for accurately characterizing the zone of interest for intramyocardial therapy.

Thus, using a translational model of iCMP, we have demonstrated that cell-free therapy targeting regeneration for chronic ischemic LV dysfunction can be efficacious when applied intramyocardially via percutaneous injection, relying on 3D imaging to navigate appropriately to the target area.

5. Zusammenfassung

Vor einem Jahrzehnt versprach sich die Forschung von Stammzellen bzw. deren Vorläuferzellen menschliches Myokard regenerieren um dadurch ischämisch geschädigtes Myokard reparieren zu können sowie die Vaskularisierung verbessern zu können. Jedoch sprechen die bis dato gesammelten Ergebnisse dafür, dass der therapeutische Erfolg lediglich mäßig ist und in der Geweberegeneration viel komplexere Mechanismen eine Rolle spielen als nur zell-basierte Repairmechanismen. In den letzten Jahren traten parakrine Effekte von ins Myokard transplantierten Zellen in den Vordergrund, da diese als wahrscheinlichste Erklärung für den kardioregenerativen Effekt der Zelltherapie gelten. Bei mesenchymalen Stammzellen konnte gezeigt werden, dass sie eine Vielzahl an parakrinen Substanzen produzieren und die Freisetzung von hunderten verschiedenen Wachstumsfaktoren, Zytokinen und anderen kleinen Molekülen mediiieren. Unsere Gruppe hat gezeigt, dass abgesehen von lebenden Stammzellen, auch apoptotische periphere mononukleäre Zellen (PBMC) eine Vielfalt von parakrinen Faktoren mit regenerativen Eigenschaften produzieren, mit antithrombotischen, vasodilatatorischen, entzündungshemmenden und zellprotektiven Effekten. Demnach könnte diese zell-freie Therapie die bisher etablierte Zelltherapie ersetzen mit dem Ziel einer therapeutischen Gefäßneubildung und Gewebeprotektion im Rahmen einer ischämischen Schädigung wie beim Myokardinfarkt. Unsere Gruppe konnte in früheren Untersuchungen zeigen, dass im Großtiermodell die intravenöse Verabreichung des Sekretoms von apoptotischen PBMC (APOSEC) im akuten Myokardinfarkt die Infarktgröße reduzieren und die linksventrikuläre Auswurfsfraktion (LVEF) erhöhen kann. Allerdings gab es bisher keine Daten über den Effekt von APOSEC in der chronischen Phase nach Myokardischämie. Daher injizierten wir APOSEC perkutan in einer späten Phase des Myokardinfarkts intramyokardial, eine Methode die bereits in der humanen Regenerationsmedizin zur Behandlung der ischämischen Kardiomyopathie etabliert wurde.

Die primäre Fragestellung dieser Arbeit war es 1. Beweise für den regenerativen Effekt von APOSEC in einem translationalen Model der chronischen linkventrikulären Dysfunktion zu gewinnen und den kardioprotektiven Effekt von APOSEC hinsichtlich Prävention von myokardialem adverse Remodelling zu evaluieren; 2. den kardioprotektiven Effekt von APOSEC auf Ebene der Genexpression in ischämischer Kardiomyopathie zu untersuchen; und 3. die diagnostische Qualität des sogenannten perkutanen intramyokardialen Navigationssystems (NOGA), ein System, welches im Rahmen der humanen zell-basierte Regenerationstherapien bei ischämischer Kardiomyopathie bereits klinisch zum Einsatz kommt, durch Vergleich mit der kardialen Magnetresonanzuntersuchung mit late enhancement (MRT+LE) zu quantifizieren.

Unsere Gruppe entwickelte ein translationales Modell der chronisch ischämischen Kardiomyopathie durch Induktion eines Myokardinfarktes mit anschließender Reperfusion bei geschlossenem Brustkorb in Schweinen. Nach 30 Tagen wurden die Versuchstiere in zwei Gruppen randomisiert und anschließend intramyokardial entweder APOSEC oder physiologische Lösung in die Infarktgrenzzone durch NOGA Steuerung injiziert. Am 60. Tag wurden sowohl eine kardiale MRT-LE als auch eine NOGA Untersuchung (zur Bestimmung der myokardialen Viabilität) durchgeführt. Weiters wurde eine Genexpressionanalyse mittels microarray in Gewebeproben aus der Infarktzone, der Infarktgrenzzone und dem normalem Myokard durchgeführt und durch quantitative real-time PCR (rtPCR) bestätigt. Wir konnten zeigen, dass die Injektion von APOSEC verglichen mit Kontrollen die Infarktgröße signifikant reduzieren sowie den Cardiac Index und myokardiale Viabilität signifikant erhöhen konnte. Die Analyse des Transkriptoms zeigte eine signifikante Downregulation von Caspase-1, Tumornekrosefaktor- α und anderen pro-inflammatorischen Molekülen in den mit APOSEC behandelten Myokardregionen. Die rtPCR-Untersuchung ergab eine höhere Expression von Mef2c und eine niedrigere von Caspase-1 in APOSEC behandelten Tieren. Zusammengefasst sind eine Hochregulation von Mef2c und eine Downregulation von Caspase-1 assoziiert mit einer reduzierten Infarktgröße und verbesserten kardialen Funktion in APOSEC-behandelten Tieren. Die veränderte Genexpression auch nach einem Monat beweist den langanhaltenden Effekt einer zell-freien Therapie mit parakrinen Faktoren. Beim Vergleich der diagnostischen Qualität des NOGA endokardialen Mappings mit den Ergebnissen des MRT-LE konnten wir zeigen, dass die durch 2D NOGA bestimmte Infarktgröße in der unipolaren Map signifikant mit den Ergebnissen des MRT-LEs korrelierte mit einer mittleren Differenz zwischen den beiden Methoden von 2.82%. Durch Kombination von unipolaren und bipolaren Maps, erwies sich NOGA als nützliches und genaues Werkzeug vergleichbar mit MRT-LE um die Zielzone für eine intramyokardiale Therapie richtig zu identifizieren.

Unsere Ergebnisse liefern Beweise für die Effektivität der zell-freien regenerativen Therapie bei chronischer ischämischer linksventrikulärer Dysfunktion durch perkutane intramyokardiale Injektion unter zu Hilfenahme des 3D Navigationssystems NOGA in einem translationalem Modell der chronisch ischämischen Kardiomyopathie.

6. *Publications arising from this thesis*

Comparison of NOGA endocardial mapping and cardiac magnetic resonance imaging for determining infarct size and infarct transmuralty for intramyocardial injection therapy using experimental data. Pavo N, Jakab A, Emmert MY, Strebinger G, Wolint P, Zimmermann M, Ankersmit HJ, Hoerstrup SP, Maurer G, Gyöngyösi M. PLoS One. 2014 Nov 19;9(11):e113245. doi: 10.1371/journal.pone.0113245. eCollection 2014.

Long-acting beneficial effect of percutaneously intramyocardially delivered secretome of apoptotic peripheral blood cells on porcine chronic ischemic left ventricular dysfunction. Pavo N, Zimmermann M, Pils D, Mildner M, Petrás Z, Petneházy Ö, Fuzik J, Jakab A, Gabriel C, Sipos W, Maurer G, Gyöngyösi M, Ankersmit HJ. Biomaterials. 2014 Apr;35(11):3541-50. doi: 10.1016/j.biomaterials.2013.12.071. Epub 2014 Jan 16.

7. Abbreviations

3D	3 dimensional
AMI	acute myocardial infarction
AMPK	AMP-activated protein kinase
APOSEC	secretome of apoptotic peripheral blood mononuclear cells
ATP	adenosin triphosphat
BiPV	bipolar voltage value
BM	bone marrow
BMSC	bone marrow (derived) stem cells
CABG	coronary artery bypass graft
CAD	coronary artery disease
CD	cluster of differentiation
CDC	cardiac derived stem cells
CLU	clusterine
cMRI	cardiac magnetic resonance imaging
CO	cardiac output
CSC	cardiac stem cells
DAPI	4',6-diamidino-2-phenylindole
DAVID	Database for Annotation, Visualization and Integrated Discovery
DNA	deoxyribonucleic acid
dP/dt	time dependent changes in LV pressure
ECG	electrocardiogram
ECM	extra-cellular matrix
EDD	end diastolic diameter
EDP	end-diastolic pressure
EDV	end diastolic volume
EF	ejection fraction
EMC	endometrial gland-derived mesenchymal cells
EPC	endothelial progenitor cells
ERC	endometrial regenerative cells
ERCC4	Excision Repair Cross-Complementation Group 4
ESV	end systolic diameter
ESV	end systolic volume
EV	extracellular membrane vesicles
FDR	false discovery rate
FUP	follow-up
FWHM	full width at half maximum
G-CSF	granulocyte colony stimulating factor
GAPDH	Glyceraldehyd-3-phosphat-Dehydrogenase
GEO	gene expression omnibus
HK	hexokinase
HPRT1	Hypoxanthin-Guanin-Phosphoribosyltransferase
I/R	ischaemia-reperfusion
IL-10	interleukin-10
IPC	ischaemic preconditioning
IPD	individual patient data
IPostC	Ischaemic postconditioning
IVRT	isovolumetric relaxation time

LAD	left anterior descending coronary artery
LE	late enhancement
LLS	local linear shortening
LV	left ventricular
MEF	myocyte enhanced factor
MI	myocardial infarction
miRNA	microRNA
MMP	matrix metalloproteinase
MNC	mononuclear cells
MP	microparticles
MPC	mesenchymal precursor cells
MRI	magnetic resonance imaging
mRNA	messenger RNA
MSC	mesenchymal stem cells
MVO	microvascular obstruction
NADH	nicotinamiddinucleotid-dehydrogenase
NGS	next generation sequencing
PBMC	peripheral blood mononuclear cells
PCA	principal component analysis
PCI	percutaneous coronary intervention
PCR	polymerase chain reaction
PPIA	Peptidylprolyl Isomerase A
RNA	ribonucleic acid
ROC	receiver operator characteristics
ROS	reactive oxygen species
rtPCR	real-time PCR
RV	right ventricular
SD	standard deviation
SDF-1	stromal cell-derived factor-1
SI	signal intensity
SPIA	signalling pathway impact analysis
SWOP	second window of protection
TE	echo time
TGF	transforming growth factor
TIMI	thrombolysis in myocardial infarction
TLR-4	Toll-like receptor-4
TNF	tumor necrosis factor
TR	repetition time
UPV	unipolar voltage value
VIP	vasoactive intestinal peptide

8. Acknowledgments

First and foremost I would like to thank my advisor Hendrik Ian Ankersmit, Head of the Christian Doppler Laboratory for Cardiac and Thoracic Diagnosis & Regeneration. It has been an honour to be his Ph.D. student. The joy and enthusiasm he has for his research was contagious and motivational not only for me but also for his whole team.

I thank the members of my Ph.D. committee Michael Gottsauner-Wolf and Georg Goliash for the valuable discussions and linking basic research ideas to clinical practice.

I would also like to thank the members of the group of Prof. Gyöngyösi who have contributed immensely to my personal and professional development at The Medical University of Vienna. The group has been a source of friendships as well as good advice and collaborations.

The animal studies discussed in this dissertation would not have been possible without the skilled and courageous team of the Veterinary Medicine University of Kaposvár. I enjoyed the collaboration and will always remember the late night sessions at the institution.

I gratefully acknowledge the ÖKG for funding the grant that made my Ph.D. work possible.

Lastly, I would like to thank my family for their love and encouragement. For my parents and grandparents who raised me with a love of science and supported me in all my pursuits.

1. INTRODUCTION

Ten years ago, the expectation arose that therapies with stem cells or progenitor cells would aid in myocardial regeneration to rebuild injured areas of myocardium, ameliorate myocyte damage from ischemia, and increase vascular density. By the second decade of this century, though, this area of research has yielded only minimal successes and brought the realization that achieving cell-based tissue regeneration promises to be far more complicated than anticipated. In the meantime, the search for cells that will be effective has continued, with trials given to native cardiac cells, cells from adipose tissue, or modified progenitor/stem cells, all with the goal of increasing and retaining in the myocardium the population of cells that engage in reparative processes. Delivery of stem cells for acute myocardial infarction (MI, AMI) or ischemic cardiomyopathy (iCMP) has generally been attempted by intracoronary or percutaneous intramyocardial injection, although other, less effective methods have been tried, including surgery or injection into peripheral veins or the coronary sinus.

Trials for cardiac regeneration have been small because of the difficulty enrolling patients within the necessary time period. For this reason, efforts have been made to perform meta-analyses of results from cell-based studies involving human cardiac cell therapies. The results of these analyses indicate only modest effects, with an average global left ventricular (LV) ejection fraction (EF) increase of 0.9 to 6.1%. Among the studies that have involved long-term follow-up, half have reported that any detected benefits wane with time.

While efforts continue to maximize the benefits and administration routes of cell-based therapy, new approaches under investigation have shifted away from cells and toward the components involved in their paracrine effects in promoting regeneration of injured cardiac tissue in humans.¹

1.1. Concept of cardiac tissue regeneration

In the area of cardiovascular disease, research has led to considerable improvements since the mid-20th century, as shown in the decreasing incidence of AMI and cardiovascular-related mortality, adverse events, and hospitalization. Prevention approaches and invasive (percutaneous coronary) and non-invasive (anti-thrombotic) interventions have alike contributed to some of these declines, all targeting restoration and maintenance of functional coronary arteries. Having innovated thus far to manage acute problems, the field of research

has pivoted to address chronic disease, including heart failure, focusing on regeneration of injured cardiac tissue following ischemia.²

Driving interest in cardiac regeneration are findings that multipotent cells of various tissue origin can differentiate into cardiomyocytes or cells carrying surface markers of early cardiomyocytes.^{3,4} Even more intriguing, transplanted hearts^{5,6} and myocardium bearing ischemic injury⁷ appear to accumulate bone marrow (BM)-derived stem cells and stem cells from the peripheral blood, in addition to containing mitotic myocytes. These results, confirmed via confocal microscopy, hint at an ability of cardiac tissue to regenerate itself, although at a low rate of cell division.^{8,9}

1.2. Cell-based cardiac tissue regeneration

1.2.1. Cell types and clinical cardiac regeneration studies

Almost two decades ago, the finding of early commitment cells with the ability to form myocytes¹⁰ triggered an intensive search for regenerative cells in the cardiovascular system. Undifferentiated myoblasts, typically existing as satellite cells, showed the ability to differentiate into cardiac-like cardiomyocytes. Because these cells led to successful cardiomyoplasty using cell replacement,⁴ research then followed involving administration of autologous myoblasts from skeletal muscle either surgically¹¹ or percutaneously into the myocardium.^{12,13} The cells could not, however, exhibit an intrinsic contractile rhythm or become a functional part of the surrounding myocardium; thus, they were hypothesized to exert their reparative effects by some other action.¹⁴

In the early 2000s, Orlic et al. and Anversa et al. characterized several BM cell clusters (e.g., Lin-/c-kit+) capable of myogenic differentiation and expression of transcription factors, such as myocyte enhanced factor (MEF), GATA4, and Nkx2.5.¹⁵⁻¹⁷ They showed that these cells could differentiate into smooth muscle and endothelial cells in a mouse MI model (15). Later work revealed that stem cells derived from BM (endothelial progenitors, angioblasts, CD34+ cells) also had angiogenic properties and could trigger new formation of blood vessels in the ischemia-damaged myocardium.¹⁶ Extending these findings, the intravenous administration of angioblasts derived from human BM into the heart in the mouse infarction model also resulted in neovascularization and an improvement in heart function.¹⁸ In addition, immature hematopoietic progenitor cells (side population cells that are Lin-/c-kit+/Sca-1+) also can differentiate into a myogenic lineage.¹⁹

The more committed BM-originated hematopoietic stem cells are multipotent cells that give rise to the myeloid and lymphoid blood cell types, characterized by their small size and lack of lineage marker (i.e., Lin⁻), but expressing c-kit, CD34⁺, and CD133⁺. This mixed population of cells can elicit differentiation into an early stage of the myogenic lineage, suggesting some potential to regenerate heart muscle. Endothelial progenitor cells (EPCs) of BM origin and CD45⁺/CD34⁺, on the other hand, do not have this capacity and instead lead to regeneration of endothelial and vascular smooth muscle cells.^{3,9} The same EPCs cocultured with rat cardiomyocytes, however, can differentiate into functional cardiomyocytes, suggesting some influence of paracrine factors.^{20,21}

These results triggered the initial clinical studies of mononuclear cells (MNCs) originating from the BM, assessing their capacity for repair in patients who had recently experienced AMI.²² After Strauer et al.'s initial clinical studies, results were published from randomized trials using unselected BM MNCs or EPCs (REPAIR-AMI, TOPCARE-AMI, respectively) in patients with AMI²³⁻³⁰ or iCMP (TOPCARE-CHD).³¹

Following on these trials came efforts to improve efficacy. Studies involving specific CD34⁺ or CD34⁺/CD133⁺ cells of BM origin, delivered via intracoronary injection in participants with AMI, were moderately successful (REGENT³², AMR-001³³). A phase 3 trial used G-CSF-mediated CD34⁺ cells (a selected population) mobilized and delivered percutaneously into the myocardium in iCMP patients randomized to the treatment.³⁴

Most initial investigations relied on mixed unselected populations of BM-MNCs because of a lack of information about which cell type would be best suited (Figure 1). Most such cells are lymphocytes, but other types can be present, including some that should be excluded from areas of myocardial injury, such as osteoblasts, pericytes, and pre-adipocytes. In fact, in these mixed populations, the target cell population, the hematopoietic stem cells, make up only about 1% of BM cells, leaving the long-term success of this approach somewhat doubtful.³⁵

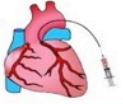
Stem cell origin/delivery route		Intracoronary	Direct intramyocardial	Percutaneous intramyocardial	Coronary sinus
					
BM-origin SC	 Mononuclear	Strauer et al, Topcare-AMI, Repair-AMI, BOOST, IACT, TCT-STAMI, ASTAMI, FINCELL CARDIAC, DanCell-CHF, BONAMI, CELLWAVE, HEBE, LATE TIME, MySTAR,	NA	PROTECT-CAD, MYSTAR, ALSTER-Stem Cell (ongoing)	NA
	CD 34	REGENT	NA	Losordo et al, RENEW (ongoing)	NA
	CD 133	Bartunek et al, COMPARE AMI, SELECT AMI (ongoing)	IMPACT-CABG	NA	NA
	 Mesenchymal	Chen et al, RELIEF (ongoing)	PROMETHEUS	POSEIDON, MSC-HF, TAC—HFT (ongoing)	NA
 Adipose-derived stem cells	ADVANCE, APOLLO (ongoing)	NA	PRECISE	NA	
 Endometrial regenerative cells		NA	NA	RECOVER-ERC (ongoing)	
 Circulating peripheral blood endothelial progenitor cells G-CSF mobilized	Choi et al, Li et al MAGIC TOPCARE-AMI, TOPCARE-CHD	NA	NA	NA	
 Multipotent Cardiac Stem cells	SCIPIO	NA	NA	NA	
 Cardiosphere-derived cells	CADUCEUS, ALLSTAR (ongoing)	NA	NA	NA	
 Myoblasts	NA	NA	CauSMIC, Smits et al	NA	
 Phenotypically modified	NA	NA	C-CURE	NA	
 Allogenic	NA	NA	POSEIDON	NA	

Figure 1. Clinical trials for various human stem cell populations and subtypes, including route of administration (from Pavo et al. JMCC 2014)¹.

Given these findings, the modest clinical results with BM-MNCs, and the first reported negative outcome trials, the search has continued for cells and techniques that might show more promise, including mesenchymal stem cells (MSCs) of BM origin, their precursors, and cardiac-derived stem cells.

In a set of *in vitro* studies, Fukuda et al. demonstrated formation of myotube-like structures by fibroblast-like mouse BM stromal cells with cardiomyogenic capacity, and these cells also gave rise to cardiomyocytes.³⁶ These results led to trials of intracoronary injection³⁷ or percutaneous intramyocardial injection of BM-derived MSCs into iCMP patients with reduced EF. In one trial, the TAC-HFT, patients with iCMP who received BM-MNC or BM-MS

transendocardial injections had a significant decrease in the size of their infarcts and improved regional function compared to placebo, but only with BM-MSCs.³⁸ In further promising MSC-related findings, administering adult human allogeneic MSCs (e.g., Provacel) intravenously resulted in increased EF for patients with anterior AMI, an improved global symptom score, and a reversed remodeling process versus results with placebo, and had a good safety profile.³⁹ Another study, POSEIDON (NCT01087996), also addressed MSC efficacy, comparing human allogeneic and autologous cells administered percutaneously and transendocardially in iCMP patients. Regarding safety, the rate of immunological reactions was low, and remodeling was reversed, although EF did not increase significantly.⁴⁰ However, in the SEED-MSC study, which included patients who had experienced AMI recently, intracoronary delivery of autologous MSCs was well tolerated and did lead to a moderately increased EF.⁴¹

Another mesenchymal cell type derived from the BM is the mesenchymal precursor cell, which in turn can give rise to stromal and multipotent cells, the latter of which can differentiate into cardiomyocytes.^{38,42}

Several other clinical trials have tested other sources of BM-MSCs as a way to resolve the issue of limited cell numbers. Cell types being evaluated have included adipose-derived stem cells,⁴³ which are under investigation in the APOLLO,⁴⁴ ATHENA (NCT01556022), PRECISE (NCT00426868), and ADVANCE (NCT01216995) trials. Other potential sources of cardiomyogenic cells that exhibit MSC properties have been identified, including endometrial regenerative cells, mesenchymal cells derived from menstrual blood, and those derived from endometrium.⁴⁵ These cells express surface markers such as CD29 and CD105 that suggest MSC properties and can fire cardiomyocyte-like action potentials.

The discovery of the cardiac stem cells (CSCs)^{9,46,47} and cardiosphere-derived cells (CDCs)^{48,49} that were positive for c-kit and clonogenic, along with being self-renewing, led to the initiation of the two phase I trials, SCIPIO⁵⁰ and CADUCEUS,⁵¹ investigating the effect of these cells in iCMP and AMI patients. The SCIPIO results showed that intracoronary infusion of autologous CSCs led to better LVEF in a small subset of patients,⁵⁰ but CADUCEUS yielded no effects on EF although scar dynamics and the ability of the regenerative muscle to distend did improve.⁵¹

1.2.2. Controversies in cell-based cardiac repair mechanisms

Despite some promising pre-clinical results for the ability of stem cells to trigger regeneration, clinical trials have been less successful following initial reports of the potential of several cell types to differentiate into cardiac muscle-like cells.¹⁰ Those studies led to further efforts, which yielded mixed findings and generated considerable controversy. Robbins et al., for example, could find no examples of BM cell differentiation into cardiomyocytes; instead, candidates such as hematopoietic cells simply matured into hematopoietic lineages.⁵² Martin et al.⁵³ similarly found no indication that human endothelial progenitor cells could differentiate into cardiac cells under culture with rat cardiomyocytes, and yet another group, Murray et al., examining hematopoietic stem cells (Lin-/c-kit+), found no capacity for differentiation into cardiac myocytes.⁵⁴ With yet more disappointing results, Jacobsen et al. reported no success mobilizing hematopoietic progenitors or differentiation into cardiomyocytes of hematopoietic cells derived from BM.⁵⁵ One proposed explanation for the expression of some cardiac markers on transplanted cells has been that existing cardiomyocytes fuse with injected stem cells,^{56,57} an idea that has been met with some skepticism.⁵⁸⁻⁶⁰

Making the transformation from a totipotent embryonic cell to a precursor of cardiac muscle and then differentiating into a cardiomyocyte requires a stepwise, time-constrained process of signaling, with cardiac-related transcription factors and cytokines serving as the master switches.^{61,62} When stem cells are administered in the hearts of patients, they do not readily differentiate at high rates, suggesting that some other mechanism is responsible for their effects. One possibility is that paracrine signaling leads to the relatively modest improvement in iCMP patients who undergo cell transplantation. Transplanted stem cells are reported to release paracrine factors that both activate *in situ* cardiac progenitor and stem cells and attract them to the site of ischemic injury, leading to a reprogramming of other cardiac cells at the site.^{63,64}

Also interfering with the success of therapeutic stem cell injection is the fact that most of the cells appear to migrate out of the target tissue, away from the myocardium. Indeed, according to Penicka et al.,^{65,66} within hours of administration, almost all of the cells have made it to the liver, lung, lymph nodes, BM, and spleen (Figure 2), with only 5% and then 1% remaining in the myocardium at 2 and 18 h following delivery.⁶⁷

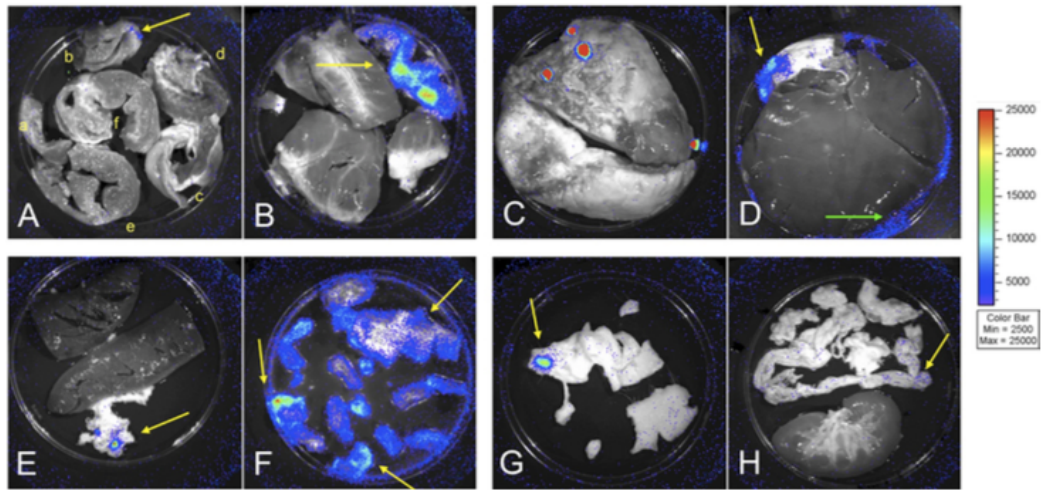


Figure 2. *In vitro* bioluminescence imaging of tissues of a pig that received an intracoronary delivery of porcine MSCs transfected with luciferase.

As seen in (A), at 3 h following administration, few cells remain in the myocardium (yellow arrow) whereas many cells accumulate in (B) the pericardial space, (C) lung, (D) portal lymph nodes, (E, H) mesenteric lymph nodes, (G) skin, and (F) BM (adopted from Gyöngyösi et al. JACC Imaging 2010).⁶⁸

1.2.3. Recent disappointing results of cardiac cell-based clinical therapies and meta-analyses

As noted, clinical trials with cell therapy have not borne out the promise of the pre-clinical studies, in part because of unavoidable differences between the two, including open chest AMI in animals vs reperfused AMI in humans, divergent delivery routes (percutaneous or open chest in rodents vs intracoronary or intramyocardial in humans), cell origin (allogeneic/heterogeneic in rodents that may be genetically modified or immune suppressed vs autologous in people), and cell numbers relative to size.

After the first results with the surgical, direct intramyocardial delivery of myoblasts⁶⁹⁻⁷¹ and BM-MNCs,⁷² Strauer et al.²² published very promising results of clinical signs of human cardiac repair after using an intracoronary route; however, questions have arisen around their findings.⁷³ Furthermore, this early enthusiasm was tempered somewhat by the first published negative results,^{74,75} which led to an entirely new set of questions and shifted the focus back from bedside to bench.

Trials of cardiac cell therapies have encountered a number of obstacles, including slow

patient recruitment in a relevant time frame. One attempt to resolve this problem has been collecting the available data for meta-analyses to achieve enough data points for statistical power. In total, these analyses have processed data from 50 studies for at most 2652 patients (of whom 447 were participants in three of Strauer et al.'s highly criticized studies, representing almost 17% of the entire pool). From the pooled data, the average EF increase with cell therapy has been from 0.9% to 6.1%,⁷⁶⁻⁸⁹ with variability across studies in population size, design, and method for evaluating EF. In all, little benefit of the therapy has been reported in terms of survival or cardiovascular-related adverse events, but the largest of these meta-analyses has cited persistent improvement in clinical endpoints and LV function.⁸⁵ In contrast, though, a recent meta-analysis that included 30 studies and 2037 patients failed to confirm LVEF increase when evaluating LV function based on cMRI measurement.⁹⁰ As is standard, both meta-analyses used published datasets, and the included trials had significant differences from one another.

A drawback of these meta-analyses is that the studies they included may have contained errors or even been retracted,⁸⁶ and it is always possible that relevant studies were excluded for reporting median values with non-normally distributed data sets. Another sort of meta-analysis based on individual patient data (IPD) may address this drawback by using unique definitions and transparent data sets to analyze subgroups for features that may be associated with cell therapy effectiveness.

The initial IPD meta-analysis was ACCRUE (Meta-Analysis of Cell-based CaRdiac studies), which evaluated 12 randomized studies of intracoronary cell administration in patients with recent AMI, for a total of 1252 IPDs.⁹¹ Based on the ACCRUE findings, **cell therapy had no effect** on LVEF or clinical outcomes, and no predictors or patient characteristics associated with cell therapy benefit.

Editorials addressing this article appeared in the same issue of *Circulation Research*, commenting on the negative findings of the ACCRUE meta-analysis as the “ACCRUEd evidence” of safe, but ineffective BM-derived cell therapy for cardiac repair (Figures 3 and 4).⁹²

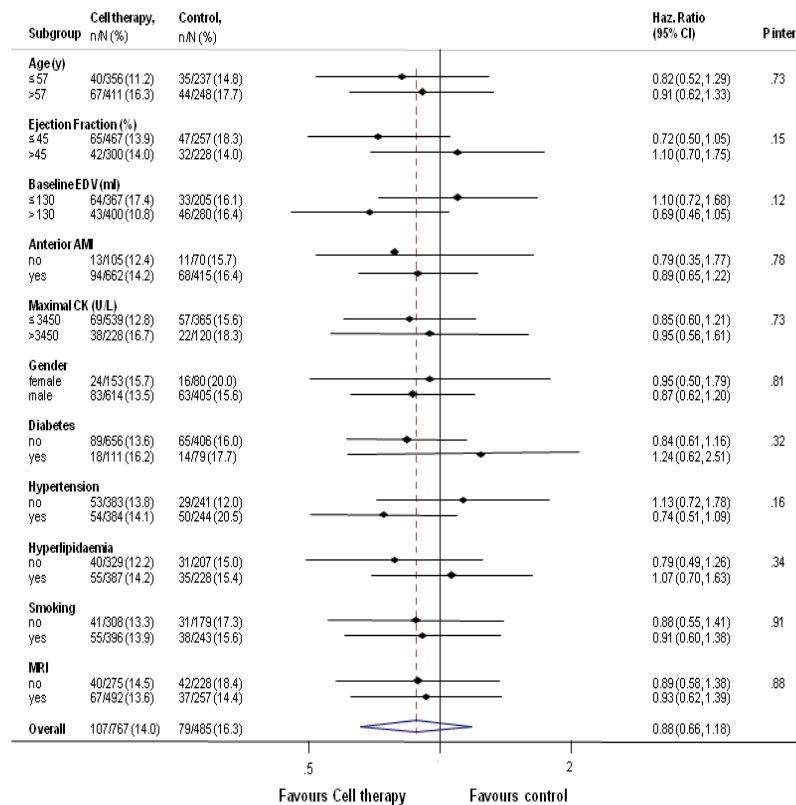


Figure 3. Cell therapy was associated with no benefit in terms of major cardiovascular- or cerebrovascular-related adverse events. No factors could influence this negative result (adopted from Gyöngyösi, Pavo et al. Circ Res 2015).⁹¹

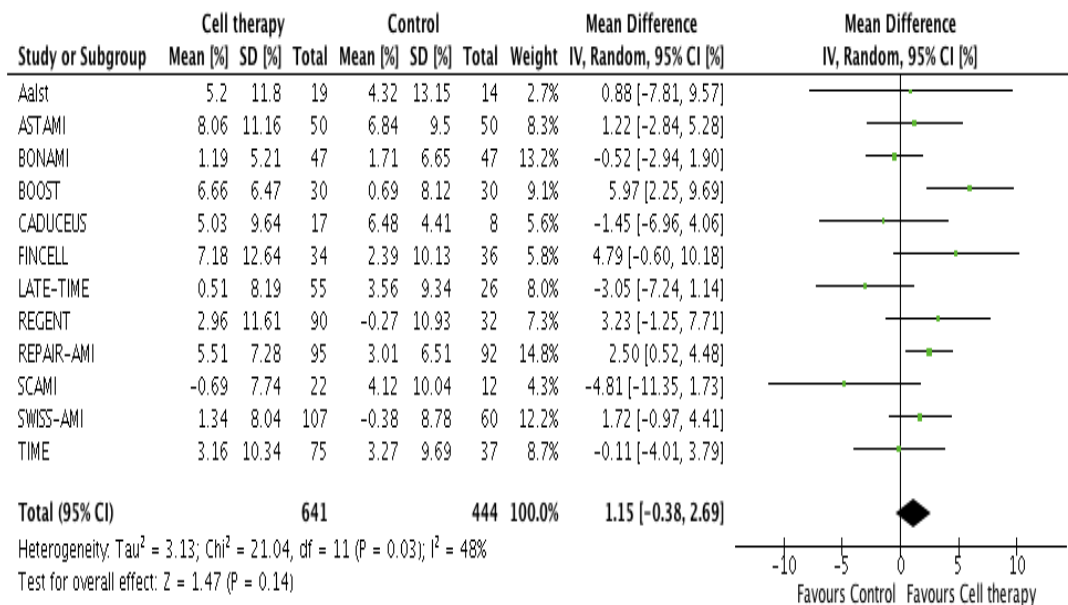


Figure 4. No benefit of cell therapy regarding changes in ejection fraction (adopted from Gyöngyösi, Pavo et al. Circ Res 2015).⁹¹

1.3. Turning from the concept from cell-based regeneration to the paracrine hypothesis

1.3.1. Secretome of living cells in cardiac repair

As noted, even though some studies showed a benefit from stem cell delivery in cardiac regeneration, only a small percentage of stem cells are delivered and retained in the heart, and their ability even to differentiate into cardiomyocytes is limited and short-lived. The hypothesized reason for the benefit in light of these findings is the secretion of paracrine-signaling factors from the administered cells that exert promotional effects on the myocardium and in vasculogenesis.

This “paracrine hypothesis” seems valid, as many stem cell types secrete molecules, like cytokines, chemokines, and growth factors, and exosomes. Several of these factors are known to improve cardiovascular function in acute and chronic cardiac tissue injury.⁹³⁻⁹⁶ The paracrine history paves the way to cardiac regeneration without cellular transplantation (cell-free therapy).⁹⁷

As shown in Figure 5, the pool of cells that acts therapeutically is now thought to do so by secreting molecules that trigger repair and regeneration, rather than by directly taking the roles themselves.⁹⁸ This proposed mechanism of repair is thought to involve several interacting pathways that work together to reduce fibrosis, promote vascular growth and remodeling, dampen inflammation, regulate survival of differentiated cells, and recruit and activate *in situ* stem and progenitor cell populations.⁹⁸

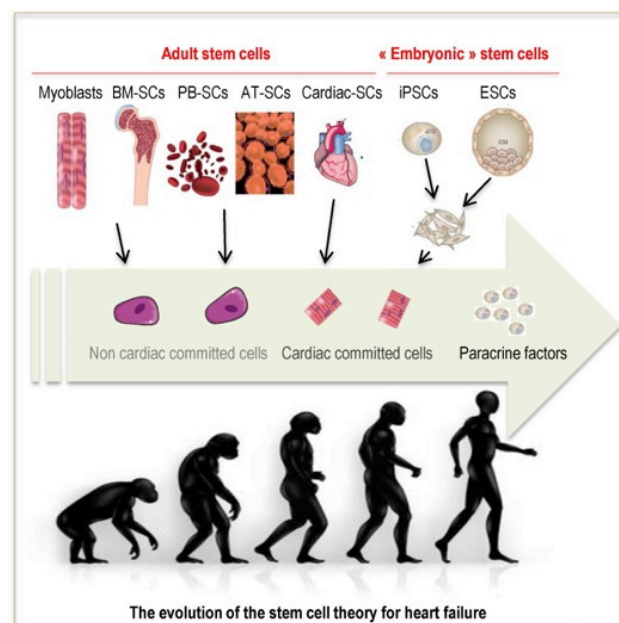


Figure 5. How the theory of stem cell benefit in heart failure has evolved (adopted from Silvestre et al. BioMedicine 2015).⁹⁸

In keeping with this newly evolved idea about stem cell therapy, MSCs are considered paracrine substance factories because of their ability to release of over hundreds of growth factors, cytokines, and other small molecules (Figure 6).

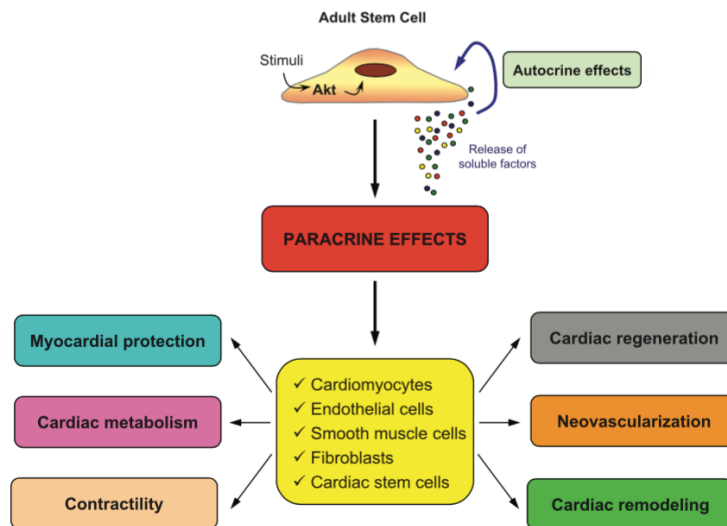


Figure 6. Secretome of MSCs with potential for cardiovascular disease treatments - including cardiac regeneration, neovascularization, negative cardiac remodeling, with consequent improvement of cardiac contractility (adopted from Gneccchi et al. Nat. Med 2005).⁹⁹

Gallina et al. summarized the factors secreted by MSCs and playing role in cardiac repair (Figure 7).¹⁰⁰

Way of secretion	Molecule	Functional role in cardiovascular repair	References	
	<i>Adrenomedullin</i>	Angiogenic and cardioprotective factor	[13]	
	<i>Angiogenin</i>	LV remodeling attenuation through vasculogenesis	[31]	
	<i>Basic fibroblast growth factor (bFGF, FGF-2)</i>	Vascular regeneration and attenuation of apoptotic pathways, leading to reduced remodeling	[32]	
	<i>CXCL12</i>	Endothelial tube formation	[33]	
	<i>Cystatin C</i>	Fibroblast chemoattraction	[34]	
	<i>Cysteine-rich angiogenic inducer (Cyr61)</i>	Angiogenesis promotion	[35]	
	<i>Dickkopf-related proteins (Dkk)</i>	JNK signaling activation, eventually resulting in cardiomyogenesis	[36]	
	<i>ECM structural proteins</i>	Fibroblast chemoattraction	[34]	
	<i>Hepatocyte growth factor (HGF)</i>	Mobilization of cardiac progenitor cells	[13]	
	<i>Hypoxic induced Akt regulated stem cell factor (HASF)</i>	Cardiomyocytes survival improvement	[37]	
	Direct secretion	<i>Insulin-like growth factor (IGF)</i>	Antiapoptotic effect, angiogenesis promotion, and activation of resident CSCs	[38]
		<i>Interleukin-1 (IL-1)</i>	Angiogenesis promotion	[39]
		<i>Interleukin-6 (IL-6)</i>	VEGF induction	[13, 39]
		<i>Leukemia inhibitory factor (LIF)</i>	Mobilization of BM-progenitor cells and cardioprotection promotion	[40]
		<i>Pigment epithelium-derived factor (PEDF)</i>	Fibroblast chemoattraction	[34]
<i>Placental growth factor (PLGF)</i>		Prevention of cell death of cardiomyocytes and endothelial cells	[13]	
<i>Secreted Frizzled Related Protein (SFRP 2)</i>		Fibrosis and apoptosis reduction, promotion of MSC self-renewal and engraftment	[41, 42]	
<i>Soluble TNFR1 (sTNFR1)</i>		Inflammatory response attenuation	[43]	
<i>Stem cell-derived factor (SDF-1)</i>		Stem cell recruitment and cardiomyocyte and MSC survival	[32, 44]	
<i>TNF-α stimulated gene-6 (TSG-6)</i>		Anti-inflammation action	[17]	
<i>Vascular endothelial growth factor (VEGF)</i>	Prevention of cell death of cardiomyocytes and endothelial cells	[13]		
Exosomes	<i>miR-19a</i>	Akt/ERK signaling activation, through PTEN targeting	[45]	
	<i>miR22</i>	Apoptosis reduction and ischemic CMCs injury improvement, through Mecp2 targeting	[46]	
	<i>20S proteasome subunits (PMSA 1-7)</i>	Cardioprotection through proteolytic degradation of misfolded proteins	[47]	
	<i>Unknown</i>	PMEC migration and vascularization improvement	[48]	
	<i>Unknown</i>	Angiogenesis promotion	[49]	
	<i>Unknown</i>	VEGF level incensement and angiogenesis promotion	[50]	
	<i>Unknown</i>	Oxidative stress inhibition, PI3K/Akt pathway activation and inflammatory activity reduction	[51]	
Microvesicles	<i>Unknown</i>	Hypoxic signal pathway inhibition	[52]	
	<i>miR221</i>	CMCs apoptosis reduction and CMCs survival improvement	[53]	
	<i>Unknown</i>	Endothelial cell proliferation and blood flow recovery	[54]	

Figure 7. Secretome of MSCs and their regenerative function (adopted from Gallina et al.).¹⁰⁰

The paracrine actions of MSCs promote cardiac regeneration through several mechanisms.¹⁰¹

a. Survival and Cytoprotection

Akt has emerged as a central player in the ability of MSCs to promote survival of cardiomyocytes via paracrine-mediated pathways.¹⁰² Among the paracrine factors that rat BM-MNCs release are platelet-derived growth factor, insulin-like growth factor (IGF-1), interleukin (IL)-1b, and vascular endothelial growth factor (VEGF); and hypoxia significantly enhances the release all of these factors. BM-MNCs also suppress programmed cell death of cardiomyocytes while preserving their contractile capacity in conditioned media.¹⁰³

b. Immunomodulation/Inflammation

When injected into myocardium, adult stem cells reduce the inflammatory state by downregulating expression of pro-inflammatory cytokines such as tumor necrosis factor- α , IL-1 β , IL-6, and monocyte chemoattractant protein-1, all effects that rely on a paracrine component.¹⁰⁴ Paracrine factors released by MSCs also can directly inhibit T cell function,¹⁰⁵ and MSCs can prevent dendritic cell maturation and function via release of IL-6 and prostaglandin-E2.^{106,107} In addition, MSCs secrete IL-1 receptor antagonist, which inhibits the

release of tumor necrosis factor- α from activated macrophages.¹⁰⁸ Various reports have shown that MSCs switch macrophages from the pro-inflammatory M1 phenotype to the anti-inflammatory M2 phenotype *in vitro* as well as *in vivo*,¹⁰⁹⁻¹¹¹ presumably through secreted factors such as IGF-1¹¹² and IL-10.¹¹³

c. Cardiomyocyte Proliferation

Mechanisms for cardiomyocyte proliferation are generally either absent or inactive in the adult mammalian heart; however, recent research has uncovered many MSC paracrine factors that may mediate cardiomyocyte proliferation. Fibroblast growth factor (FGF)-2, for example, promotes cardiomyocyte proliferation *in vitro* via PKC ϵ .¹¹⁴ Platelet-derived growth factor increases the proliferation of cardiomyocytes via Akt activation and inactivation of GSK-3 β .¹¹⁵ Neuregulin-1, a member of the epidermal growth factor (EGF) family, stimulates DNA synthesis in both neonatal and adult cardiomyocytes through its specific receptor ErbB4.^{116,117} Finally, the delivery of neuregulin-1 into adult mice by injection encourages regeneration after MI.¹¹⁷

d. Cardiac Remodeling

Cardiac remodeling is mediated by a significant change in the extracellular matrix (ECM) including fibrosis, cardiomyocyte hypertrophy, and changes in ventricular dimension and function. A main goal of regenerative therapy would be to alter the ECM and prevent post-infarction remodeling. Stem cells express many molecules that control the ECM, such as matrix metalloproteinases (MMPs), serine proteases, and serine protease inhibitors, suggesting that transplanted MSCs may prevent fibrosis through a paracrine action.¹¹⁸ MSC transplantation inhibits the expression of collagen-1 and collagen-III as well as the tissue inhibitor of metalloproteinase-1, which are linked to remodeling and overexpressed following MI.¹¹⁹

e. Metabolism and Contractility

Ischemic injury modifies cardiac metabolism with a shift from the typical fatty acid oxidation to glucose uptake and a move to lactate production.¹²⁰ In a rat MI model, Akt overexpression significantly augments the capability of MSCs to inhibit alterations in metabolism, sparing phosphocreatine stores and restraining glucose uptake.¹²¹ Conditioned media from BM-MNCs preserves fractional shortening and maximal rate of relengthening of adult rat ventricular cardiomyocytes in culture.¹⁰³ The release of inotropic paracrine factors is most presumably amplified by hypoxia, but the identity of these factors is currently unknown.

f. Neovascularization

Delivery of MSCs to an occluded coronary vessel triggers an increase in capillary density,^{122,123} which is also seen with administration of BM-MNCs to ischemic myocardium, along with improved local blood flow.¹²⁴ Paracrine factor release from transplanted adult stem cells includes factors that promote angiogenesis such as basic FGF, angiopoietin, VEGF, and hepatocyte growth factor (HGF).^{123,125} As evidence of VEGF's critical role as an angiogenesis-promoting paracrine factor, ablation of its gene results in a significantly reduced capacity of MSCs to effect recovery of function in heart injury.¹²⁶ The relevance of these findings is somewhat tempered by the fact that antibody interference with VEGF and FGF has only a limited inhibitory effect, suggesting that MSCs may have pathways or beneficial factors that complement or compensate for one another.

g. Resident Stem Cell Activation

The myocardium encloses many resident stem cells, which are characterized by several markers including c-Kit and Sca-1. The most intensively investigated resident stem cell of the heart is the c-Kit cardiac progenitor cell (CPC). These CPCs are supposed to be capable of supporting regeneration via mobilization into the injured tissue and differentiation into mature cardiac cells. In patients with heart failure following MI, delivery of c-Kit⁺ autologous CPCs via intracoronary injection is reported to decrease infarct size and boost ventricular systolic function.^{127,128} Yet, in all of these studies, it was obvious that donor c-Kit⁺ cell differentiation into mature cardiac cells, such as cardiomyocytes, was too limited to explain the functional benefits. As noted, paracrine factors might be involved, and indeed, recent work has suggested that such factors from adult stem cells may significantly enhance the ability of local c-Kit⁺ CSCs to differentiate into cardiomyocytes. Furthermore, application of conditioned medium that has been derived using MSCs leads to both proliferation and differentiation of CPCs. The growth factor IGF-1, a paracrine factor released by MSCs, promotes resident stem cell mobilization¹²⁹ and commitment to the cardiac lineage.^{130,131}

In addition, oligonucleotides recently have been proposed to have role in cardiac regeneration. Regenerative miRNAs and other non-coding RNAs might be mediators of paracrine effects in cardiac repair (Figure 8). MicroRNAs (miRNAs) are post-transcriptional regulators of expression of different genes and consist of approximately 22 nucleotides. They are also expressed in cardiovascular organ tissues and involved in several cellular mechanisms of cardiovascular diseases, such as cardiac hypertrophy, MI, and arrhythmias.^{132,133} MiRNAs play a role in cardiac developmental biology, stem cell differentiation, apoptosis, neovascularization, cardiac repair processes, and LV remodeling.^{132,134,135} Several miRNAs are dysregulated in the acute and chronic phases of MI

and have discriminatory diagnostic value.^{136,137}

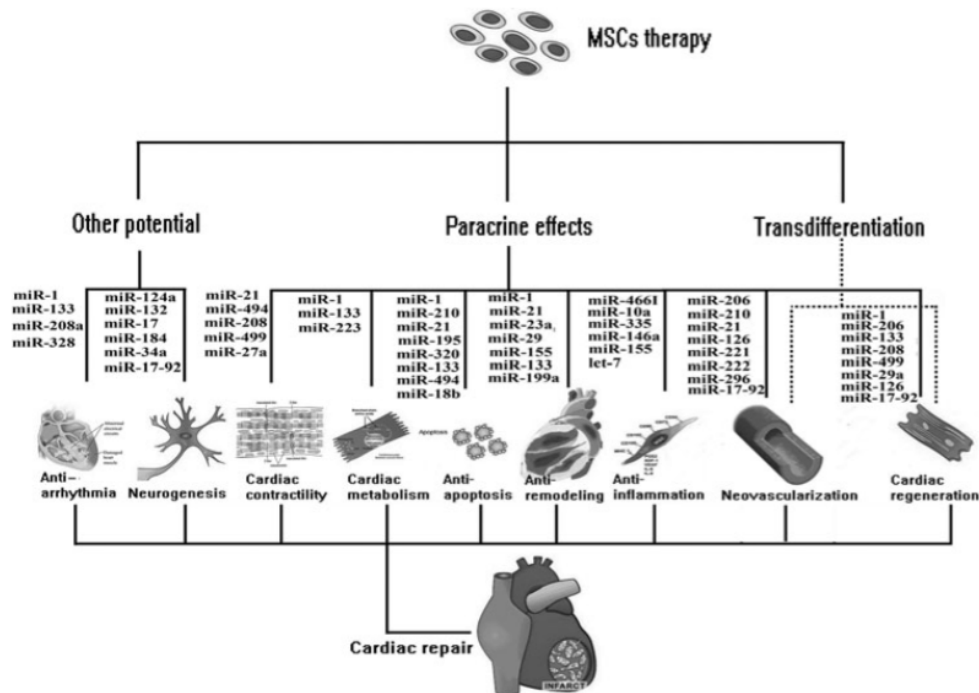


Figure 8. Summary of miRNAs in cardiovascular repair mechanisms mediated by MSCs (adopted from Wen et al. 2011).¹³²

Additionally, other oligonucleotides, such as long noncoding mRNAs, also play a role in the cardiovascular system (Figure 9).¹³⁸

Circulating ncRNAs and ncRNAs in age-related cardiovascular diseases.

	Disease/condition	Modulation	Refs
miR-1	Myocardial infarction	Up	[191-194]
miR-133	Myocardial infarction	Up	[159,192]
miR-208a	Myocardial infarction	Up	[193]
miR-208b	Myocardial infarction	Up	[173,193]
miR-499	Myocardial infarction	Up	[166,193,194]
miR-328	Myocardial infarction	Up	[195]
miR-27b	Myocardial infarction	Down	[196]
miR-126	Myocardial infarction	Down	[197]
miR-126, miR-92a, miR-17, miR-155, and miR-145	Coronary artery disease	Down	[198]
miR-147	Coronary artery disease	Down	[171]
miR-135	Coronary artery disease	Up	[171]
miR-337-5p, miR-433, and miR-485-3p	Coronary artery disease	Up	[170]
miR-134, miR-198, and miR-370,	Unstable angina vs stable angina	Up	[171]
miR-106b, miR-25, miR-92a, miR-21, miR-590-5p, miR-126*, and miR-451	Unstable angina vs stable angina	Up	[162]
miR-423-3p	Heart failure	Up	[172]
miR-499, -122	Heart failure	Up	[173]
miR-126	Heart failure	Down	[57]
miR-107, miR-139, miR-142-5p, miR-125b, and miR-497	Heart failure	Down	[174]
miR-142-3p, miR-29b	Heart failure	Up	[174]
miR-503	Ꞥ2dm + critical limb ischemia	Up	[175]
ANRIL	Myocardial infarction	Down	[179]
aHIF	Myocardial infarction	Up	[179]
ANRIL, KCNQ1OT1	Myocardial infarction	Down	[179]
LIPCAR	Myocardial infarction	Down	[181]

Figure 9. Role of circulating miRNAs and long noncoding RNAs in cardiovascular diseases (adopted from Greco et al. 2015).¹³⁸

Pinpointing the cellular source of these beneficial factors has been another question to resolve, and evidence is growing that some of them may be packaged into extracellular membrane vesicles (EVs) such as exosomes and microparticles (MPs). All cell types secrete both, and both appear to be present in all biological fluids and cell culture media. The stored material, including miRNAs, lipids, proteins, and nucleic acids, are transferrable to target cells, allowing the producing cell to affect the functions of these other cells and regulate endogenous cell populations. Evidence supports the function of EVs in the benefits of cell therapy, including repair following MI¹³⁹ and, most crucially, that using EVs alone comes close to re-creating the beneficial effects of whole cell transplantation. What remains to be pinned down are the precise molecules involved and whether or not they must interact complementarily as delivered in the vesicle or can exert effects as single molecules.

A summary of paracrine factors used in clinical trials and their main results are listed in Figure 10. The stromal cell–derived factor-1 (SDF-1) was the first molecule to be regarded as a paracrine factor, recruiting progenitor cells expressing the homing receptor of CXCR4, which leads them to wander to the peri-infarcted area when sensing the chemotactic stimulus of SDF-1.¹⁴⁰

Table 1 Summary of paracrine factors used in clinical trials for myocardial repair.

Factor	Phase	Patient type and no.	Results	Ref
rhEPO	Randomized, controlled trials	Chronic heart failure, n = 32	An increase of 5.5% and a decrease of 5.4% in LVEF in the treatment and control groups, respectively.	Silverberg et al. (2001)
rhFGF2	Phases I and II	Coronary artery disease, n = 337	No improvement in exercise tolerance or myocardial perfusion at day 180. Significant reduction in angina was observed at day 90 but not at day 180 compared to that of the placebo group.	Simons et al. (2002)
rhG-CSF	Randomized, controlled trials	Acute MI, n = 385	Increased EF in patients with early MI (4.65%, p < 0.0001) or with mean baseline EF < 50% (4.73%, p < 0.0001) compared to that of the controls.	Abdel-Latif et al. (2008)
rhGrowth hormone	A mixture of controlled and uncontrolled trials	Congestive heart failure, n = 212 in 14 studies	Improved LVEF by 4.3% compared to that of the controls. An increase in left ventricular mass and wall thickness was observed. There was no examination in development of arrhythmias.	Tritos and Danias (2008)
rhNeuregulin-1	Phase I	Chronic heart failure, n = 15	Increased LVEF (4–12%, p < 0.001) at day 12–84 post infusion with neuregulin-1 compared to controls. Adverse side effects were reported.	Jabbour et al. (2011)
	Phase II	Chronic heart failure, n = 44	No statistically significant difference in % LVEF compared to that of the placebo group.	Gao et al. (2010)
rhVEGF	Phase I (VIVA trial)	Coronary artery disease, n = 178	Low-dose rhVEGF did not have any effect by day 60 after infusion; high-dose rhVEGF improved angina by day 120 compared to that of the placebo group.	Henry et al. (2003)
	Phase I	Coronary artery disease, n = 14	Improved myocardial perfusion at rest in a dose-dependent manner.	Braitsch et al. (2013)

Abbreviations – rh: recombinant human protein; LVEF: left ventricular ejection fraction.

Figure 10. Summary of paracrine factors used in clinical trials (adopted from Lui et al.).¹⁴¹

Recently, several emerging concepts of the paracrine mechanism have been proposed¹⁰¹: (1) Paracrine factors released by stem cells influence adjacent and distant cells differentially by their concentration gradients, thus creating a tissue microenvironment; (2) paracrine factors have pleiotropic actions on different cells and multiple mechanisms; and (3) paracrine factors can exert temporal and spatial effects on cardiac repair and regenerative events.

1.3.2. Secretome of apoptotic cells in cardiac repair

Apoptotic peripheral blood mononuclear cells (PBMCs) also can have beneficial effects on myocardial function, similar to those seen with living stem cells.¹⁴²⁻¹⁴⁴ As with the latter, paracrine factors are hypothesized to be the effectors, acting by limiting inflammation, enhancing angiogenesis, protecting resident myocytes and promoting their cell cycle re-entry, boosting cardiac cell metabolism and contractility, stimulating humoral activity, and recruiting endogenous stem cells.^{96,142,145}

The viability rate of the cells applied in clinical trials is about 75 to 95%.^{28,146,147} Accordingly, about 5-25% of the cells are dead or apoptotic at the time of cell delivery.¹⁴⁶ Another proportion of the cells is going to be apoptotic in the ischemic myocardium because of the lack of oxygen or nutritive substances and the effect of cytotoxic molecules in the necrotic environment.¹⁴⁸ Necrotic cells release inflammatory mediators, such as heat-shock proteins or Toll-like receptor-4, amplifying local inflammation. In contrast with necrotic cells, apoptotic cells mitigate the inflammation. Endocytosis of apoptotic cells by macrophages triggers release of anti-inflammatory mediators, such as IL-10 or transforming growth factor-beta.¹⁴⁶ Other candidate mechanisms may be inhibiting the pro-inflammatory cytokines IL-6, tumor necrosis factor-alpha, or IL-1b. All of these local processes lead to acceleration of the inflammatory tissue resolution. In addition, apoptosis triggers the activation of immature dendritic cells (also found in myocardium), which further enhances the anti-inflammatory processes by upregulation of anti-inflammatory molecules and downregulation of other pro-inflammatory cytokines.¹⁴⁹ The local inflammatory cells also undergo apoptosis, multiplying the apoptotic signal intensity. In contrast with the necrotic core of the infarction, the border zone consists of many viable cells with reduced energy metabolism and of apoptotic cells. Cell delivery in this area is of particular importance as the injected cells become locally apoptotic, amplifying the apoptotic response (Figure 11).¹⁴⁶

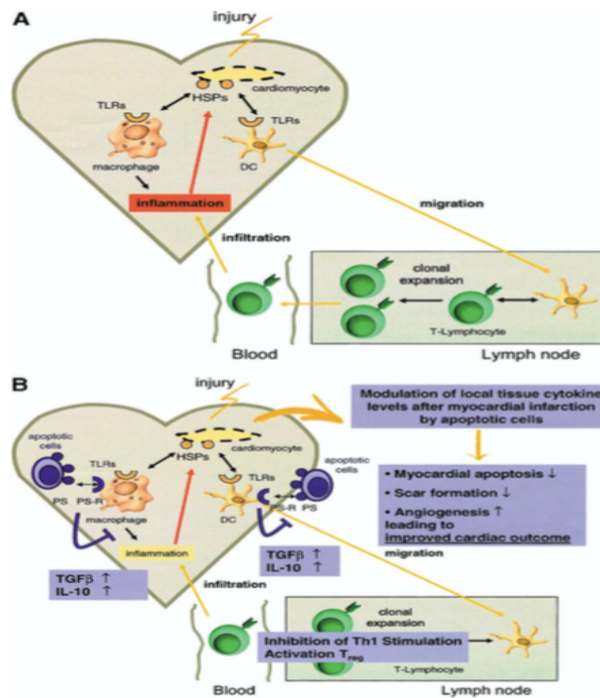


Figure 11. The dying cell hypothesis (adopted from Thum et al. 2005).¹⁴⁶

Furthermore, treatment of the isolated mouse heart subjected to ischemia/reperfusion with exosome leads to preservation of LV contractility via increased ATP, NADH, phosphorylated Akt, and phosphorylated GSK-3 β and decreased oxidative stress and phosphorylated c-JNK.¹⁵⁰

1.3.3. Paracrine regenerative effect of the secretome of apoptotic peripheral blood mononuclear cells (APOSEC)

1.3.3.a. Mechanisms of action of APOSEC

Having shown that apoptotic PBMCs promote regeneration in spinal cord injury, the heart, and wound healing,¹⁵¹⁻¹⁵⁹ Ankersmit et al. turned to these cells as a way to reprogram the inflammatory response and neo-angiogenesis following AMI, both of which are critical to post-AMI remodeling. They hypothesized that paracrine factors from apoptotic PBMCs might recruit c-kit⁺ EPCs from the BM to the site of damage.¹⁵⁹ They first irradiated PBMCs to induce apoptosis, confirmed their identity, and then injected them intravenously into a rat MI model. As controls, these authors used non-irradiated PBMCs and cell-free medium. To assess the immunomodulatory potential of apoptotic cells, this group stimulated the

irradiated PBMCs with lipopolysaccharide (LPS), following by RNA analysis and testing in human fibroblast culture (Figure 12).

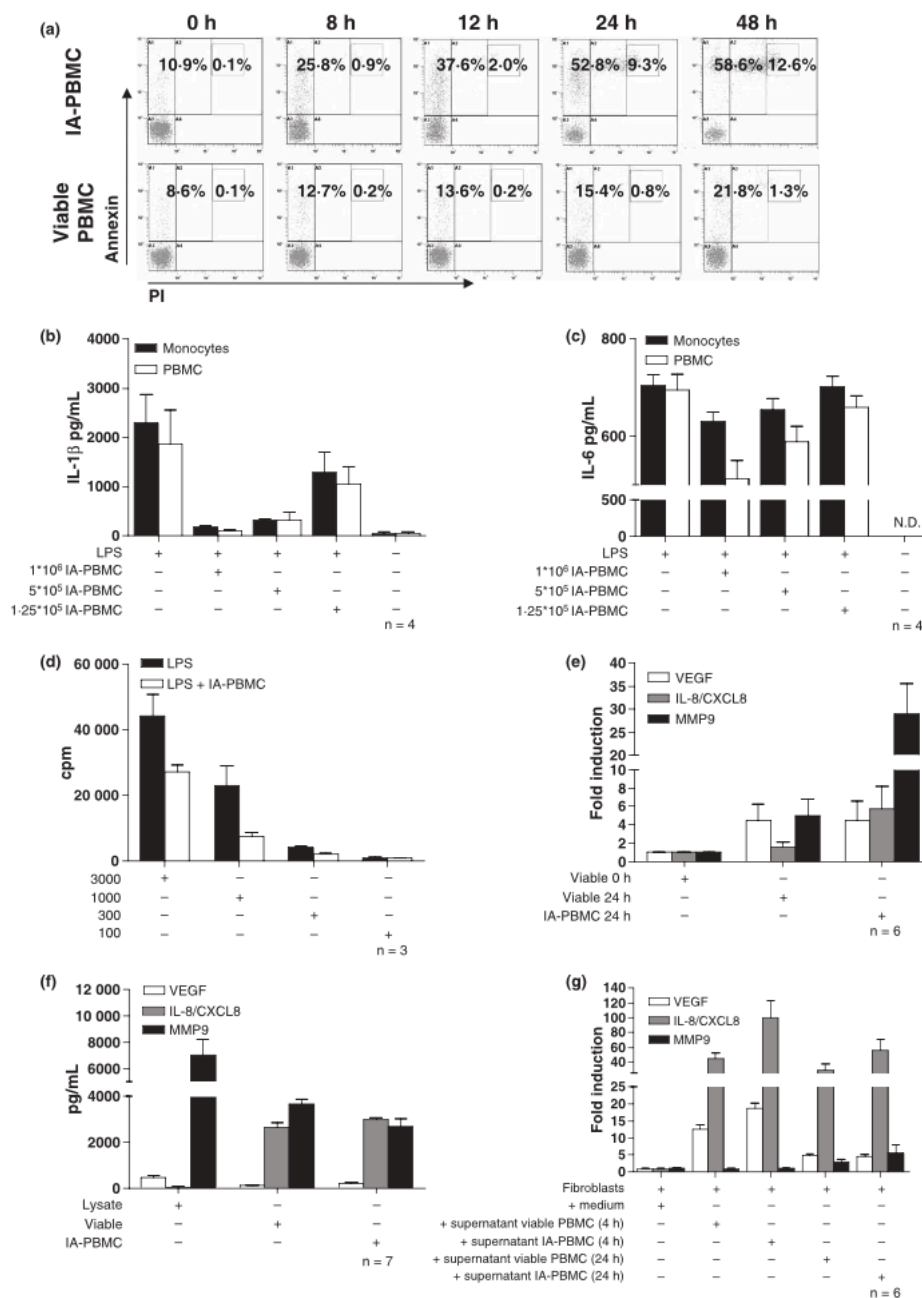


Figure 12. PBMC response to irradiation. (a) Per FACS analysis, irradiation induced apoptosis in human PBMCs with increased Annexin V expression over 48 h ($n = 4$). Necrosis was defined by high PI-positive staining. (b) Dose-dependent reduced secretion of pro-inflammatory IL-1 β with co-incubation of LPS-stimulated PBMCs or monocytes and irradiated apoptotic autologous PBMCs ($n = 4$). (c) IL-6 secretion of LPS-stimulated PBMCs and monocytes in the presence of IA-PBMC ($n = 4$). (d) Decreased T cell proliferation (counts per minute (cpm), $n = 3$) following addition of autologous IA-PBMCs in a mixed lymphocyte reaction with LPS stimulation. (e) RNA expression analysis (RT-PCR) of VEGF, IL-8/CXCL8, and MMP9. (f) Protein levels of VEGF, IL-8/CXCL8, and MMP9. (g) Fold induction of VEGF, IL-8/CXCL8, and MMP9 in fibroblasts.

MMP9 transcripts; upregulation of IL-8/CXCL8 and MMP9 in irradiated PBMCs after a culture period of 24 h ($n = 6$). (f) ELISA of VEGF, IL-8/CXCL8, MMP9; MMP9 is seen predominantly in cell lysates, whereas VEGF and IL-8/CXCL8 protein secretion differences look similar in viable cells and IA-PBMCs ($n = 7$). (g) Human fibroblasts, incubated with supernatants from cultures of viable cells or IA-PBMCs, showing strong VEGF, IL-8/CXCL8, and MMP9 upregulation (RT-PCR); peak values were from fibroblasts incubated in IA-PBMC supernatants ($n = 6$) (adopted from Ankersmit Eur J Clin Invest-2009).¹⁵⁹

When irradiated or viable PBMCs or medium were administered to the rat MI model, more cells in the infarcted area stained positive for VEGF and c-kit, but histological analysis of hearts explanted 6 weeks post-MI showed less dilatation and less scar tissue formation in cell-treated animals. However, irradiated cells were associated with the least extension of scar tissue ($5.8 \pm 2.0\%$, mean \pm SEM) vs medium ($24.95 \pm 3.6\%$) and viable PBMCs ($14.3 \pm 1.3\%$) (Figure 13).¹⁵⁹

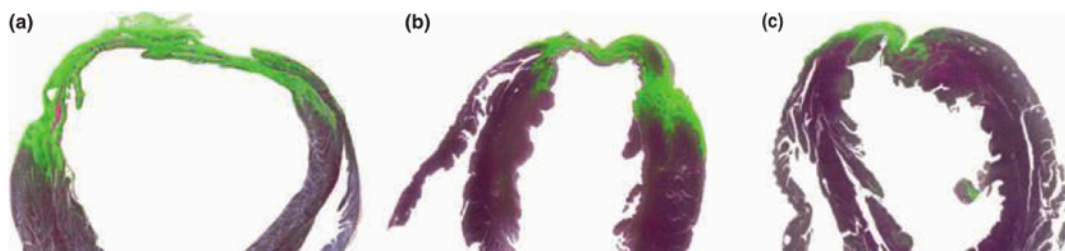


Figure 13. Comparison of the effect of irradiated vs viable PBMCs in a rat MI model. Ischemic rat hearts (Elastica van Gieson staining), explanted 6 weeks post-MI induction: (a) medium injection only, hearts appear more dilated, with a greater extent of fibrosis (green indicates infarcted myocardium); (b) reduced scar extension with injection of viable cells; (c) fewer signs of dilatation and least extent of scar tissue following injection of irradiated PBMCs (adopted from Ankersmit Eur J Clin Invest-2009).¹⁵⁹

Further evaluation of the secretome of the living and apoptotic PBMCs showed that several regenerative factors secreted by the apoptotic cells were present in higher amounts compared to the secretome of living PBMCs (Figure 14).

Table 1 Analysis of soluble factors secreted by non-irradiated cells and irradiated apoptotic PBMC (APOSEC)

Soluble factors (ng/ml)	Viable PBMC			Apoptotic PBMC			Sig.
	1 × 10 ⁶	2.5 × 10 ⁶	25 × 10 ⁶	1 × 10 ⁶	2.5 × 10 ⁶	25 × 10 ⁶	
IL-8	1.74 ± 0.40	1.93 ± 0.09	10.49 ± 3.53	1.22 ± 0.29	2.30 ± 0.13	18.01 ± 2.87	ns ns ^Y
GRO-alpha	0.17 ± 0.09	0.36 ± 0.09	2.06 ± 1.58	0.07 ± 0.02	0.48 ± 0.09	3.95 ± 0.93	ns ns ns
ENA-78	3.41 ± 1.34	29.93 ± 3.41	34.89 ± 16.33	3.93 ± 1.43	37.86 ± 12.73	108.86 ± 27.88	ns ns ^Y
MCP-1	1.66 ± 0.65	0.47 ± 0.21	0.27 ± 0.00	0.76 ± 0.19	0.74 ± 0.17	0.27 ± 0.00	ns ns ns
RANTES	8.32 ± 0.18	18.62 ± 3.21	37.63 ± 2.72	4.01 ± 0.05	22.25 ± 3.64	51.58 ± 4.44	ns ns ns
HMGB1	0.63 ± 0.39	3.44 ± 2.11	33.57 ± 6.45	2.74 ± 0.27	6.46 ± 1.12	20.51 ± 3.62	ns ns [†]
MMP9	4.14 ± 0.91	14.59 ± 2.75	29.46 ± 8.29	0.99 ± 0.16	3.61 ± 0.59	19.35 ± 5.34	ns ^{†,‡}
sICAM-1	0.14 ± 0.04	1.43 ± 0.25	7.43 ± 0.85	0.42 ± 0.25	2.09 ± 0.42	9.40 ± 1.29	ns ns ^Y
VEGF ₁₆₅	0.13 ± 0.01	0.42 ± 0.04	0.82 ± 0.34	0.15 ± 0.02	0.64 ± 0.04	4.39 ± 1.22	ns ns ^Y
MIF	4.84 ± 0.09	17.79 ± 0.95	13.24 ± 0.85	5.85 ± 0.22	20.15 ± 1.14	58.99 ± 1.17	ns ns ^Y
PAI-1	1.25 ± 0.35	1.93 ± 0.29	49.60 ± 9.04	0.00 ± 0.00	5.06 ± 3.25	45.86 ± 1.43	ns ns ns
IL-16	0.0 ± 0.0	0.11 ± 0.02	0.84 ± 0.31	0.00 ± 0.00	1.25 ± 0.07	5.25 ± 0.52	ns ^{†, Y}
IL-1ra	0.35 ± 0.09	0.52 ± 0.17	2.16 ± 0.96	0.13 ± 0.04	0.41 ± 0.17	6.43 ± 1.33	ns ns ^Y
IL-10	0.01 ± 0.00	0.00 ± 0.0	0.05 ± 0.01	0.02 ± 0.01	0.02 ± 0.01	0.06 ± 0.01	ns ns ns
IGF-1	0.00 ± 0.00	0.01 ± 0.0	0.03 ± 0.02	0.00 ± 0.00	0.01 ± 0.01	0.03 ± 0.03	ns ns ns
HGF	0.33 ± 0.08	0.16 ± 0.01	0.69 ± 0.19	0.11 ± 0.03	0.07 ± 0.02	0.79 ± 0.19	ns ns ns
FGF-2	0.56 ± 0.02	0.53 ± 0.00	0.59 ± 0.01	0.48 ± 0.01	0.53 ± 0.02	0.55 ± 0.02	ns ns ns
TGF-β	0.08 ± 0.01	0.10 ± 0.01	0.21 ± 0.07	0.06 ± 0.01	0.09 ± 0.02	0.39 ± 0.09	ns ns ns
SDF-1	0.17 ± 0.0	0.19 ± 0.0	0.22 ± 0.03	0.16 ± 0.01	0.15 ± 0.07	0.12 ± 0.04	ns ns ns
G-CSF	0.00 ± 0.00	0.00 ± 0.00	0.00 ± 0.00	0.00 ± 0.00	0.00 ± 0.00	0.00 ± 0.00	ns ns ns
GM-CSF	0.00 ± 0.00	0.00 ± 0.00	0.07 ± 0.02	0.00 ± 0.00	0.00 ± 0.00	0.08 ± 0.02	ns ns ns

Cells were incubated in three different cell concentrations for 24 h. Supernatants were analyzed for cytokines, chemokines and growth factors (n = 5)

ns p > 0.05 viable PBMC versus apoptotic PBMC (of corresponding cell density)

[†] p < 0.05 1 × 10⁶ viable PBMC versus 1 × 10⁶ apoptotic PBMC

[‡] p < 0.05 2.5 × 10⁶ viable PBMC versus 2.5 × 10⁶ apoptotic PBMC

^Y p < 0.05 25 × 10⁶ viable PBMC versus 25 × 10⁶ apoptotic PBMC

Figure 14. Content of secretomes of living and apoptotic PBMCs (adopted from Lichtenauer BRC-2011).¹⁵⁸

For further analysis of the biologically active components of APOSEC, the transcriptome and different fractions of the supernatants of human PBMCs after irradiation were assessed by Beer et al., with results suggesting several mechanisms in organ tissue regeneration.^{160,161}

Gene expression analysis was conducted with whole human genome oligo microarrays in PBMCs after 2, 4, and 20 h of cultivation following irradiation and compared with the non-irradiated transcriptome. Figure 15 shows two heatmaps for 525 (non-irradiated) and 1099 (irradiated PBMC) genes, respectively, that had a minimum fold-change upregulation <2.0 over baseline at two or more of the three time points. A total of 167 transcripts encoded proteins actively secreted by non-irradiated cells and 213 secreted by irradiated PBMCs.

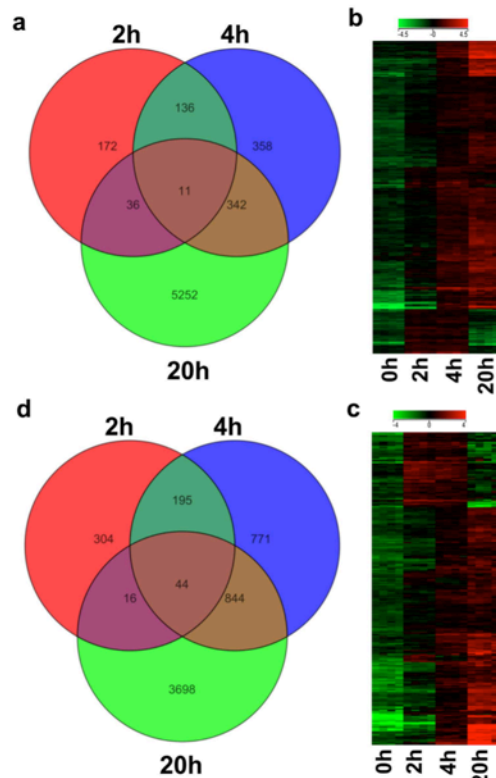


Figure 15. Effects on PBMC transcriptome of irradiation at 2, 4, and 20 h of cultivation. Venn diagrams: numbers of transcripts upregulated with >2-fold expression changes above baseline after cell separation for (a) non-irradiated and (d) irradiated PBMCs. Heatmaps: (b) non-irradiated and (c) irradiated PBMCs, with expression most prominent at 20 h post-cultivation. Green = downregulated; red = upregulated; $n = 4$ per time point (adopted from Beer SciRep-2015).¹⁶¹

The 20-h time point showed the highest expression change in irradiated PBMCs, with expression appearing to shift from proteins related to metabolic processes before irradiation to regeneration after irradiation, including proteins related to angiogenesis, wound healing, and leukocyte trafficking.

ELISA of supernatant protein content following the 20-h time point showed that compared to viable PBMCs, irradiated PBMCs had higher concentrations of thrombospondin, CXCL13, neuropilin, and angiogenin but that concentrations of adrenomedullin, PDGF-AB, PDGF-BB, and C3 were similar between the two. Versus viable cells, lipids from the supernatant of irradiated cells had greater concentrations of oxidized lipid products in the CM and of triglycerides, phospholipids, cholesterol, free fatty acids, cholesterol sulfate, and cholesterol esters but similar concentrations of non-oxidized precursor phospholipids. Both cell populations had large nuclei and scanty cytoplasm on electron microscopy, but irradiated cells were notable for disintegrating cell membrane and more intercellular debris, both

suggesting that MPs were being released from the plasma (Figure 16). Annexin V staining and detection of MPs with FACS analysis, relying on SSC/FL1 characteristics, showed that the irradiated cells had released MPs with diameters between 0.2 and 0.5 μm (Figure 16).

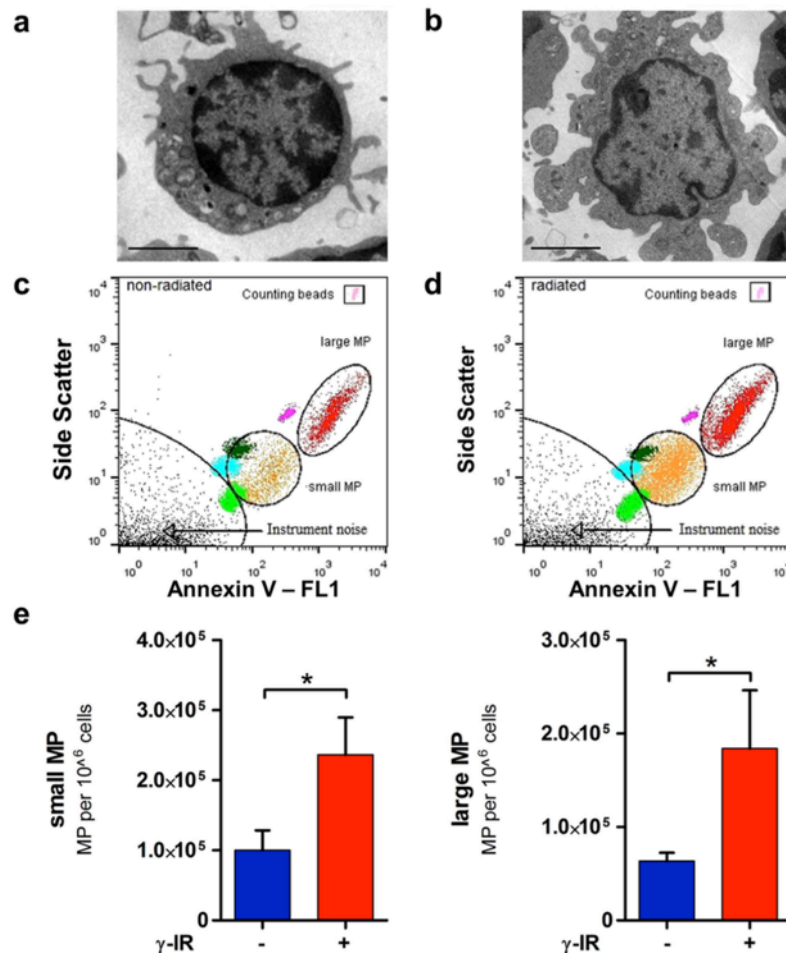


Figure 16. The effect of ionizing radiation on microparticle release. Non-irradiated (a, c, e, left) and irradiated (b, d, e, right) PBMCs were cultured for 20 h and analyzed by electron microscopy and FACS. (a) Non-irradiated cell with largely intact PM, nucleus, and minor PM shedding. Scale bar = 2.5 μm . (b) Irradiated cell with shrinking, PM fragmentation, chromatin condensation. (c, d) (e) FACS quantification of the absolute number of MPs released from PBMCs (adopted from Beer SciRep-2015).¹⁶¹

Exosomes also were isolated from the culture medium of irradiated and non-irradiated cells at 20 h of culture using ultracentrifugation. Exosome count in supernatant from irradiated PBMCs (15×10^5 exosomes/ 10^5 cell) was 3-fold that of non-irradiated PBMCs (6×10^5 exosomes/ 10^5 cell). Irradiated cells also had a higher exosome protein content based on 2D gel electrophoresis results.

In vitro assays proved the biological effects of distinct components of the supernatant. CXCL1 and CXCL8 expression was increased in human fibroblast cultures in response to stimulation with total supernatant of irradiated and non-irradiated PBMCs and with isolated exosomes. In primary human keratinocyte cultures, the total supernatant and the protein fraction of irradiated PBMCs led to a significantly stronger induction of gene expression than those of non-irradiated samples.

The time-dependent analysis of the transcriptome of mRNA and miRNA after high-dose irradiation of PBMCs revealed that at 4 h after irradiation, the apoptotic and p53 signaling pathways were dominant, while other apoptosis-related cellular processes were seen to predominate at 20 h post-irradiation. In the late phase after irradiation, 177 miRNAs were significantly up- or downregulated, with a significant negative correlation with target gene mRNA expression (Figure 17).¹⁶⁰ The identified miRNAs have roles in regulating pathways involved in the radiation response, such as the apoptotic pathway, and in MAPK signaling, interactions among cytokines, and endocytosis.

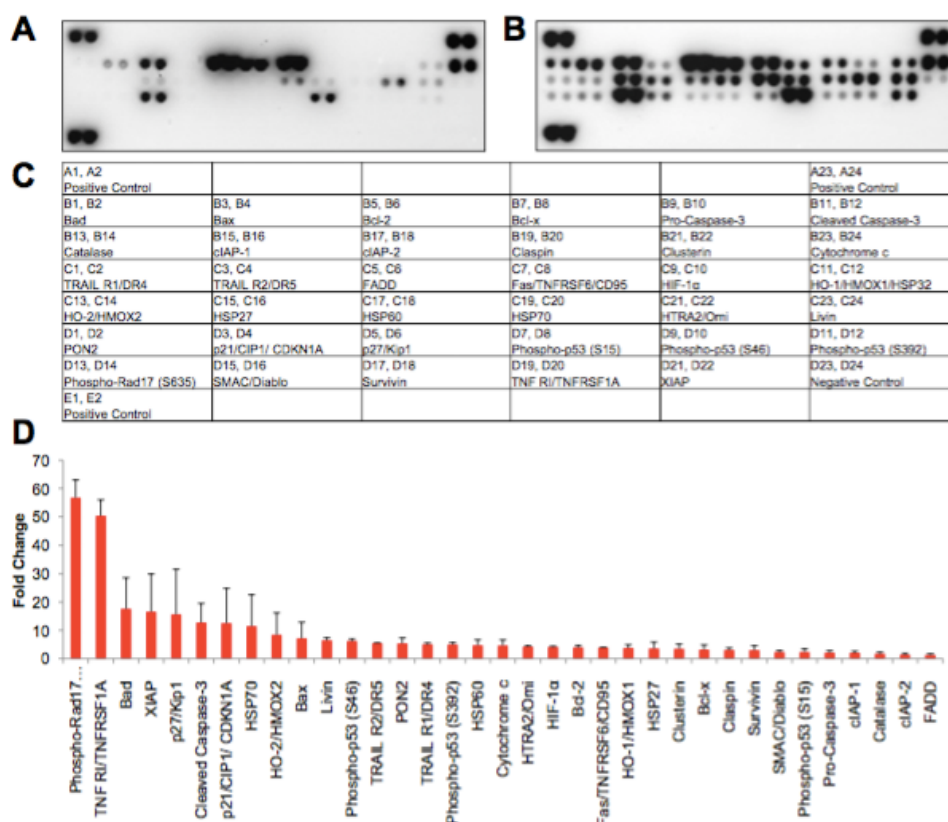


Figure 17. Proteins that are upregulated with radiation exposure. Membrane array from cell lysates of 10^6 non-irradiated (A) or irradiated (B) human PBMCs at 20 h post exposure to

ionizing radiation. (C) Protein list; (D) average pixel intensities (adopted from Beer BMC Genomics-2014).¹⁶⁰

In an AMI pig model in which experimental and viral-cleared, GMP (good manufacturing practice)-compliant supernatant were evaluated by injection 45 min after ischemia onset, both treatments led to improved cardiac output and smaller areas of infarct versus controls at 30 days.

Overall, these results show that irradiation of cells triggers alterations in the human PBMC secretome, both qualitatively and quantitatively. Compared to non-irradiated cells, irradiated PBMCs release more oxidized phospholipids, extracellular vesicles, and proteins that promote angiogenesis. Based on results from *in vitro* studies with human keratinocytes and fibroblasts, the protein and exosome fractions contain the factors that are biologically active in APOSECs. This evidence base opens the way to further exploration and development of regenerative cell-free therapies.

1.3.3.b. Cardiac regenerative effect of APOSEC in rodents and pigs with acute MI

The first experiments of Ankersmit et al. using irradiated PBMCs for the treatment of rat AMI showed that the cell suspension of stressed PBMCs significantly reduced the infarct size and increased the LVEF as compared with viable PBMCs.¹⁵⁹ Irradiated PBMCs enhanced the secretion of pro-angiogenic MMP9 and IL-8 and facilitated the homing of reparative FLK+/c-kit+ progenitor cells in the infarction zone.¹⁵⁹ The main mechanism suggested was the paracrine effect exerted by the enhanced release of cytokines by the apoptotic cells.

As a next step, the irradiated or non-stressed PBMCs were discarded, and only the soluble factors of the cell culture medium of the irradiated and control PBMCs were used. The Ankersmit group published the first evidence of a regenerative effect of the cell-free medium of the irradiated PBMCs, called APOSEC, the secretome of the irradiated PBMCs. Lichtenauer et al. demonstrated the cytoprotective effect of the APOSEC first under *in vitro* conditions in human cardiomyocyte cell culture, followed by the first *in vivo* proof of concept in rat AMI.¹⁵⁷

When human cardiac myocytes were incubated with APOSEC, they secreted survival factors, such as AKT, Erk1/2, p38, and MAPK; these factors are members of the myocardial salvage RISK pathway during ischemia/reperfusion injury. Additionally, the anti-apoptotic Bcl-2 and BAG1 were upregulated 24 h after the co-culture with APOSEC (Figure 18).¹⁵⁷

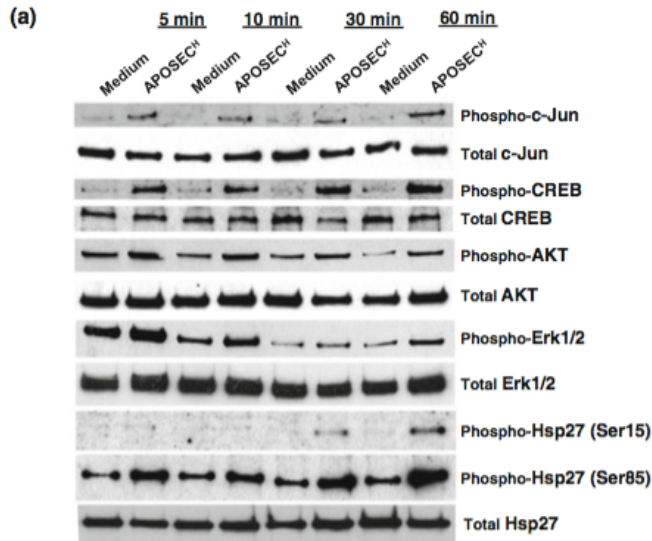


Figure 18. Time-dependent induction of release of cytoprotective substances of human cardiomyocytes after co-culture with APOSEC (adopted from Lichtenauer-BRC-2011b).¹⁵⁷

Furthermore, in the closed-chest reperfused MI translational pig model, APOSEC was infused intravenously at minute 40 of coronary occlusion, resulting in a significantly increased LVEF one month after the infarction. Because of the closed-chest and intravenous infusion, the MI pig model is as close as possible to representing primary percutaneous coronary intervention in the clinic, with a 90-minute closure of the mid-left anterior descending coronary artery, followed by reperfusion (Figure 19).¹⁵⁷

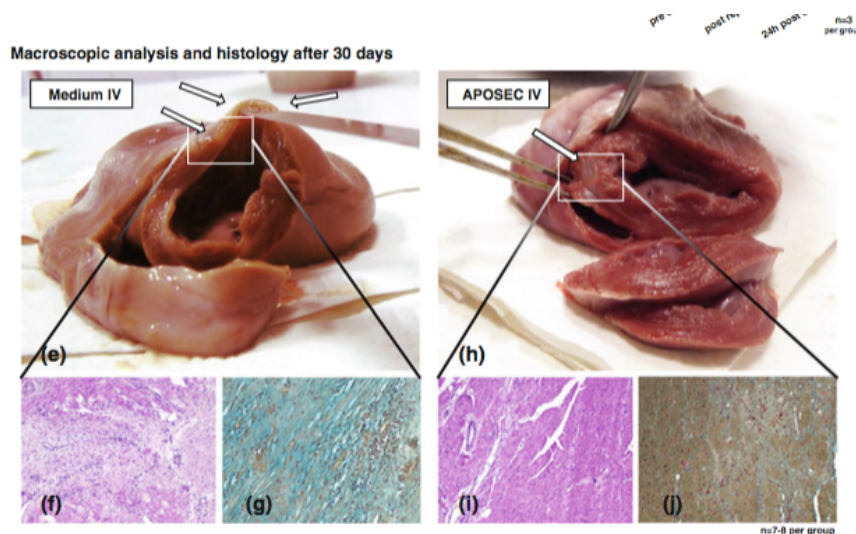


Figure 19. Administration of APOSEC in acute MI phase in a pig model representing closed-chest reperfusion (adopted from Lichtenauer-BRC-2011b).¹⁵⁷

As a mechanism of action, several possible basic processes were suggested and demonstrated:

First, as also previously mentioned, the cytoprotective and anti-inflammatory effect of APOSEC was demonstrated.¹⁵⁷

Second, intravenous infusion of APOSEC in the 40th min of the coronary occlusion resulted in a decrease in microvascular obstruction, confirmed by cMRI with late enhancement (Figure 20).¹⁵⁶

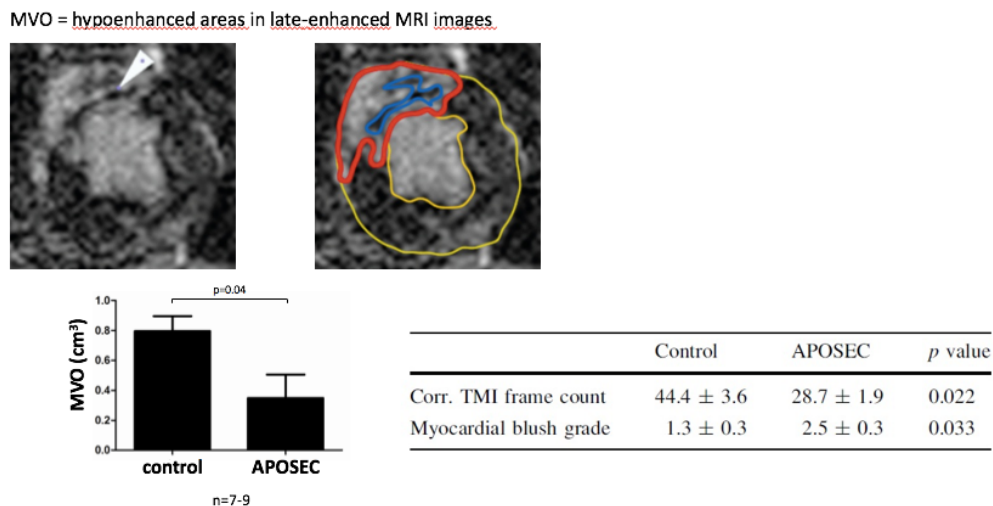


Figure 20. Decrease in microvascular obstruction (MVO) after administration of APOSEC in the acute phase of MI (Hoetzenecker-BRC-2012).¹⁵⁶

Cardiac MRI with late enhancement showed hypoenhanced areas in late-enhanced images. Corrected TIMI frame count and myocardial blush grade confirmed the better macro- and microvascular-related tissue perfusion.

Third, APOSEC inhibited platelet activation, as a significantly lower amount of platelet activation markers, such as P-selectin, TSP-1, PF-4, and CD40L were detected in the pigs at different time points after AMI induction (Figure 21).¹⁵⁶

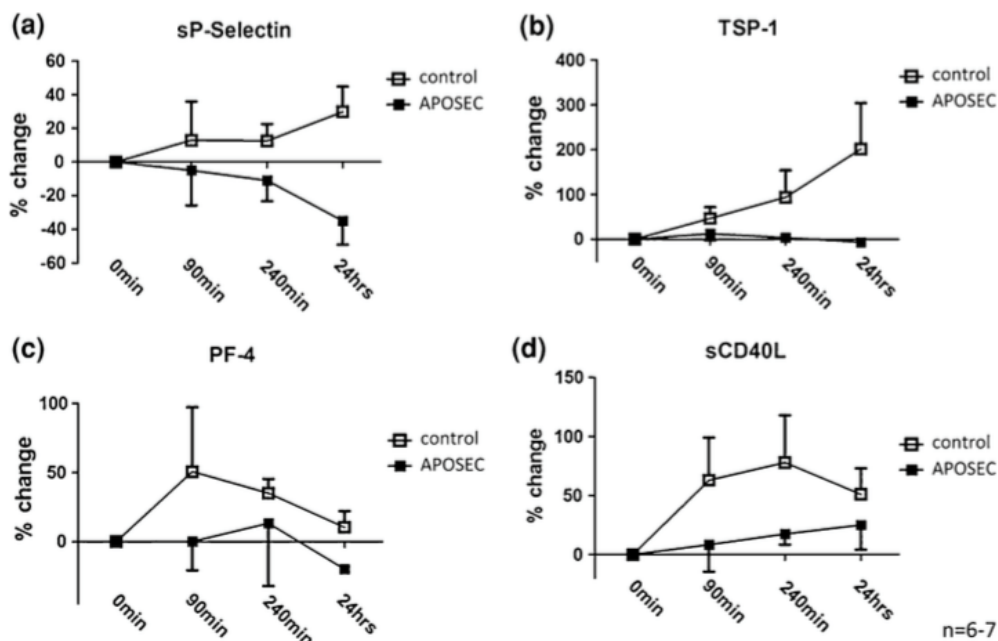


Figure 21. Time-dependent decrease in circulating platelet activation markers measured in plasma of APOSEC or medium control-treated pigs (adopted from Hoetzenecker BRC-2012).¹⁵⁶

Furthermore, *in vitro* platelet function analyses clearly demonstrated the antiplatelet effect of APOSEC (Figure 22).¹⁵⁶

Isolated human platelets were stimulated with different concentrations of TRAP-6 and ADP with or without preincubation with APOSEC.

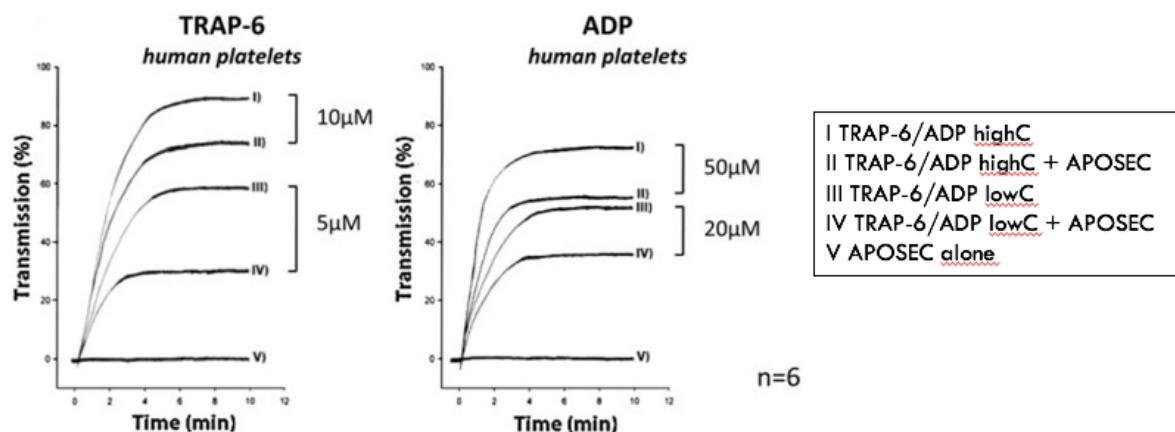


Figure 22. Antiplatelet activity of APOSEC confirmed by light transmittance aggregometry (adopted from Hoetzenecker et al. BRC-2012).¹⁵⁶

Fourth, APOSEC elicits vasodilation, proven by induction of inducible nitric oxide (iNOS) and endothelial (eNOS) in cell culture, as well as an increase in circulating NO, PGI₂, and vasoactive intestinal peptide (VIP) in APOSEC-treated animals compared to medium-treated

controls. Additionally, *in vitro* myograph experiments revealed a dose-dependent vasodilatory action of APOSEC (Figure 23).¹⁵⁶

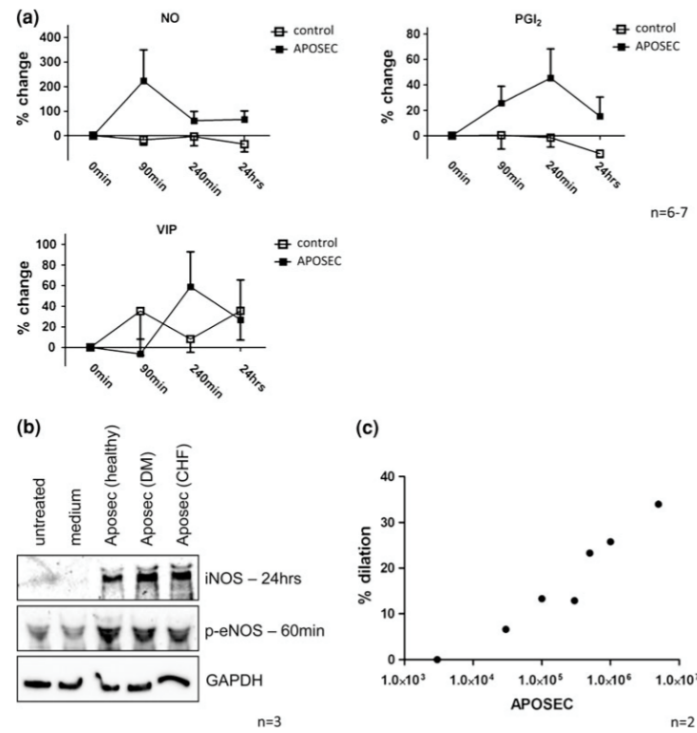


Figure 23. Vasodilatory effect of APOSEC. (a, b) Evidence of an increase in vasodilatory substances circulating in pigs following APOSEC treatment in the acute MI phase; (c) the vasodilatory effect of APOSEC in the organ chamber myograph model is dose dependent (adopted from Hoetzenecker et al. BRC-2012).¹⁵⁶

2. AIM

The aim of the present PhD thesis was to gain further evidence of APOSEC regenerative effect. APOSEC has been shown to exert cytoprotective, anti-inflammatory, anti-apoptotic and regenerative properties in in vitro cell culture, in vivo in rodents and pig acute myocardial infarction models. In the last decade, due to enhancement of treatment of acute myocardial infarction via introduction of several new invasive coronary therapies, and new medicines, which decreased markedly the mortality of the acute myocardial infarction, the treatment of acute myocardial infarction shifted to treatment of post-infarction chronic heart failure. Our aim was to prove the regenerative effect of APOSEC in a translational model of chronic ischemic left ventricular dysfunction.

Furthermore, as we used the 3D navigation of endocardial mapping, in further experiments we aimed to justify the diagnostic and prognostic value of this percutaneous intramyocardial navigation system.

A. Methodological study: the NOGA endocardial mapping system

- Comparing the performance of the NOGA system with cardiac MRI in their ability to determine infarction size and infarction transmuralty – is the NOGA system a valid tool to guide intramyocardial regenerative substance delivery?

B. Cardiac regeneration using APOSEC in chronic myocardial infarction

- Assessing the efficacy and safety of percutaneous intramyocardial delivery of APOSEC in a clinically relevant porcine model of chronic left ventricular dysfunction in response to myocardial infarction

- Investigation of the effects of APOSEC on haemodynamic function and gene expression profile in chronic left ventricular dysfunction

3. MATERIALS AND METHODS

3.1. Experimental chronic left ventricular dysfunction post MI

For both studies we used a porcine closed-chest reperfused acute MI model (n=60 for the NOGA project and n=22 for the APOSEC study). In female pigs closed-chest reperfused acute MI was produced by percutaneous occlusion of the mid left anterior descending coronary artery (LAD). The animals were sedated by the injection of ketamine hydrochloride (12 mg/kg), xylazine (1 mg/kg), and atropine (0.04 mg/kg) intramuscularly. Following intratracheal intubation animals were anesthetized by the administration of isoflurane (1.5–2.5 vol%), O₂ (1.6–1.8 vol%), and N₂O (0.5 vol%). Blood pressure values, O₂ saturation, and electrocardiography were controlled constantly. In order to perform angiography, a 6F introducer sheath (Terumo Medical Corporation, Somerset, NJ, USA) was inserted via the right femoral artery, which was prepared with a surgical method. Following this, 200 IU/kg of heparin were administered. Next, a balloon catheter (3.0 mm in diameter, 9 mm long; Maverick, Boston Scientific Corp, Natick, MA, USA) was introduced into the LAD to perform a selective angiography of the left coronary artery tree. After identification of the origin of the second major diagonal branch, occlusion of the mid LAD was conducted by ballooninflation at 5 atmospheres. After 90 minutes the balloon was deflated to allow a reperfusion of ischemia-affected myocardium supplied by the mid LAD. The animals were then allowed to recover from the anesthesia.

The trials and the animal experiments were carried out in firm accordance with the recommendations in the Guide for the Care and Use of Laboratory Animals of the National Institutes of Health. The Experimental Animal Care and Use Committee at the Faculty of Animal Science of the University of Kaposvar (Hungary) approved the protocol previously (Permit Numbers: 246/002/SOM2006/11/11 and 246/002/SOM2006/08/11). All procedures were completed under general anesthesia, and the team worked with all efforts to minimize the suffering of the pigs.

3.2. cMRI-LE acquisitions

Sixty days after the induction of acute MI and after development of chronic LV dysfunction, cardiac magnetic resonance imaging (cMRI) with LE was performed. cMRI images were obtained on a 1.5 T Siemens Avanto Syngo B17 clinical scanner (Erlangen, Germany) with a phased-array coil and a vector ECG system. Functional (dynamic) images were obtained by retrospective ECG-gating (HR: 80–100 beats/minute), steady-state free precession technique (SSFP - TRUFISP sequence) in short-axis and long-axis sections of the heart

using 1.2-ms echo time (TE), 40-ms repetition time (TR), 25 phases, 50° flip angle, 360-mm field-of-view, 8-mm slice thickness, and a 256 x 256 image matrix. Delayed enhancement diastolic phase short-axis images were acquired after injection of 0.05 mmol/kg of contrast medium using an inversion recovery prepared gradient-echo sequence, in order to determine the extent of infarct size and its transmural. Additionally, LE images were acquired 10 minutes after the administration of gadolinium contrast agent.

3.3. Analysis and visualization of cMRI images

For all reconstructions, efforts were made to include the entire heart volume (from the apex to the level of the great vessels), so that the complete left ventricle was integrated in the MRI analysis. The examination was constantly limited to image slices including the myocardium of the left ventricle in 360 degrees. Image analysis was conducted by applying the Segment for Windows software (version 1.9; Medviso AB, Lund, Sweden).¹⁶² Infarction size and transmural were determined semi-automatically in the 10-minute LE images using the “2SD” approach. During this process, hyperintense image pixels were tagged as infarcted if their signal intensity (SI) was greater than the mean value plus 2 standard deviations of the normal-appearing LV myocardium. Signal intensity was derived from the absolute value of the voxel intensity data, which were stored in the DICOM files from the cMRI-LE acquisitions.

The 3D volume of the infarct was assessed in both absolute units and also as a percentage of the total LV myocardial volume. In order to gain a precise volume determination the entire LV was evaluated by both imaging modalities (NOGA and cMRI-LE). The non-contractile mitral valve areas were ignored for the evaluation of infarct size and transmural.

By using segmental transmural data from the infarct segmentations polar plots were constructed. To realize the same apex, heart axis, and orientation as for NOGA maps the analogous bull’s eye maps were processed.

For these reconstructions, myocardial viability data were interpolated and smoothed from a total of 8 apico-basal segments and 32 wall sectors per segment. To facilitate the interpretation of the images the linear borders of 17 segments were overlaid graphically using the “classical” segmental nomenclature. The endo- and epicardial borders were segmented, and a segmental model was fitted on the left ventricle model (32 sections per slice). Using the standard transmural analysis feature of the Segment software (Medviso Inc., Lund, Sweden), the midline was determined for each segment of the left ventricle. The transmural of the infarct is given as the radial projection of the segmented scar volume on the midline, summed for each section.

By applying two-dimensional planimetry to the polar plots, we performed two distinct measurements of the transmural extent of the infarct. The extents of the transmural or non-transmural infarct and normal areas were defined as the percentage of segments in which the SI was >75% (infarct core), 51–75% (border zone of infarction), 25–50% (non-transmural infarction), or <25% (normal).¹⁶³ Alternatively, SI >60% was defined as transmural infarct, 31–60% as non-transmural infarct, and <30% as a normal area.¹⁶⁴ To calculate the areas, we used the raw transmural data from 32 sections per slice, as noted above. All MRI area measurements are reported as the percentage of segments in the threshold range divided by the total number of segments.

Dynamic MR images were analyzed for myocardial wall movement and functional parameters. We carried out semi-automatic segmentation of the LV endocardial and epicardial borders while the end-diastolic volume (EDV), end-systolic volume (ESV), global LV ejection fraction (EF), and cardiac output (CO) were calculated automatically on short-axis images.

3.4. NOGA® electroanatomical mapping of the LV

The electromechanical maps of the pigs were acquired 62±1 days after acute MI (2±1 days after cardiac MRI). The principles and procedures of NOGA electroanatomical mapping have been described previously.¹⁶⁵ Briefly, the external reference patch containing a tip sensor, was fixed onto the pig's back right below the heart. The left femoral artery was surgically prepared and a 7 F introducer sheath was laid. Next, 5000 IU of unfractionated heparin were administered. A NogaStar® (Johnson & Johnson, Diamond Bar, California) mapping catheter was introduced through the femoral sheath and was advanced inside the aorta under fluoroscopic guidance. Next, the NOGA catheter was bent and advanced into the LV through the atrioventricular valve. Once the catheter was located inside the LV chamber, the tip of the catheter was straightened and angled towards the apex. In order to initiate a three-dimensional shape of the heart a few endocardial points in several areas of the LV chamber (the very apical point, regions of the outflow tract, as well as lateral and posterior wall points) were acquired. With subsequent assessments of newer points the heart silhouette was then updated in real, which further facilitated electromagnetic navigation with reduced use of fluoroscopic radiation.

In each of the twelve myocardial segments at least four points were sampled. Throughout the course of electromechanical mapping, unipolar and bipolar electrocardiograms along with the exact 3D localization and orientation of the catheter tip in relation to the LV chamber were measured simultaneously. At the same time the stability of the catheter-to-wall contact was

weighed at every location in real time, and merely stable measurement points were accepted. Both electrophysiological and regional data were then combined to generate a color-coded 3D reconstruction of the LV chamber. For the creation of the 3D maps the apex-LV chamber longitudinal axis was defined carefully. As additional information, the end-diastolic, end-systolic volumes and global ejection fraction could be calculated by the evaluation of the movement of the catheter tip, and also the average heart rate could be assessed.

3.5. Evaluation of the NOGA® maps

To quantify the relative size of the area of interest we used the ImageJ for Windows software (U.S. National Institutes of Health [NIH], Bethesda, Maryland, USA). For this purpose, the 3D unipolar (UPV) and bipolar (BiPV) voltages were presented as two-dimensional polar maps. Discriminatory threshold values were used in equal manner for all NOGA® maps: <5 mV for non-viable infarcted area, 5-15 mV for infarct border zone and >15 mV for normal viability in unipolar maps and <0.8 mV for transmural, 0.8-1.9 mV for non-transmural infarction and >1.9 mV for normal myocardium in bipolar maps. These cut-off values are represented by the color-coding of the NOGA® images to enable the identification of myocardial regions with decreased UPVs and BiPVs (Table 1, Figure 24). To validate the threshold values used for discrimination for bipolar NOGA® maps, the correlation between with MRI-based infarct area measurements and NOGA measurements at various discriminatory bipolar threshold values was calculated. First, the raw images of the NOGA® transmural data (bipolar recordings) into the image processing pipeline of Matlab R2010 for Windows were exported and then image RGB (red-green-blue) color values were converted into voltage values; the image was then cropped to the cMRI-LE infarct area. Using 100 threshold steps from 0.5 to 1.5 mV we iteratively exported the NOGA®-based transmural areas to the cMRI transmural maps and determined the correlation coefficient between the two images using different thresholds (25, 30, 50, 60 and 75% transmural) (Figure 25A).

In order to establish the BiPV cut-off that offers optimal fit to the size of transmural and non-transmural cMRI-LE areas, we also evaluated 0.5–1.5 mV and 1.0–2.0 mV BiPV cut-offs (Figure 26). The relative extent of the infarct core zone, border regions, and areas representing normal myocardium were determined from the color-coded unipolar voltage polar map, and the extent of the transmural and non-transmural infarction were demarcated on the bipolar maps (Figures 27 and 28). The delineation and analysis of these regions on the NOGA® maps was performed by an investigator blinded to the results of the cMRI-LE.

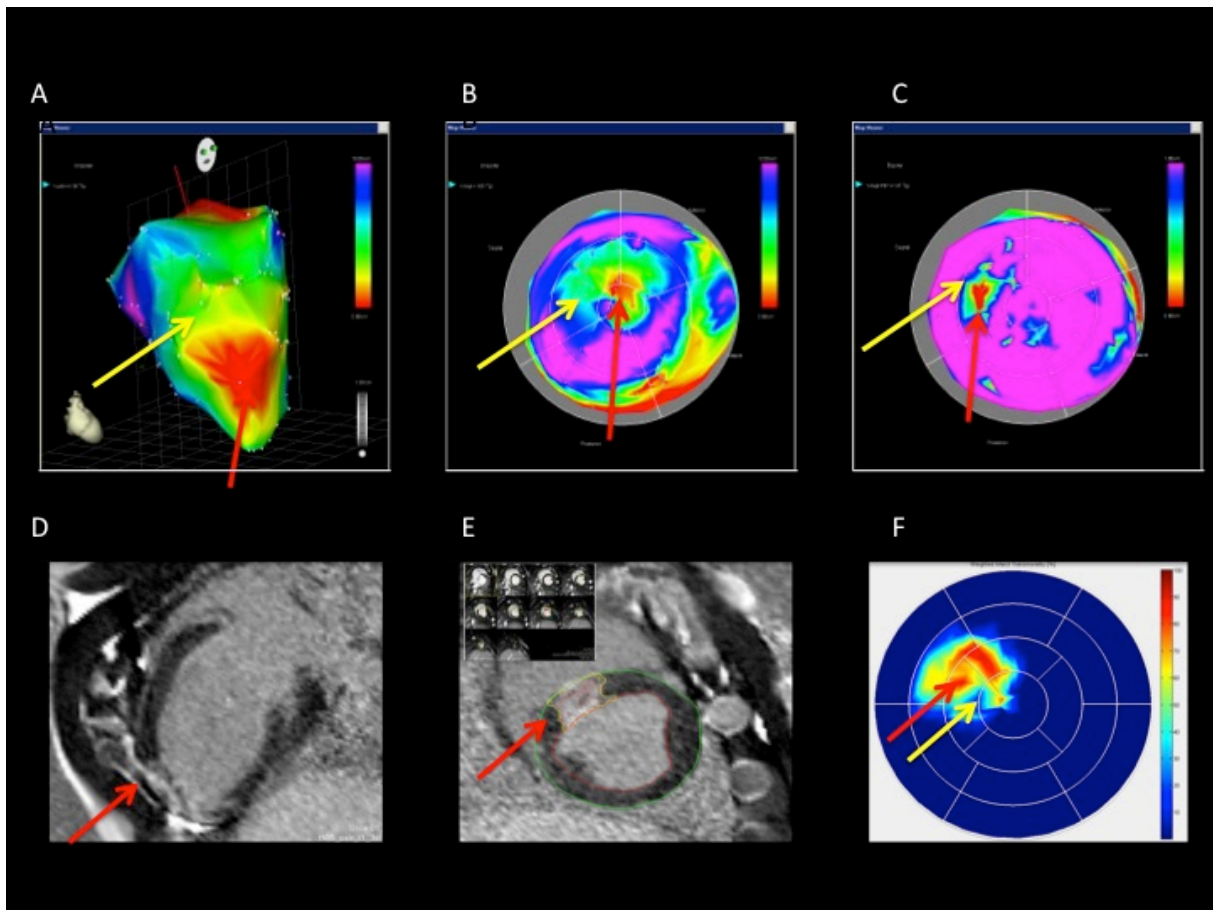


Figure 24. NOGA® endocardial mapping and cardiac magnetic resonance imaging (cMRI) of a pig with chronic myocardial ischemia.

- A. 3D NOGA® maps displaying the anterior, anteroseptal, and apical myocardial infarction. Red colour shows the infarct core (red arrow), the surrounding green-yellow area indicates the border zone of infarction (yellow arrow).
- B. The corresponding unipolar voltage polar map. The color-coding is identical to A.
- C. The bipolar voltage polar map of the same animal. Red colour shows transmural infarction (red arrow); yellow-green colour specifies the non-transmural infarction (yellow arrow), and blue-pink colour indicates normal myocardium.
- D. cMRI with LE long axis image shows the myocardial scar (red arrow).
- E. cMRI with LE short axis images with myocardial infarction (red arrow). Determination of infarction size was assessed by splitting of the myocardium to 8 parts from the basis of the heart to the apex (left upper corner).
- F. cMRI transmurality polar map indicating transmural infarction (red arrow) with a proximate area of non-transmural infarction (yellow arrow).

Table 1. NOGA® endocardial unipolar and bipolar map-derived cut-off values.

Cut-off value	Color on the NOGA® map	Definition
Unipolar voltage map		
>15 mV	Blue, violet	Normal tissue
5–15 mV	Yellow, green	Border zone of infarction
<5 mV	Red	Area of myocardial infarction
Bipolar voltage map		
>1.9 mV	Blue, violet	Normal tissue
0.8–1.9 mV	Yellow, green	Non-transmural infarction
<0.8 mV	Red	Transmural infarction

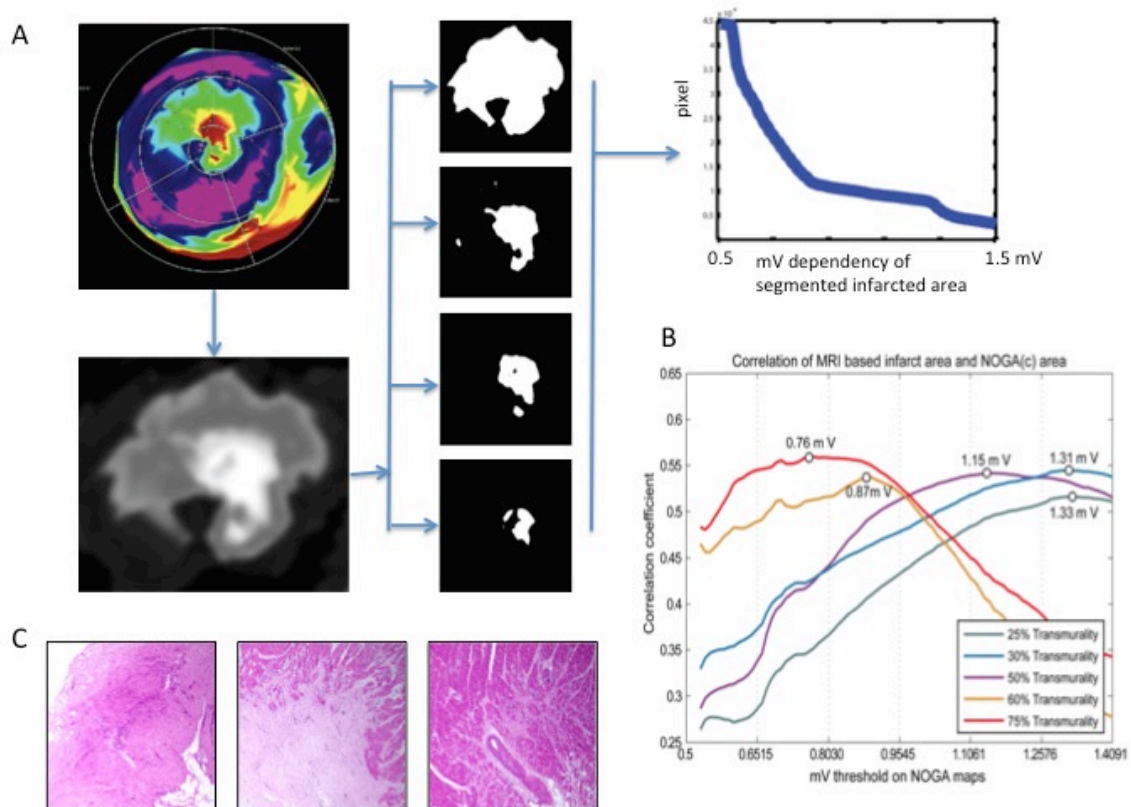


Figure 25. Magnet resonance imaging-derived NOGA© bipolar threshold values for infarct transmurality.

- A. Iterative thresholding of voltage maps (left panel): the original reconstructed NOGA© maps were cropped to infarct area converted to mV scale, images were then iteratively thresholded from 0.5 to 0.5 mV using a total of 100 steps. The mid panels shows examples of the process. The right panel indicates the relation between area of infarct and mV threshold applied.
- B. Voltage-threshold dependence of the correlation between different NOGA and MRI areas. The maximal value of an obtainable correlation coefficient is illustrated for each threshold.
- C. Correlates histological findings for transmural (upper) and non-transmural (mid) infarction and normal myocardium (bottom), cut from the areas of bipolar voltage values below 0.8 mV, between 0.8-1.9 mV and above 1.9 mV, with corresponding cMRI-LE transmuralities values of >75%, 50% and <24%, respectively.

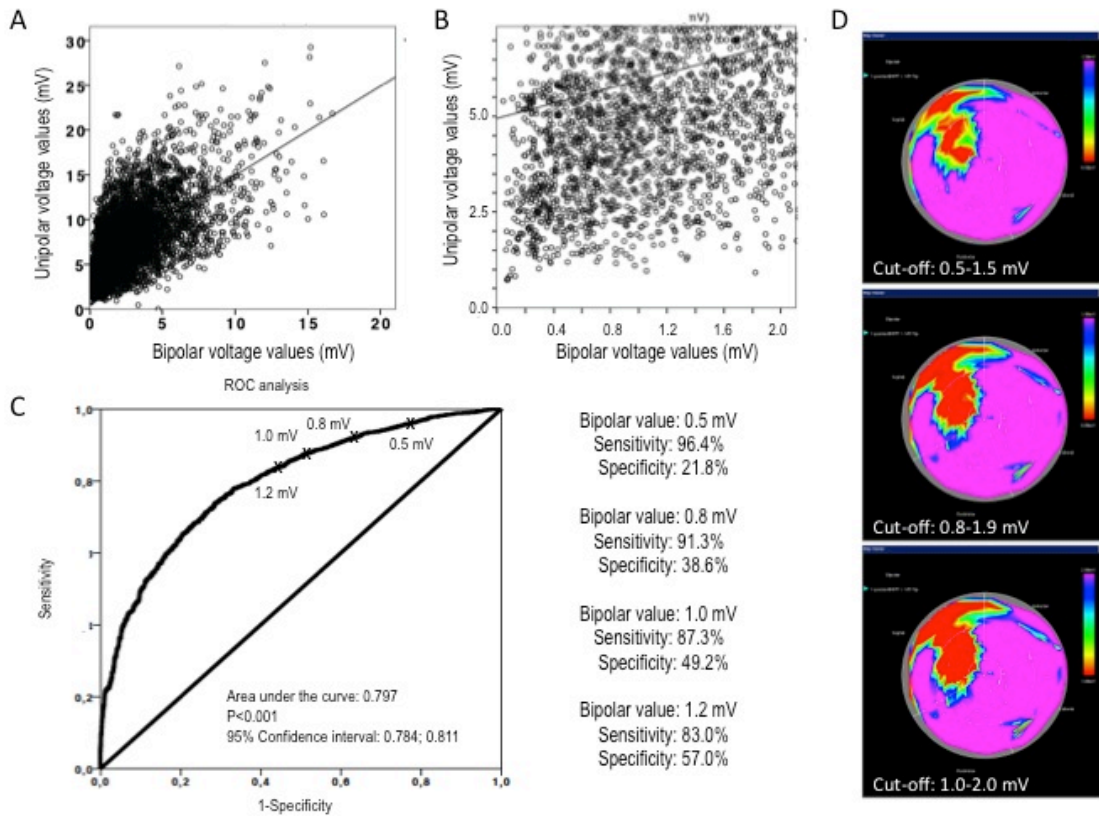


Figure 26. Determination of the bipolar voltage (BiPV) cut-off value for calculating the transmural and non-transmural infarct size using unipolar voltage values (UPV).

- A. Scatter plot with linear correlation between UPV and BiPV.
- B. Part of the scatter plot displaying the non-viable range defined as UPV < 5 mV.
- C. Receiver operator characteristics curve for the assessment of different BiPV cut-off values.
- D. Examples of bipolar maps with different cut-offs values.

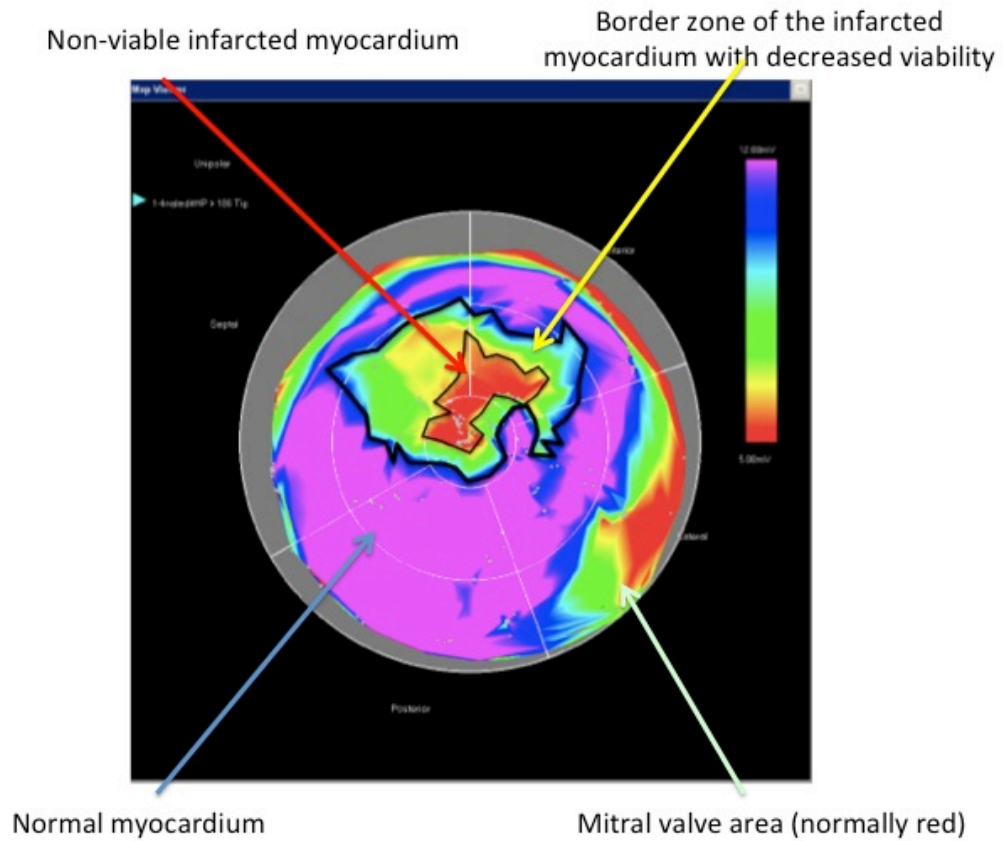


Figure 27. Schematic illustration of the planimetric calculation of the size of the infarct core and the size of the border zone of the infarction with decreased viability in the NOGA® endocardial mapping.

Red colour shows the infarct core region, and green-yellow colour depicts the proximate area with reduced viability.

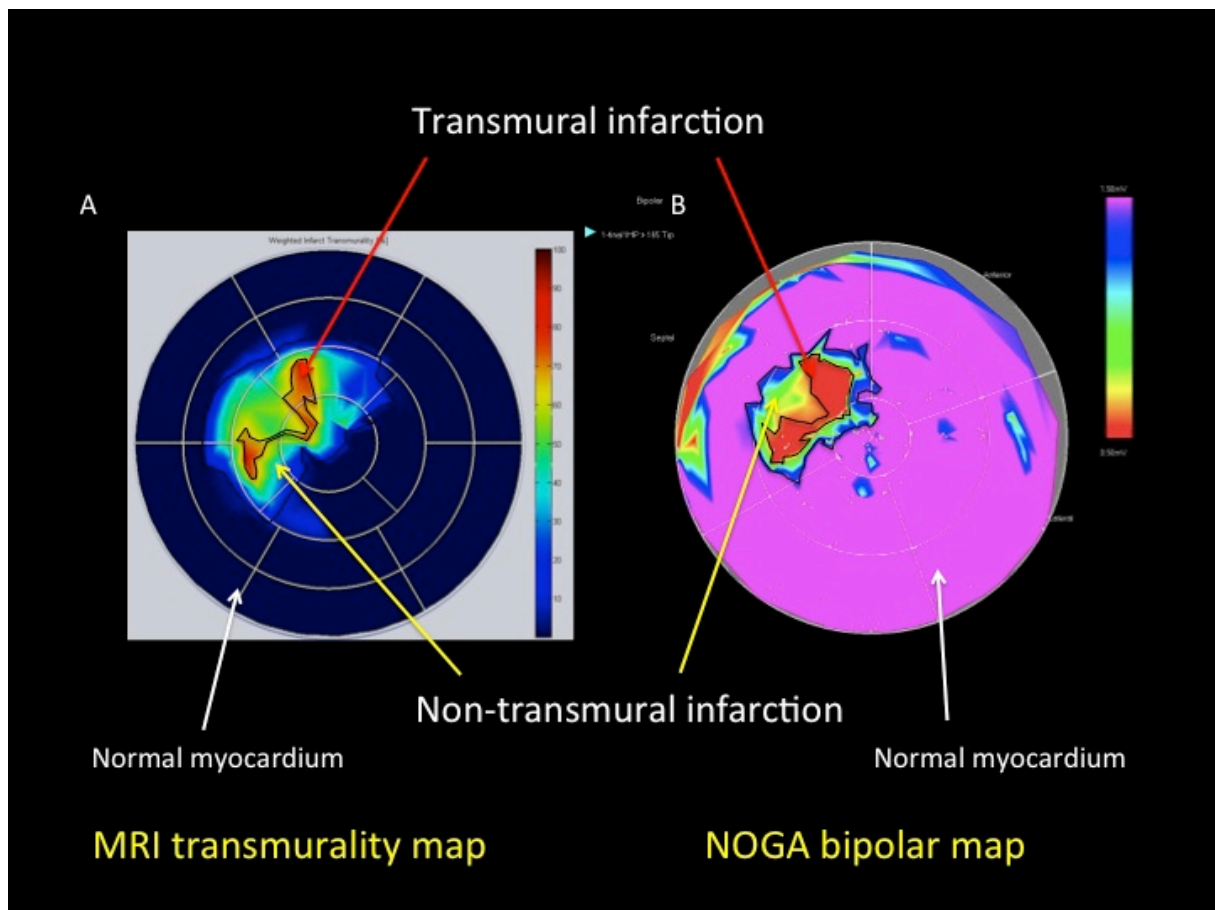


Figure 28. Schematic illustration of the planimetric calculation of the transmural and non-transmural infarct sizes as shown in polar maps from cardiac magnetic resonance imaging (cMRI) and NOGA® endocardial mapping.

- A. Planimetric determination of the extent of the transmural and non-transmural infarction from cMRI.
- B. Planimetric determination of the extent of the transmural and non-transmural infarction from a NOGA® bipolar voltage map.

3.6. Overlap ratio

The following equation was used for determination of the overlap ratio between the cMRI and NOGA® bipolar transmural maps¹⁶⁶ (Figure 29):

$$\text{(NOGA® bipolar map overlap area + cMRI transmural map overlap area) / (NOGA® bipolar low voltage area + cMRI transmural area)}$$

For the overlap ratio of the transmural, non-transmural and the combined transmural and non-transmural (not normal) areas the following cut-off values were used:

- Transmurality overlap ratio: between a NOGA® bipolar map area with BipV <0.8 mV and a cMRI transmural area with SI >75%;
- Non-transmural areas overlap ratio: between a NOGA® bipolar map area with BipV 0.8-1.9 mV and a cMRI transmural area with SI 25-75%;
- Combined transmural and non-transmural (not normal) area overlap ratio: between a NOGA® bipolar map area with BipV <1.9 mV and a cMRI transmural area with SI >25% (Figures 26 and 27).

A result of >60% overlap was considered good accuracy¹⁶⁶, and 50–60% of overlap was considered moderate accuracy (these values are arbitrary).

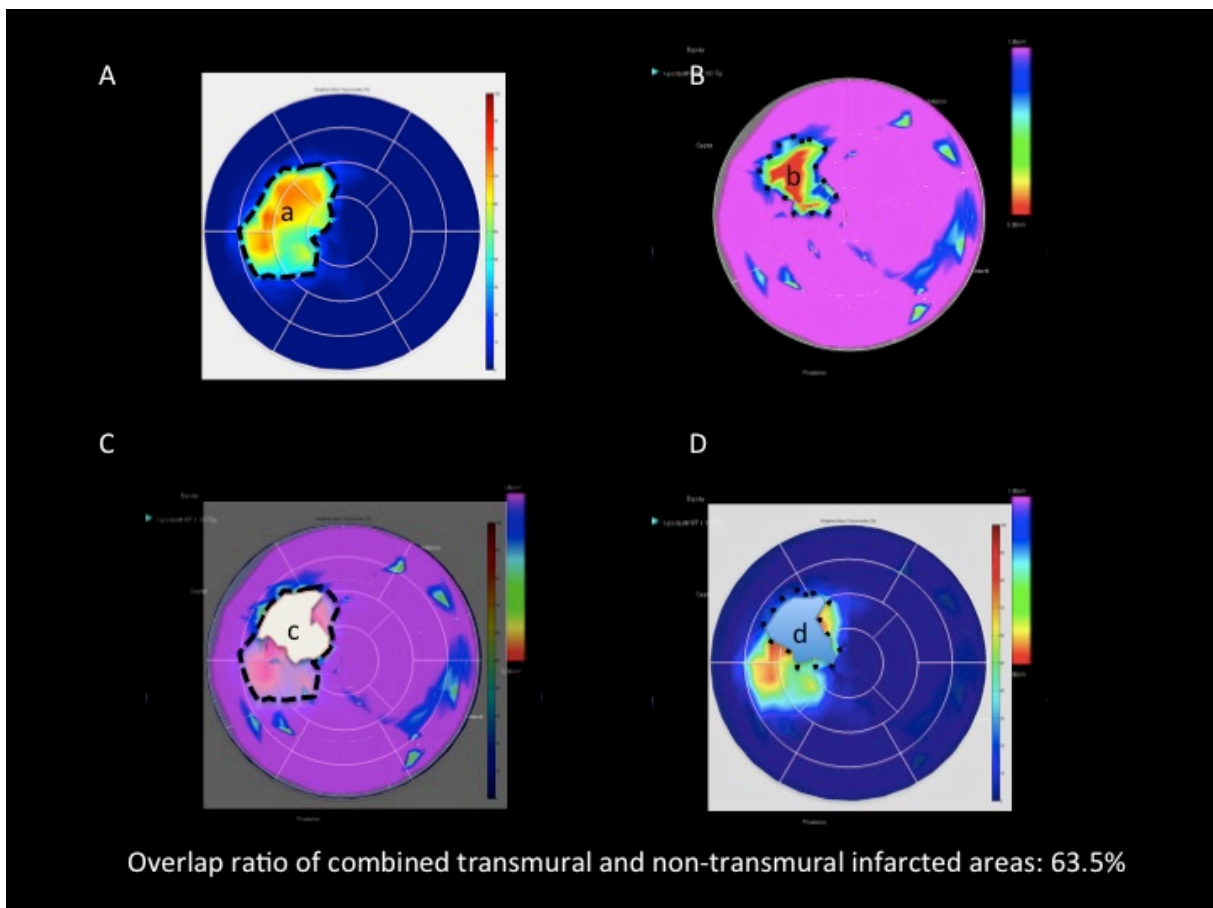


Figure 29. Calculation of the overlapping ratio of the transmural plus the non-transmural infarction by cardiac magnetic resonance imaging (cMRI) and NOGA® endocardial mapping.

- A. cMRI transmural polar map.
- B. NOGA® bipolar polar map.
- C and D. Overlap of the cMRI and NOGA® polar maps.

a: The size of the transmural and non-transmural infarction by cMRI; b: the size of transmural and non-transmural infarction by NOGA® bipolar mapping; c: overlap of the NOGA® bipolar infarct shape on a cMRI polar map; d: overlap of the cMRI infarct shape on a NOGA® bipolar map. The overlapping ratio was calculated as follows: $(c+d)/(a+b)$.

3.7. Histology for the NOGA-MRI study

Samples of myocardial tissue were obtained from transmural and non-transmural infarction areas as well as from normal myocardium, corresponding to the regions of bipolar voltage values below 0.8 mV, between 0.8 and 1.9 mV and above 1.9 mV, and analogous cMRI-LE transmural values of >75%, 50% and <24%, respectively. The samples were stored in 4.5% formalin for at least 24h and then embedded in paraffin. Samples were sectioned into 4-6 µm thick slices and stained with haematoxylin-eosin.

3.8. Generation of cell culture medium from irradiated porcine PBMC for in vivo experiments (APOSEC)

Blood was gained from the animals by direct cardiac puncture. Briefly, three animals were anesthetized by an IV bolus of 10 mg/kg ketamine and 1.3 mg/kg azaperone. Direct heart puncture was done after left thoracic dermal incision was made under sterile conditions using a hollow needle. Blood drawn with 50-ml syringes was then transferred into prepared heparinized plastic bags for blood products. PBMCs were isolated by Ficoll-Paque density gradient centrifugation (GE Healthcare Bio-Sciences AB, Sweden). The apoptosis of PBMC was induced by 60-GY Cesium-137 irradiation (Department of Transfusion Medicine, General Hospital, Vienna). The irradiated cells were cultured with serum-free UltraCulture Medium (Lonza, Switzerland) for 24h until a cell density of 25×10^6 . After that the cells were discarded and the supernatant was obtained. Supernatants were dialyzed against 50 mM ammonium acetate for 24h at 4°C. The acquired liquid was sterile filtered (Whatman Filter 0.2 µm FP30/0.2 Ca-S, Dassel, Germany), frozen, and lyophilized overnight (Lyophilizator Christ alpha 1-4, Martin Christ Gefriertrocknungsanlagen GmbH, Osterode am Harz, Germany). Lyophilized APOSEC aliquots derived from 1.5×10^9 PBMCs were stored at -80°C until the animal experiments were performed.

3.9. Percutaneous intramyocardial delivery of APOSEC or medium solution using 3D NOGA guidance

At day 30 after acute MI after the development of LV remodeling, the animals were sedated and intubated. The patency of the mid LAD was confirmed by coronary angiography. LV hemodynamic parameters were measured by a pigtail catheter. We performed NOGA endocardial mapping using a percutaneous NOGA Star catheter (Cordis, Johnson & Johnson, Miami Lakes, FL, USA) as described previously.¹⁶⁵ After creation of the 3D silhouette of the LV depicting the infarction, the diagnostic NOGA Star catheter was switched to a NOGA MyoStar injection catheter (Cordis, Johnson & Johnson). The pigs were randomized to intramyocardial injections and received either APOSEC (derived from 2.5×10^9 PBMCs, resuspended in 4 ml physiologic saline, 300- μ l aliquots) or medium as a control (resuspended lyophilized Cell Growth medium) in 11 ± 1 locations of the border zone of infarction using 3D NOGA-guided percutaneous intramyocardial delivery. The animals were then allowed to recover from the procedure. At day 60 post MI (30 days post intramyocardial injections), control coronary angiography and NOGA endocardial mapping were conducted under general anesthesia.

3.10. Cardiac magnetic resonance imaging (cMRI) for area at risk, microvascular obstruction 3 days post-AMI

For the animals in the APOSEC study, cardiac MRI with LE was performed at day 3 and day 60 after reperfused acute MI using a 1.5-T clinical scanner (Avanto, Siemens, Erlangen, Germany) with a phased-array coil and a vector ECG system (Chapters 3.2 and 3.3.). The area at risk and microvascular obstruction were calculated for cMRI at day 3.¹⁶²

3.11. LV hemodynamic measurements

During coronary angiography, LV hemodynamic measurements were done using a pigtail catheter. The systolic aortic pressure, LV end-systolic (ESP) and end-diastolic pressures (EDP), as well as LV contractility expressed as dP/dt and dP/dt/P, and the LV end-diastolic stiffness (LV EDP/EDV) were assessed.

3.12. Myocardial viability, infarct transmuralty and regional functional assessment by NOGA

The mean unipolar, bipolar, and local linear shortening values (UPV, BiPV, and LLS) of the injected areas were measured by the 12-segment polar map analysis principles. The results were stated as mV or %, respectively.

3.13. Histology for the APOSEC study

The hearts were explanted at day 60 and representative tissue samples of normal, border zone and infarcted areas were obtained. Tissue specimens were first fixed in 10% neutral buffered formalin, then embedded in paraffin, sectioned, and stained for haematoxylin-eosin and angiogenic marker of CD31 and stem cell factor CD117. Additionally, immunofluorescence staining of the small capillaries was performed using monoclonal mouse anti-pig CD31 and CD117 antibody (ABD Serotec, Kidlington, UK) and goat anti-mouse IgG as the secondary antibody (DyLight, Rockford, IL, USA). Histological sections were counterstained with DAPI (Thermo Scientific, Rockford, IL, USA). Samples were mounted in Vectashield with 4',6-diamidino-2-phenylindole (DAPI) (Vector Laboratories, Burlingame, CA). Native and fluorescence images were taken on an Axiophot-II microscope (Carl Zeiss; Jena/Oberkochen, Germany) that was connected to a CCD camera (Hamamatsu Photonics; Hamamatsu City, Japan) using Open Lab 2.0.9 software (Improvision, Coventry, UK). The number of CD31, CD117 and DAPI positive cells in border zone, and infarcted tissues were counted on 5 sections per slide (3x5 slides per heart) using $\times 400$ magnification. The ratio of CD31/DAPI and CD117/DAPI were determined and given as percentages.

3.14. Gene expression analysis using RNA microarrays and real time PCR (rtPCR)

For RNA extraction heart tissue specimens were collected from the infarct core area, the border zone, and the unaffected myocardium. Tissue samples were stored in RNAlater (Qiagen, Germany) at -20°C . Total RNA was isolated from the samples using the RNeasy Microarray Tissue Mini Kit (Qiagen, Germany) according to the manufacturer. RNA quality was tested on RNA Nano chips using the Agilent 2100 Bioanalyzer platform (Agilent Technologies).

3.15. RNA microarrays

Transcriptomics analysis using microarrays was performed by Miltenyi (Miltenyi Biotec GmbH, Germany). Briefly, 100ng of each total RNA sample was used for the linear T7-based amplification step. The RNAs were amplified and labeled using the Agilent Low Input Quick Amp Labeling Kit (Agilent Technologies) to produce Cy3-labeled cRNA. An ND-1000 Spectrophotometer (NanoDrop Technologies) was used to measure cRNA and the dye-incorporation rate. Hybridization was performed using the Agilent 60-mer oligo microarray protocol and the Agilent Gene Expression Hybridization Kit (Agilent Technologies). Briefly, 1.65 μg of Cy3-labeled fragmented cRNA in hybridization buffer was hybridized for 17 hours at 65°C to Agilent Whole Sus scrofa Genome Oligo Microarrays 4x44K V2 using

hybridization chambers in an oven. The microarrays were then washed with Agilent Gene Expression Wash Buffer 1 at room temperature for 1 min, and a second wash was performed with preheated (37°C) Agilent Gene Expression Wash Buffer 2 for 1 min. The fluorescence signals of the hybridized Agilent Microarrays were measured using Agilent's Microarray Scanner System (Agilent Technologies) and analyzed using Agilent Feature Extraction Software (FES).

Raw hybridization values were loaded into R (GNU R) using the R-package limma (v3.14.4). Microarray data have been uploaded to the Gene Expression Omnibus database (<http://www.ncbi.nlm.nih.gov/geo/query/acc.cgi?acc=GSE47397>). Biological interpretation of significant gene lists was performed using the Database for Annotation, Visualization and Integrated Discovery (DAVID) v6.¹⁶⁷ Data were reported in annotational clusters or as single gene expression, heat maps, and Venn diagrams.

3.16. *rtPCR of selected genes*

The mRNA of myocardial samples from different regions and both groups of animals was reverse transcribed to cDNA (Qiagen, Germany) and expression of mRNA of interest was quantified by rtPCR (Applied Biosystems 7500 Real-Time PCR System, Life Technologies, USA). The primers for the target sequences were designed using Primer3 software (http://primer3.wi.mit.edu/primer3web_help.htm; Microsynth, Switzerland) (Table 2). The expression rates of the target genes were normalized to the geometric means of the housekeeping genes GAPDH, HPRT1, and PPIA. The relative gene expression level was calculated using the ΔC_t method (i.e. expression level relative to an endogenous control). The expression changes were calculated relative to expression levels in the normal myocardium of the same animal.

Table 2. List of the primers used for rtPCR.

Gene	Name	Accession number	Forward sequence (5'-3')	Reverse sequence (5'-3')	Amplicon [bp]	E [%]
HPRT1	Hypoxanthine		CCC AGC GTC GTG ATT	ATC TCG AGC AAG CCG	131	89
	phosphoribosyltransferase 1	NM_001032376.2	AGT GA	TTC AG		
PPIA	Peptidylprolyl isomerase A		GTC TTC TTC GAC ATC GCC	TCC TTT CTC CCC AGT	120	95
	(cyclophilin A)	NM_214353.1	GT	GCT CA		
GAPDH	Glyceraldehyde-3-phosphate		TCC ACC CAC GGC AAG	ATG TTG GCG GGA TCT	104	109
	dehydrogenase	NM_001206359.1	TTC CAC	CGC TCC T		

HIF1alpha	Hypoxia inducible factor 1, alpha subunit	NM_001123124.1	ACC TGA GCC TAA CAG TCC CAG TG	TTC TTT GCC TCT GTG TCT TCA GCA A	114	88
MMP9	Matrix metalloproteinase 9	NM_001038004.1	CGG GAG ACC TAC GAA CCA AT	TTT CTG TCG GTC ATC TCG GC	97	108
CASP3	Caspase 3, apoptosis- related cysteine peptidase	NM_214131.1	GGG ATT GAG ACG GAC AGT GG	TGA ACC AGG ATC CGT CCT TTG	136	95
CxCl12	Chemokine (C-X-C motif) ligand 12	NM_001009580.1	GTG GCA CGG CTG AAG AGC AAC	GGC CCG AGA GAG TGG GAC TGG	112	91
MEF2C	Myocyte enhancer factor 2C	NM_001044540.1	TAA CAT GCC GCC ATC CGC CC	ATC CTC TCG GTC GCT GCC GT	151	97
MYOG	Myogenin (myogenic factor 4)	NM_001012406.1	GCC AGG GGT GCC CAG TGA ATG	ATG ATC CCC TGG GTT GGG GC	94	121
GATA4	GATA binding protein 4	NM_214293.1	AGA AAA CGG AAG CCC AAG AAC	CCA CAC TGC TGG AGT TGC TG	109	95
TGFBR3	Transforming growth factor, beta receptor III	NM_214272.1	ATG GAC CTC TAC ACC ACG GA	CGA GTA CGG GGA GAT GAA GC	153	95

3.17. Statistics

Continuous variables are presented as mean values \pm standard deviation.

The correlation between NOGA®- and cMRI-derived parameters was calculated by linear regression analysis indicating Pearson correlation coefficients and Bland-Altman plots. The analysis was carried out by the Matlab R2010 software for Windows. For the iterative fitting of the linear function, a “least absolute residual” robust regression approach was used. We used a the standardized nomenclature for the interpretation of the correlations between the images of the two methods: large for a correlation coefficient greater than 0.5, moderate for 0.5-0.3, and small for 0.3-0.1. In order to choose the best BiPV cut-off value for determining the transmural and non-transmural scars, all UPVs were correlated with the corresponding BiPVs using linear regression analysis. Using a 5 mV UPV value as the cut-off for viability/non-viability, receiver operator curve (ROC) analysis was performed, and the sensitivity, specificity of different BiPV values, and the area under the curve, with 95% confidence intervals, were calculated.

In the APOSEC study, comparisons between the treatment and sham groups were tested using the Student's *t* test for continuous variables and the χ^2 test for categorical variables. Data analysis was conducted by an experienced researcher blinded to randomization and study results. Statistical analysis was carried out using the SPSS 18.0 (SPSS Inc, USA) software. For gene array analysis, to test for all comparisons (i.e. differences between regions of interest: normal, border, and infarct and APOSEC vs. control) a linear model for each gene was fitted and the estimated coefficients and standard errors for these contrasts were computed. Subsequently, moderated t-statistics, moderated F-statistics, and the log-odds of differential expression were calculated by empirical Bayes shrinkage of the standard errors towards a common value. False discovery rates (FDR) below 5% were considered statistically significant for each comparison. Higher FDR cut-offs were used for some contrasts, especially for the use of the gene lists for biological interpretation. Unsupervised hierarchical clustering was performed with the Euclidean distance as the distance function and the Ward algorithm in R, using centered and scaled log₂ expression values. Principal Component Analysis (PCA) was also performed for centered and scaled values.

For all statistical analyses, a p-value <0.05 was considered statistically significant.

4. RESULTS

4.1. COMPARISON OF NOGA ENDOCARDIAL MAPPING AND CARDIAC MAGNETIC RESONANCE IMAGING FOR DETERMINING INFARCT SIZE AND INFARCT TRANSMURALITY FOR INTRAMYOCARDIAL INJECTION THERAPY USING EXPERIMENTAL DATA



Comparison of NOGA Endocardial Mapping and Cardiac Magnetic Resonance Imaging for Determining Infarct Size and Infarct Transmurality for Intramyocardial Injection Therapy Using Experimental Data

Noemi Pavo¹, Andras Jakab², Maximilian Y. Emmert^{3,4,5}, Georg Strebinger¹, Petra Wolint^{3,4,5}, Matthias Zimmermann⁶, Hendrik Jan Ankersmit^{6,7}, Simon P. Hoerstrup^{3,4,5}, Gerald Maurer¹, Mariann Gyöngyösi^{1*}

1 Department of Cardiology, Medical University of Vienna, Vienna, Austria, **2** Department of Biomedical Imaging and Image-guided Therapy, Medical University of Vienna, Vienna, Austria, **3** Swiss Centre for Regenerative Medicine, University of Zürich, Zürich, Switzerland, **4** Division of Surgical Research, University Hospital of Zürich, Zürich, Switzerland, **5** Clinic for Cardiovascular Surgery, University Hospital of Zürich, Zürich, Switzerland, **6** Department of Thoracic Surgery, Medical University of Vienna, Vienna, Austria, **7** Christian Doppler Laboratory for Cardiac and Thoracic Diagnosis and Regeneration, Vienna, Austria

Abstract

Objectives: We compared the accuracy of NOGA endocardial mapping for delineating transmural and non-transmural infarction to the results of cardiac magnetic resonance imaging (cMRI) with late gadolinium enhancement (LE) for guiding intramyocardial reparative substance delivery using data from experimental myocardial infarction studies.

Methods: Sixty domestic pigs underwent diagnostic NOGA endocardial mapping and cMRI-LE 60 days after induction of closed-chest reperfused myocardial infarction. The infarct size was determined by LE of cMRI and by delineation of the infarct core on the unipolar voltage polar map. The sizes of the transmural and non-transmural infarctions were calculated from the cMRI transmural map using signal intensity (SI) cut-offs of >75% and >25% and from NOGA bipolar maps using bipolar voltage cut-off values of <0.8 mV and <1.9 mV. Linear regression analysis and Bland-Altman plots were used to determine correlations and systematic differences between the two images. The overlapping ratios of the transmural and non-transmural infarcted areas were calculated.

Results: Infarct size as determined by 2D NOGA unipolar voltage polar mapping correlated with the 3D cMRI-LE findings ($r = 0.504$, $p < 0.001$) with a mean difference of 2.82% in the left ventricular (LV) surface between the two images. Polar maps of transmural cMRI and bipolar maps of NOGA showed significant association for determining of the extent of transmural infarction ($r = 0.727$, $p < 0.001$, overlap ratio of $81.6 \pm 11.1\%$) and non-transmural infarction ($r = 0.555$, $p < 0.001$, overlap ratio of $70.6 \pm 18.5\%$). NOGA overestimated the transmural scar size (6.81% of the LV surface) but slightly underestimated the size of the non-transmural infarction (-3.04% of the LV surface).

Conclusions: By combining unipolar and bipolar voltage maps, NOGA endocardial mapping is useful for accurate delineation of the targeted zone for intramyocardial therapy and is comparable to cMRI-LE. This may be useful in patients with contraindications for cMRI who require targeted intramyocardial regenerative therapy.

Citation: Pavo N, Jakab A, Emmert MY, Strebinger G, Wolint P, et al. (2014) Comparison of NOGA Endocardial Mapping and Cardiac Magnetic Resonance Imaging for Determining Infarct Size and Infarct Transmurality for Intramyocardial Injection Therapy Using Experimental Data. PLoS ONE 9(11): e113245. doi:10.1371/journal.pone.0113245

Editor: Joshua M. Hare, University of Miami Miller School of Medicine, United States of America

Received: February 26, 2014; **Accepted:** October 21, 2014; **Published:** November 19, 2014

Copyright: © 2014 Pavo et al. This is an open-access article distributed under the terms of the Creative Commons Attribution License, which permits unrestricted use, distribution, and reproduction in any medium, provided the original author and source are credited.

Funding: This study was sponsored by the Christian Doppler Laboratory for Cardiac and Thoracic Diagnosis and Regeneration, Vienna, Austria; by the Ludwig Boltzmann Institute Cluster of Cardiovascular Diseases; and by the Swiss Centre for Regenerative Medicine, University of Zurich, Zurich, Switzerland. The funders had no role in study design, data collection and analysis, decision to publish, or preparation of the manuscript.

Competing Interests: The authors have declared that no competing interests exist.

* Email: mariann.gyongyosi@meduniwien.ac.at

Introduction

The border zone of myocardial infarction (MI) represents myocardial areas with decreased viability and reduced wall motion capacity. Perfusion and transport of cell-death waste products, such as oxygen radicals and other metabolic substances, is impaired due to the close proximity to the non-perfused infarcted area, and this may account for the functional decline. These areas

are targeted by cardiac regenerative therapies because regenerative cells delivered to these areas may survive and help restore cardiac function.

Compared to intracoronary or intravenous delivery, intramyocardial delivery of regenerative drugs, genes, or cells into the border zone of chronic myocardial ischemia results in higher retention of the applied substances, which may result in more

effective therapy [1–4]. However, accurate real-time localization of this area for application of intramyocardial regenerative therapy remains a challenge. Cardiac magnetic resonance imaging (cMRI) with late gadolinium enhancement (LE) is the gold standard for assessing myocardial infarct size, infarct transmural, and left ventricular (LV) function and for assessing the efficacy of cardiac therapies [5,6]. Identification of subendocardial or non-transmural infarcted areas using cMRI-LE would be ideal for guiding targeted intramyocardial regenerative therapy. However, cMRI is an off-line imaging modality, and there is a delay between diagnostic imaging and application of the therapy. Further, cMRI is contraindicated for patients with cMRI-non-compatible pacemakers or implantable defibrillators.

Three-dimensional (3D) NOGA endocardial mapping and electromagnetic guided percutaneous intramyocardial therapy is the method that is currently used for real-time (on-table) assessment of myocardial viability and for delineation of the infarct and infarct border zone [7–10]. The accuracy and reproducibility of NOGA maps for evaluating myocardial viability have been established [11–15], and this 3D imaging method has been compared with other 3D imaging methods such as myocardial scintigraphy, positron emission tomography, and cMRI [16–20]. Furthermore, histology, echocardiography, and other methods have confirmed that NOGA mapping can be used to correctly assess the size and severity of myocardial necrosis [21]. In order to assess the accuracy of the point-to-point sampling method of NOGA mapping, several research groups have developed fusion software for constructing hybrid images of cMRI and NOGA CARTO mapping [22–29]. These reports on a limited number of patients confirmed that there is good correlation between the two 3D images regarding the location and size of the infarction. However, the reports noted that NOGA mapping does not show good correlation with cMRI-LE in terms of the delineation of non-transmural areas. Moreover, the aim of these multimodality images was to find a focus for arrhythmogen substrates for ablation therapy to treat reentry tachycardias using unipolar and bipolar voltage electrocardiograms.

Here we focused on the accuracy of NOGA mapping to delineate transmural and non-transmural infarction by comparing it with cMRI-LE imaging. We investigated whether NOGA mapping is suitable for guiding intramyocardial drug or cell delivery using data from experimental myocardial infarction studies. We chose to use an animal model of closed chest reperfused MI. This is very similar to human primary percutaneous coronary intervention in acute MI, which simulates post-infarction left ventricular dysfunction.

We hypothesized that real-time, on-table 3D endocardial mapping using the NOGA system can accurately delineate the zone of decreased viability and non-transmural scars that is the target area for percutaneous intramyocardial therapy. Here we show that there is a significant correlation between the two images in terms of infarct size and the sizes of the transmural and non-transmural infarction, with high degree of overlap between endocardial mapping and cMRI-derived infarcted areas.

Materials and Methods

Experimental chronic left ventricular dysfunction post MI

Closed-chest reperfused acute MI was induced in 60 female farm pigs by percutaneous occlusion of the mid left anterior descending coronary artery. Sixty days later, the pigs underwent cMRI-LE images to confirm chronic myocardial infarction. Additional NOGA endocardial mapping was then performed

2 ± 1 days later, just before the animals were euthanized, aiming to search for correlations between the two images.

Briefly, all pigs were sedated with ketamine hydrochloride (12 mg/kg), xylazine (1 mg/kg), and atropine (0.04 mg/kg) intramuscularly. The pigs were intubated intratracheally and anesthetized with isoflurane (1.5–2.5 vol%), O₂ (1.6–1.8 vol%), and N₂O (0.5 vol%). O₂ saturation, blood pressure, and electrocardiography were monitored continuously. After an arteriotomy of the right femoral artery, a 6F introducer sheath (Terumo Medical Corporation, Somerset, NJ, USA) was inserted. Heparin (200 IU/kg) was administered followed by selective angiography of the left coronary artery tree. A balloon catheter (3.0 mm in diameter, 9 mm long; Maverick, Boston Scientific Corp, Natick, MA, USA) was advanced into the left anterior descending coronary artery (LAD). After the origin of the second major diagonal branch, the mid LAD was occluded by inflation of the balloon at 5 atmospheres for 90 minutes, followed by deflation of the balloon to allow opening of the infarct-related artery and reperfusion of the ischemia-affected myocardium. The pigs were then allowed to recover from the anesthesia.

This study was carried out in strict accordance with the recommendations in the Guide for the Care and Use of Laboratory Animals of the National Institutes of Health. The protocol was approved by the Experimental Animal Care and Use Committee at the Faculty of Animal Science of the University of Kaposvar (Hungary) (Permit Numbers: 246/002/SOM2006/11/11 and 246/002/SOM2006/08/11). All procedures were performed under general anesthesia, and all efforts were made to minimize the suffering of the animals.

NOGA electroanatomical mapping of the LV

The electromechanical maps of the pigs were obtained 62 ± 1 days after induction of acute MI. The principles and procedures of NOGA electroanatomical mapping have been described previously [7–10]. Briefly, the external reference patch, which contains a tip sensor, was taped onto the experimental animal's back below its heart. A 7 F introducer sheath was introduced into the left femoral artery, followed by administration of 5000 IU of unfractionated heparin. To begin the navigation process, a fully deflected NogaStar (Johnson & Johnson, Diamond Bar, CA) mapping catheter was introduced through the femoral sheath and was advanced inside the aorta under fluoroscopic guidance. Before entering the LV chamber, the mapping catheter was bent and then introduced through the aortic valve. As soon as the tail of the catheter was inside the LV, the catheter tip was straightened and orientated towards the apex. The first few endocardial points in different regions of the LV (apical point, outflow tract, and lateral and posterior points) were sampled to initiate a three-dimensional silhouette of the heart, which was then updated in real time with every new mapping point which facilitated further electromagnetic navigation with limited use of fluoroscopy.

At least four points were acquired in each of twelve myocardial segments. During the mapping process, simultaneous unipolar and bipolar electrocardiograms were recorded as well as the 3D location and orientation of the catheter tip of several sites within the LV cavity. The electrophysiological and mechanical data were integrated to create a color-coded 3D reconstruction of the LV chamber to facilitate assessment of the regional viability. The stability of the catheter-to-wall contact was evaluated at every location in real time, and only stable location points were accepted to create the 3D maps [9,10]. When constructing the NOGA maps, care was taken to correctly define the apex and the heart axis.

Using the movement of the catheter tip in the LV cavity, the end-diastolic, end-systolic volumes and global ejection fraction were calculated automatically. The average heart rate was calculated during the electroanatomical mapping procedure.

Evaluation of the NOGA maps

ImageJ for Windows (U.S. National Institutes of Health [NIH], Bethesda, Maryland, USA) was used to determine the relative size of the area of interest. The 3D unipolar (UPV) and bipolar (BiPV) voltages of each measuring point were displayed as two-dimensional polar maps (bull's eye format). The same discriminatory threshold values were used for all NOGA maps: <5 mV for non-viable infarcted area, 5–15 mV for infarct border zone and >15 mV for normal viability in unipolar maps and <0.8 mV for transmural, 0.8–1.9 mV for non-transmural infarction and >1.9 mV for normal myocardium in bipolar maps. These cut-off values are represented by the color-coding of the NOGA images and facilitate the identification of areas with reduced UPVs and BiPVs (Table 1, Fig. 1). As a next step, in order to validate the discriminatory threshold values for bipolar NOGA maps, we determined the correlation between MRI-based infarct area measurements and different discriminatory bipolar cut-off values. Specifically, we exported the raw images of the NOGA transmural data (i.e. the bipolar recordings) into the image processing pipeline of Matlab R2010 for Windows, converted the image RGB (red-green-blue) color values into voltage values, and cropped the image to the cMRI-LE infarct area. Using 100 threshold steps (from 0.5 to 1.5 mV), we iteratively exported the NOGA-based transmural areas to the cMRI transmural maps and determined the correlation coefficient between the two images using different thresholds (25, 30, 50, 60, and 75% transmural) (Fig. 2A).

In order to determine the BiPV cut-off that provides the best fit to the size of transmural and non-transmural cMRI-LE areas, we also tested 0.5–1.5 mV and 1.0–2.0 mV BiPV cut-offs (Fig. 3). The fibrous ring and cardiac valves, represented as red zones at the outer edge of the bull's eye NOGA maps, were excluded from analysis as they contained low UPVs and BiPVs that were indicative of non-contractile collagen structures [9,10].

The relative size of the infarct core, border areas, and normal myocardium was determined from the color-coded unipolar voltage polar map, and the sizes of the transmural and non-transmural infarction were delineated on the bipolar maps (Figs. 4 and 5). The demarcation and measurement of these areas on the NOGA maps was carried out by a researcher who was blinded to the results of the cMRI-LE.

cMRI-LE acquisitions

Cardiac magnetic resonance (cMRI) images were acquired on a 1.5 T Siemens Avanto Syngo B17 clinical scanner (Erlangen, Germany) with a phased-array coil and a vector ECG system. Functional (dynamic) images were acquired using a retrospective ECG-gated (HR: 80–100 beats/minute), steady-state free precession (SSFP - TRUFISP sequence) technique in short-axis and long-axis sections of the heart using 1.2-ms echo time (TE), 40-ms repetition time (TR), 25 phases, 50° flip angle, 360-mm field-of-view, 8-mm slice thickness, and a 256×256 image matrix. For quantitative measurement of infarct extent and transmural, delayed enhancement diastolic phase short-axis images were obtained after injection of 0.05 mmol/kg of contrast medium using an inversion recovery prepared gradient-echo sequence. LE images were obtained 10 minutes after gadolinium contrast agent injection.

Analysis and visualization of cMRI images

In all cases, care was taken to include the entire heart volume from the apex to the level of the great vessels, and the entire left ventricle was included in the MRI analysis. Analysis was consistently restricted to slices between the apex and the basis on which the left ventricle myocardium is seen in 360 degrees. Image analysis was performed using Segment for Windows software (version 1.9; Medviso AB, Lund, Sweden) [30]. The extent and transmural of the infarct was semi-automatically quantified on the 10-minute LE images using the “2SD” approach. During this procedure, hyperintense image pixels were tagged as infarcted if their signal intensity (SI) was greater than the mean value plus 2 standard deviations of the normal-appearing LV myocardium. Signal intensity was derived from the absolute value of the voxel intensity data, which were stored in the DICOM files from the cMRI-LE acquisitions.

The 3D infarct volume was determined both in absolute units and as a percentage of the total LV myocardium volume (Fig. 1). The entire LV was imaged by both NOGA and cMRI-LE in order to obtain an accurate volume measurement. The non-contractile mitral valve areas, which are clearly visible in both images, were excluded from the quantitative analysis of infarct size and transmural.

Polar plots were derived from the infarct segmentations using segmental transmural data. The corresponding bull's eye maps were processed to achieve the same apex, heart axis, and orientation as for NOGA maps.

For these visualizations, viability data from 8 apico-basal slices and 32 wall sectors per slice were interpolated and smoothed. The linear borders of 17 segments were overlaid on the images

Table 1. NOGA endocardial unipolar and bipolar map-derived cut-off values.

Cut-off value	Color on the NOGA map	Definition
Unipolar voltage map		
>15 mV	Blue, violet	Normal tissue
5–15 mV	Yellow, green	Border zone of infarction
<5 mV	Red	Area of myocardial infarction
Bipolar voltage map		
>1.9 mV	Blue, violet	Normal tissue
0.8–1.9 mV	Yellow, green	Non-transmural infarction
<0.8 mV	Red	Transmural infarction

doi:10.1371/journal.pone.0113245.t001

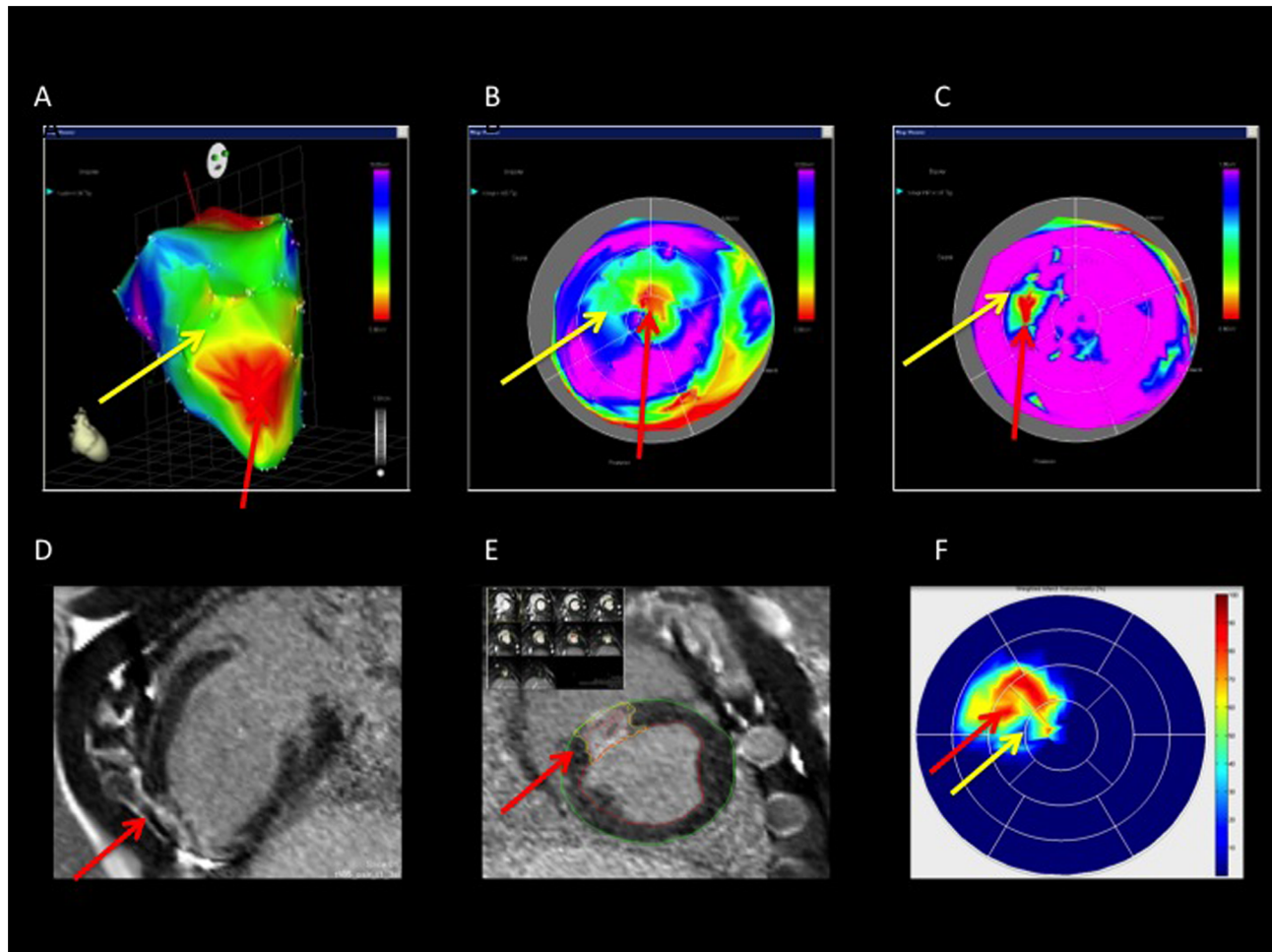


Figure 1. NOGA endocardial mapping and cardiac magnetic resonance imaging (cMRI) of a pig with chronic myocardial ischemia. A. 3D NOGA mapping showing anterior, anteroseptal, and apical myocardial infarction. Red indicates the infarct core (red arrow), the surrounding green-yellow area shows the border zone of infarction (yellow arrow). B. The corresponding unipolar voltage polar map. The color-coding is the same as in A. C. The bipolar voltage polar map of the same pig. Red indicates the transmural infarction (red arrow); yellow-green indicates the non-transmural infarction (yellow arrow), and blue-pink indicates normal myocardium. D. cMRI with late enhancement reveals the myocardial scar (red arrow). Long axis image. E. cMRI late enhancement short axis images with myocardial infarction (red arrow). Quantitative size of infarction was assessed by dividing of the myocardium to 8 slices from heart basis to apex (left upper corner). F. A cMRI transmural map shows the transmural infarction (red arrow) with a surrounding area of non-transmural infarction (yellow arrow). doi:10.1371/journal.pone.0113245.g001

graphically to help interpret the images using “classical” segmental nomenclature, while the interpolated data originated from 32 sections per slice. The endo- and epicardial borders were segmented, and a segmental model was fitted on the left ventricle model (32 sections per slice). Using the standard transmural analysis feature of the Segment software (Medviso Inc., Lund, Sweden), the midline was calculated for each section of the LV myocardium. The transmural of the infarct is given as the radial projection of the segmented scar volume on the midline, summed for each section.

By applying two-dimensional planimetry to the polar plots, we performed two distinct measurements of the transmural of the infarct. The extents of the transmural or non-transmural infarct and normal areas were defined as the percentage of sectors in which the SI was >75% (infarct core), 51–75% (border zone of infarction), 25–50% (non-transmural infarction), or <25% (normal) [22]. Alternatively, SI >60% was defined as transmural infarct, 31–60% as non-transmural infarct, and <30% as a normal area [21]. To calculate the areas, we used the raw transmural

data from 32 sections per slice, as noted above. All MRI area measurements are reported as the percentage of segments in the threshold range divided by the total number of segments.

Dynamic MR images were analyzed for myocardial wall movement and functional parameters. We carried out semi-automatic segmentation of the LV endocardial and epicardial borders while the end-diastolic volume (EDV), end-systolic volume (ESV), global LV ejection fraction (EF), and cardiac output (CO) were calculated automatically on short-axis images.

Overlap ratio

The overlap ratio between the cMRI and NOGA bipolar transmural maps was calculated as follows [28] (Fig. 6):

$$\frac{(\text{NOGA bipolar map overlap area} + \text{cMRI transmural map overlap area})}{(\text{NOGA bipolar low voltage area} + \text{cMRI transmural area})}$$

For the overlap ratio of the transmural, non-transmural and the combined transmural and non-transmural (not normal) areas the following cut-off values were used:

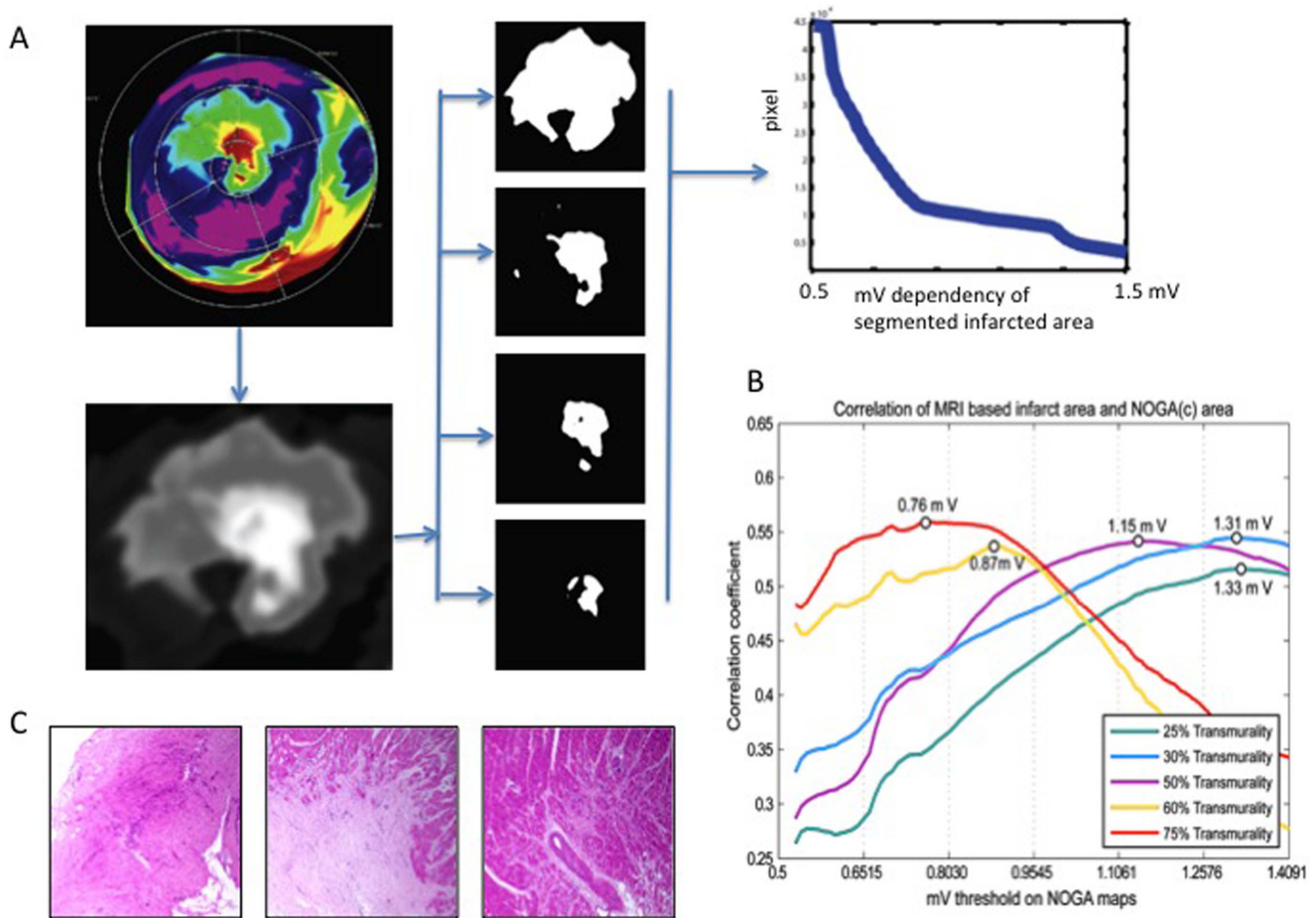


Figure 2. Magnet resonance imaging- (MRI-) derived NOGA bipolar threshold values for infarct transmural. A. Iterative thresholding of voltage maps (left panel). The original NOGA maps were cropped to infarct areas, converted to a mV scale, then iteratively thresholded using 100 steps from 0.5 to 1.5 mV. The middle panel shows examples of the iterative thresholding process. The right panel shows the association between the area of infarction and the applied mV threshold. B. Voltage-threshold dependence of the correlation between NOGA maps and areas on an MRI. The maximum correlation coefficient is shown for each line plot. C. Histological correlations of transmural (left) and non-transmural (middle) infarctions and normal heart tissue (right). Samples were taken from areas with bipolar voltage values <0.8 mV, between 0.8 – 1.9 mV, and >1.9 mV with corresponding cMRI-LE transmural values of $>75\%$, 50% , and $<25\%$, respectively. Magnification: $2\times$. doi:10.1371/journal.pone.0113245.g002

- Transmurality overlap ratio: between a NOGA bipolar map area with BipV <0.8 mV and a cMRI transmural area with SI $>75\%$;
- Non-transmural areas overlap ratio: between a NOGA bipolar map area with BipV 0.8 – 1.9 mV and a cMRI transmural area with SI 25 – 75% ;
- Combined transmural and non-transmural (not normal) area overlap ratio: between a NOGA bipolar map area with BipV <1.9 mV and a cMRI transmural area with SI $>25\%$ (Figs. 4 and 5).

Overlap $>60\%$ was considered good accuracy [28], and 50 – 60% overlap was considered moderate accuracy (arbitrary value).

Histology

Myocardial samples were collected from transmural and non-transmural infarctions and from normal heart tissue. These were areas with bipolar voltage values <0.8 mV, from 0.8 – 1.9 mV, and >1.9 mV with corresponding cMRI-LE transmural values of $>75\%$, 50% , and $<25\%$, respectively. The samples were stored in 4.5% buffered formalin for at least 24 h and embedded in

paraffin. Sections were cut into 4 – to 6 - μM thick slices and stained with hematoxylin-eosin.

Statistical analysis

Continuous variables are presented as mean values \pm standard deviation. The correlation between NOGA- and cMRI-derived parameters (infarct size, transmural and non-transmural infarct size) was calculated by linear regression analysis using Pearson Product Moment Correlation and Bland-Altman plots. Linear regression and Bland-Altman analysis was performed using Matlab R2010 software for Windows. During the iterative fitting of the linear function, a “least absolute residual” robust regression approach was used [31]. For interpretation of the correlations between 2 images the standardized nomenclature was used: if the correlation coefficient is greater than 0.5 is large, 0.5 – 0.3 is moderate, and 0.3 – 0.1 is a small correlation [32].

In order to choose the correct BiPV cut-off values for determining the transmural and non-transmural scars, all UPVs were also correlated with the corresponding BiPVs using linear regression analysis. Using a 5 mV UPV value as the cut-off for viability/non-viability, receiver operator curve (ROC) analysis was

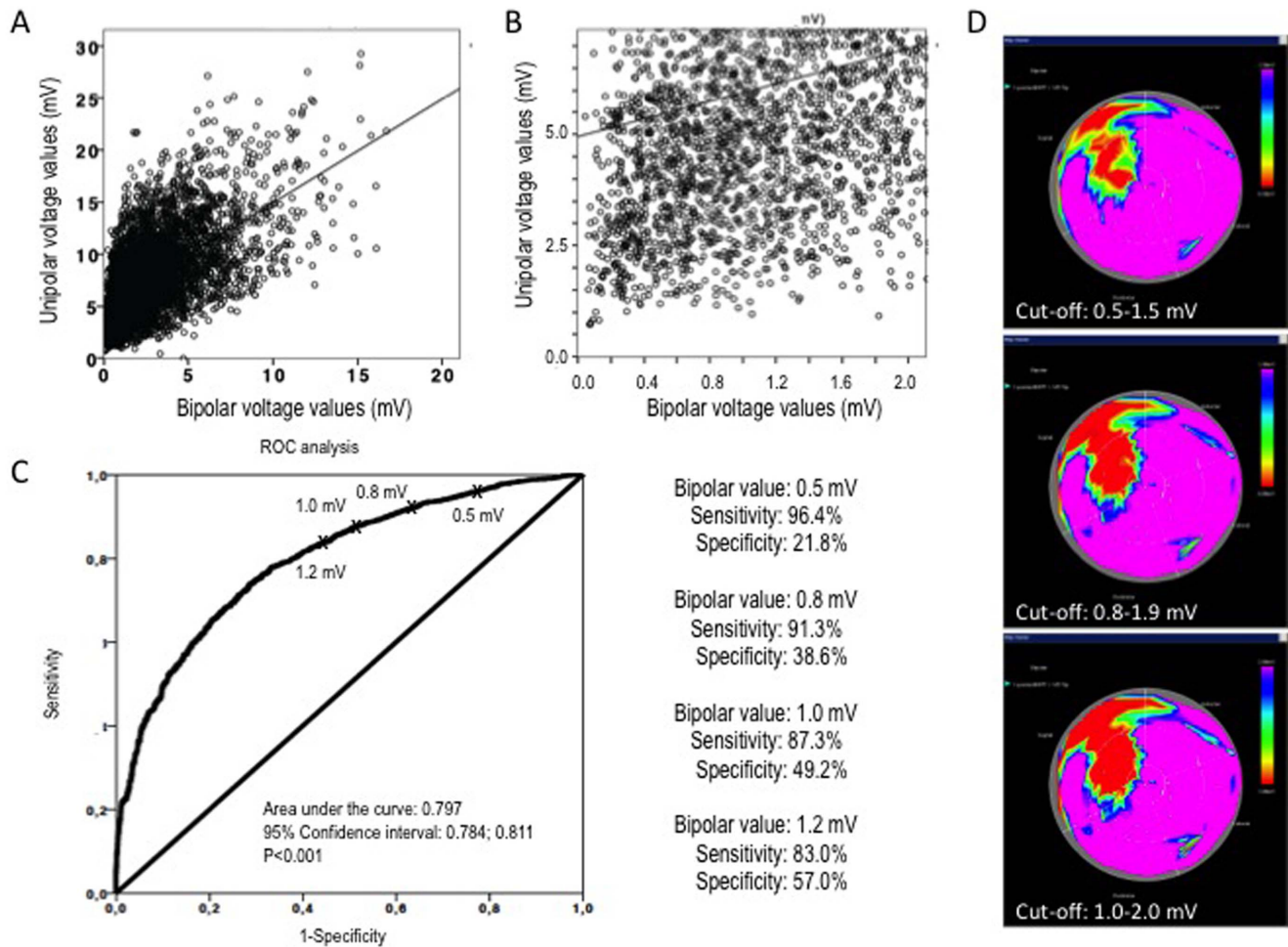


Figure 3. Determination of the bipolar voltage (BiPV) cut-off value for calculating the transmural and non-transmural infarct size using unipolar voltage values. A. Linear correlation between unipolar and bipolar voltage values. B. Part of the correlation showing the non-viable range defined as unipolar voltage values <5 mV. C. Receiver operator characteristics curve for determination of different bipolar voltage cut-off values. D. Display of bipolar maps using different cut-offs. doi:10.1371/journal.pone.0113245.g003

performed, and the sensitivity, specificity of different BiPV values, and the area under the curve, with 95% confidence intervals, were calculated.

For all statistical analyses, a p-value <0.05 was considered statistically significant.

Results

There were no complications during the NOGA and cMRI-LE procedures that required additional medication or cardiopulmonary resuscitation.

Correlation of NOGA threshold values with MRI-based transmuralities

Depending on the threshold values applied to the NOGA bipolar voltage maps, the correlations between the different cut-offs of the two images were $r=0.27-0.57$. The 75% MRI transmuralities areas showed the best correlation with the NOGA-based areas using a cut-off of 0.76 mV, while the 60% transmuralities areas correlated best with NOGA maps using a 0.87 mV threshold. The validation experiment resulted in a cut-off value of 1.3 mV for 25% transmuralities. In order to exclude non-

transmural ischemia, we used the usual value of 1.9 mV for normal, non-infarcted areas (Figure 2B). Notably, these cut-offs correlated well with the histological findings (Fig. 2C), confirming the proprietary diagnosis of transmural and non-transmural areas.

cMRI and NOGA mapping results

The cMRI-LE and NOGA endocardial mapping results are summarized in Tables 2 and 3. NOGA mapping and cMRI-LE showed similar results for LV volumes and global EF. Heart rates were slightly higher during the NOGA procedure, probably due to the longer procedure time.

The NOGA endocardial maps contained a mean of 202 ± 31 (range: 152–295) mapping points per animal, with a mapping point distribution of 16.8 ± 5.5 points per segment of the 12-segment view. The mapping points were connected automatically if the distance between points was less than 15 mm. The mean time for the NOGA procedure was 35 ± 9 min.

The BiPV values correlated significantly with the UPV values (Fig. 3). ROC analysis showed that a BiPV value of 0.8 mV as the non-transmural cut-off value had a sensitivity >90% and low but acceptable specificity. Display of the bipolar maps with different cut-offs revealed small differences between the images, with a

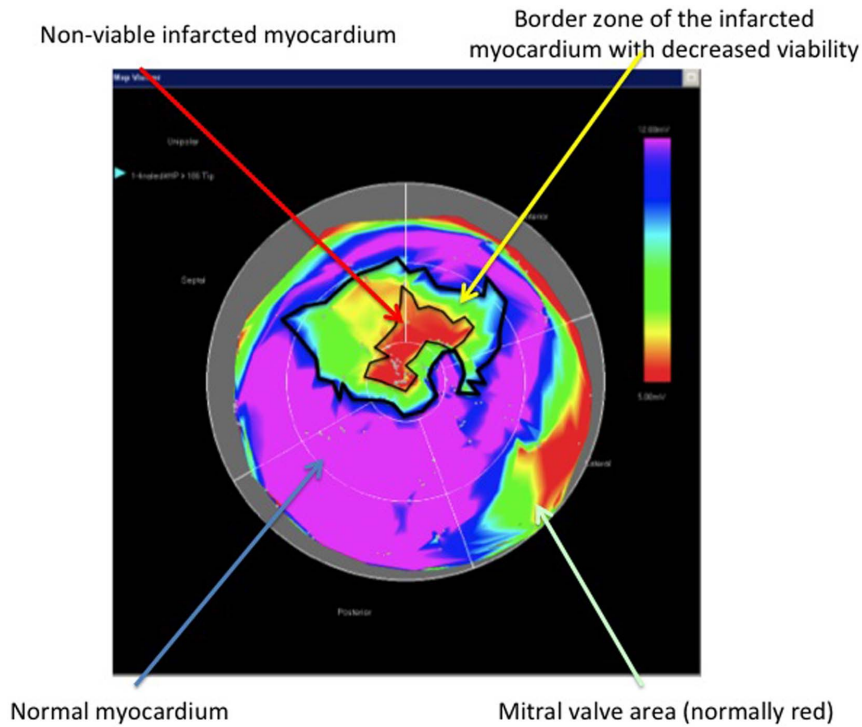


Figure 4. Schematic illustration of the planimetric calculation of the size of the infarct core and the size of the border zone of the infarction with decreased viability in the NOGA endocardial mapping. Red indicates the infarct core, and green-yellow indicates the surrounding area that has decreased viability.
doi:10.1371/journal.pone.0113245.g004

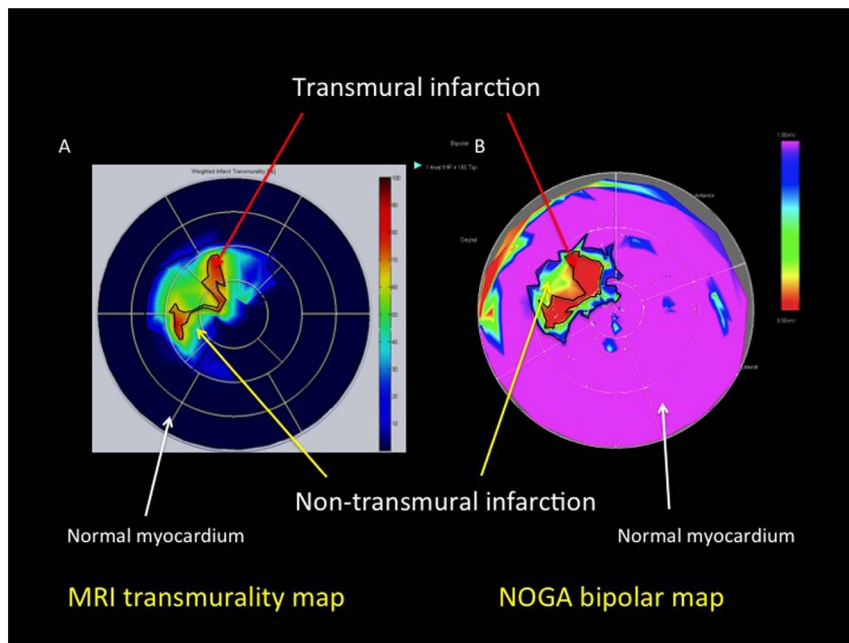


Figure 5. Schematic illustration of the planimetric calculation of the transmural and non-transmural infarct sizes as shown in polar maps from cardiac magnetic resonance imaging (cMRI) and NOGA endocardial mapping. A. Planimetric calculations of the sizes of the transmural and non-transmural infarction by cMRI. B. Planimetric calculations of the sizes of the transmural and non-transmural infarction in a NOGA bipolar voltage map.
doi:10.1371/journal.pone.0113245.g005

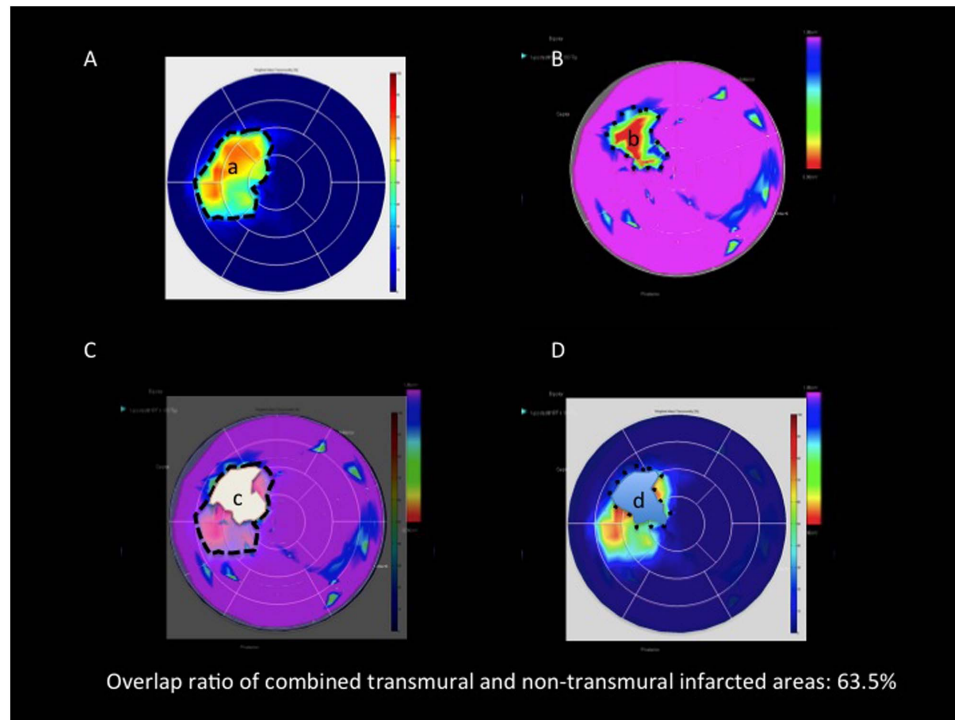


Figure 6. Calculation of the overlapping ratio of the transmural plus the non-transmural infarction by cardiac magnetic resonance imaging (cMRI) and NOGA endocardial mapping. A. cMRI transmural polarity polar map. B. NOGA bipolar polar map. C and D. Overlap of the cMRI and NOGA polar maps. a: The size of the transmural and non-transmural infarction by cMRI; b: the size of transmural and non-transmural infarction by NOGA bipolar mapping; c: overlap of the NOGA bipolar infarct shape on a cMRI polar map; d: overlap of the cMRI infarct shape on a NOGA bipolar map. The overlapping ratio was calculated as follows: (c+d)/(a+b).

doi:10.1371/journal.pone.0113245.g006

transmural infarct size of $12.5 \pm 8.7\%$ using a 0.5-mV cut-off value, $14.1 \pm 6.2\%$ using a 0.8-mV cut-off value, and $16.8 \pm 5.3\%$ using a 1-mV BiPV cut-off value, with no statistically significant differences between the 3 area measurements. Based on the best overlap ratio between the two images, a BiPV cut-off of 0.8–1.9 mV was used for further analysis.

The unipolar voltage map-derived scar size (UPV < 5 mV) showed a moderate association with the transmural scar size as determined by bipolar maps (BiPV < 0.8 mV) ($r = 0.385$, $p = 0.002$). There was better concordance between the border zone of infarction (UPV 5–15 mV) and non-transmural scars (BiPV 0.8–1.9 mV) ($r = 0.457$, $p < 0.001$). The total size of the

ischemic area showed good correlation between the two maps ($r = 0.575$, $p < 0.001$).

Correlation of infarct size as determined by cMRI-LE and NOGA mapping

There was a significant correlation ($r = 0.504$, $p < 0.001$) between the infarct size as determined using the NOGA unipolar voltage polar map and the size determined by cMRI-LE. The Bland-Altman plot showed that NOGA mapping resulted in a systematically higher infarct size compared to cMRI-LE, with a mean difference between the two images of $2.82 \pm 7.43\%$ in the LV surface (Fig. 7).

Table 2. Endocardial NOGA mapping results.

NOGA electromechanical mapping	Value (mean \pm SD) (n = 60)
End-diastolic volume	108 \pm 12 mL
End-systolic volume	67.1 \pm 9.6 mL
Stroke volume	41.3 \pm 11.6 mL
Left ventricular ejection fraction	38.7 \pm 7.6%
Heart rate	110 \pm 7 bpm
Relative size of the infarct core (area of unipolar voltage < 5 mV)	19.5 \pm 8.1%
Size of the area of border zone of the infarction (area of unipolar voltage 5–10 mV)	20.4 \pm 9.7%
Size of the transmural infarction (area of bipolar voltage < 0.8 mV)	14.1 \pm 6.2%
Size of the non-transmural infarction (area of bipolar voltage 0.8–1.9 mV)	11.6 \pm 5.6%

doi:10.1371/journal.pone.0113245.t002

Table 3. Results of cardiac magnetic resonance (cMRI) with late enhancement.

cMRI	Value (mean \pm SD) (n = 60)
End-diastolic volume	106 \pm 22 mL
End-systolic volume	67.8 \pm 22 mL
Stroke volume	38.2 \pm 8.4 mL
Left ventricular ejection fraction	37.6 \pm 8.9%
Heart rate	102 \pm 11 bpm
Cardiac output	4.2 \pm 1.1 L/min
Cardiac index	3.7 \pm 0.9 L/min/m ²
Left ventricular myocardial mass	108 \pm 15 g
Left ventricular myocardial volume	103 \pm 14 mL
Relative infarct size of left ventricular myocardial mass	16.9 \pm 6.3%
Volume of myocardial infarction	15.7 \pm 6.5 mL
0%–30%–60%–100% SI for transmural	
Size of transmural infarction if SI > 60%	10.4 \pm 5.1%
Size of non-transmural infarction if SI = 31–60%	8.4 \pm 3.9%
Size of non-infarcted tissue if SI < 30%	81.2 \pm 6.7%
0%–25%–50%–75%–100% SI for transmural	
Size of transmural infarction if SI > 75%	6.4 \pm 5.6%
Size of border zone of transmural infarction if SI = 51–75%	7.5 \pm 4.3%
Size of non-transmural infarction if SI = 25–50%	6.7 \pm 2.9%
Size of non-infarcted tissue if SI < 25%	79.4 \pm 7.6%

SI: signal intensity.

doi:10.1371/journal.pone.0113245.t003

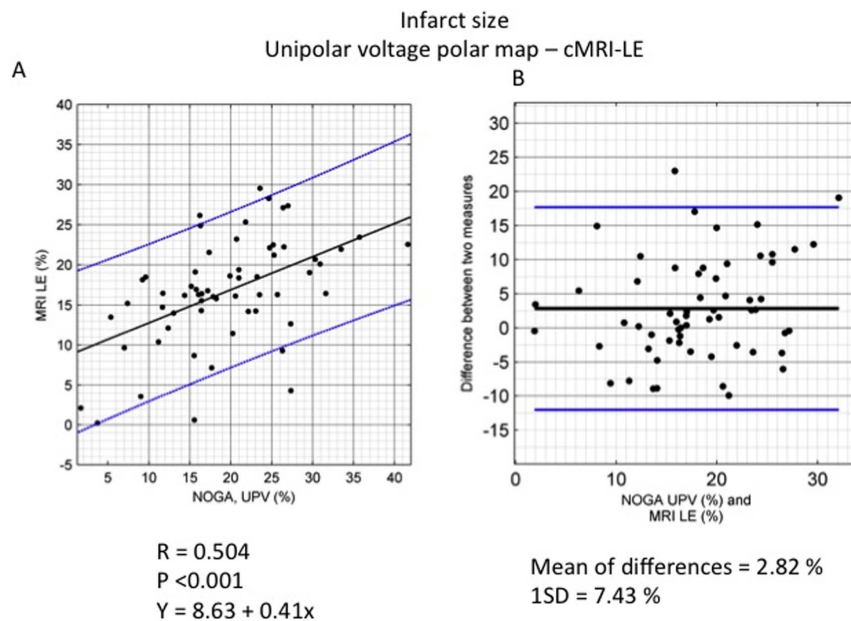


Figure 7. Correlation between NOGA endocardial mapping and cardiac magnetic resonance imaging (cMRI) and statistical analysis of the determination of infarct size. A. Regression equation between the size of the infarct core as determined on a unipolar voltage map (UPV) and as determined using late enhancement cMRI. B. Bland-Altman plot of the size of the infarct core as determined on a unipolar voltage map and the size as determined using late enhancement cMRI. Mean (black line) \pm 2SD (blue line).
doi:10.1371/journal.pone.0113245.g007

Correlation of transmural infarct size as determined by cMRI and NOGA mapping

Using $SI > 75\%$ and NOGA BipV < 0.8 mV, the correlation between the two images was $r = 0.727$ ($p < 0.001$) for the size of the transmural infarction. NOGA bipolar mapping resulted in a larger transmural infarction size than did cMRI-LE, with a mean difference of $6.81 \pm 4.39\%$ in the LV surface.

Using cut-offs for infarct transmurality of $SI > 60\%$ and NOGA BipV < 0.8 mV, the correlation was slightly lower ($r = 0.576$, $p < 0.001$), with a mean difference between the two images of $2.14 \pm 5.62\%$ of LV surface.

Correlation between cMRI and NOGA mapping regarding non-transmural infarct size

Using $SI = 51\text{--}75\%$ and NOGA BipV $0.8\text{--}1.9$ mV to define non-transmural infarction, the correlation between the two images was $r = 0.555$ ($p < 0.001$). NOGA bipolar mapping resulted in a smaller area of non-transmural infarction, with a mean difference of $3.04 \pm 5.92\%$ between the two images (Fig. 8).

Using $SI = 31\text{--}60\%$ and NOGA BipV $0.8\text{--}1.9$ mV as cut-offs for non-transmural infarction, the correlation was slightly higher

($r = 0.657$, $p < 0.001$), with a mean difference between the two images of $3.23 \pm 4.56\%$ of LV surface.

Overlap ratio

The overlap ratio was $81.6 \pm 11.1\%$ and $70.6 \pm 18.5\%$ for delineation of the transmural and non-transmural infarction size on the cMRI and NOGA images, respectively. None of the images showed an overlapping accuracy below 60% regarding transmural infarction. Regarding non-transmurality, two of the 60 animals (3.3%) showed an overlapping ratio between 50% and 60%, which was considered moderate agreement between the two imaging methods.

The overlap ratio of the combined transmural and non-transmural infarction was $70.2 \pm 12.2\%$.

Discussion

Our results indicate that NOGA electroanatomical mapping is accurate enough to guide targeted intramyocardial therapy if both unipolar and bipolar maps are used. The results of NOGA were comparable to those of cMRI-LE, regarding the extent of the transmural and non-transmural scars and viable and reduced viability myocardial areas.

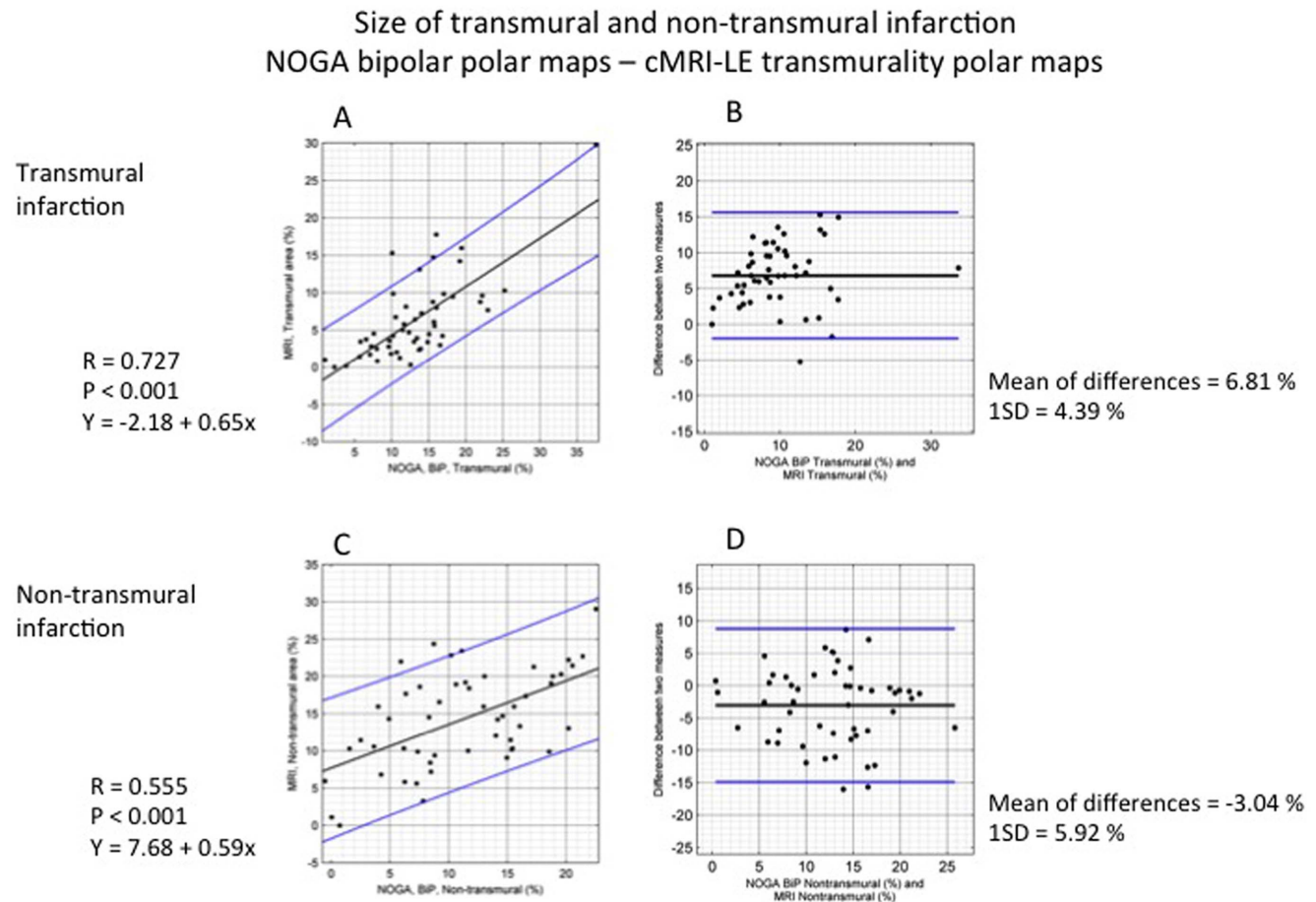


Figure 8. Correlation between NOGA endocardial mapping and cardiac magnetic resonance imaging (cMRI) and statistical analysis of the determinations of transmural and non-transmural infarction. A. Regression equation between the size of the transmural infarction as determined on a bipolar voltage map and the size as determined using cMRI. B. Bland-Altman plot of the size of the transmural infarction as determined on a bipolar voltage map and the size as determined using cMRI. Mean (black line) $\pm 2SD$ (blue line). C. Regression equation between the size of the non-transmural infarction as determined on a bipolar voltage map and the size as determined using cMRI. D. Bland-Altman plot of the size of the non-transmural infarction as determined on a bipolar voltage map and the size as determined using cMRI. Mean (black line) $\pm 2SD$ (blue line). doi:10.1371/journal.pone.0113245.g008

The main difference between the two 3D images is that different sampling methods are used to construct them. The NOGA 3D LV shape is constructed by point-to-point measurements, which is in contrast with the other 3D methods, such as cMRI-LE, which have a spatial resolution of 1.4 mm per voxel. For map construction, a 15-mm point-to-point distance was used by endocardial mapping, while an in-plane resolution of 1–2 mm with an 8-mm slice thickness was utilized for cMRI-LE analysis. Accordingly, the accuracy of the NOGA map depends mainly on the number of gathered and measured points and on the quality of the acquired points used to construct the 3D map. Difficulties in reaching some regions with the mapping catheter due to LV cavity structures such as the papillary muscles or the occurrence of ventricular arrhythmias due to touching vulnerable ischemic areas might lead to insufficient sampling, resulting in incomplete mapping. Nevertheless, unipolar voltage mapping overestimated the infarct size by just 2.82% of the entire LV endocardial surface, and bipolar mapping overestimated the transmural scar by just 6.82% of the LV. These estimates are acceptable for performing intramyocardial procedures safely and accurately. The overestimation of the infarct size and transmural scar as compared to cMRI-LE might result from the quantitative comparison of 2D NOGA polar maps and 3D cMRI-LE and 2D transmural cMRI-LE images. According to our results, both the unipolar and bipolar voltage maps showed wider zones of interest than on cMRI, which may raise the risk of injecting reparative substances into normal myocardium. The intramyocardial injections are oriented into the non-transmural infarct or into areas with decreased viability. Different cut-offs are suggested for viability and transmural thresholds in the literature; there are no universally agreed-upon definitions for these terms. Of course, the operators should try to make sure that the intramyocardial injections are made into the correct area, but an injection may be made into the “normal” myocardium if stronger cut-off criteria for non-normal territory are used. However, regenerative cells or other material delivered into the lane neighboring the non-transmural infarction have a good chance of being retained, being functional, and migrating or penetrating into the ischemic area, so a wider zone might result in more effective and safe treatment.

The sizes of the unipolar voltage scar and border zone differed from the sizes of transmural and non-transmural infarction as determined on the bipolar maps. Although the total size of the unhealthy areas on the unipolar and bipolar polar maps showed good correlation, the size of the infarction and border area determined on the unipolar maps was systematically larger than the size of the transmural and non-transmural regions on the bipolar maps. This is not surprising, because an infarct area contains heterogeneously viable myocytes that can be apoptotic or hibernating. Accordingly, the infarct core and the border area (i.e. the extent of infarction) do not necessarily overlap the transmural and non-transmural infarction (i.e. the infarction severity) because the infarct core may include transmural and non-transmural necrotic areas.

The unipolar voltage values represent a summation of the action potentials of the surrounding endocardial surface areas, while the bipolar voltage values represent the amplified difference between the tip of the unipolar electrode and the additional proximal electrode placed within the catheter. Accordingly, a non-transmural infarction with severe endocardial (but not epicardial) necrosis may appear to be an infarct core in the unipolar map. This might explain the differences between the unipolar and bipolar NOGA maps, and between the NOGA maps and other 3D images that measure infarct size. Nevertheless, using both (uni- and bipolar) maps of the NOGA images, information about both

the extent and the severity of infarction are available real-time, on-table during a procedure, in contrast to off-line images such as cMRI-LE or myocardial single photon emission computed tomography.

Additionally, to set the correct and right cut-off values of the NOGA maps is of great importance. Several authors used several different cut-off values for definition of viability using the unipolar voltage maps, while the usage of bipolar maps is less common, probably due to the small range of not normal values (0–1.9 mV of interest) suggesting less precise differentiations. We have measured the transmural and non-transmural scars on the cMRI-LE image using two different SI cut-offs, because a SI between 25% and 50% suggests a false positive non-transmural infarction. When the cMRI transmural threshold is lowered to 60% from 75% and to 31–60% from 51–75%, the size of the transmural and non-transmural infarct areas increase, and the correlations are slightly lower and higher, respectively. The SI of 30% and 60% for cut-off of non-transmural and transmural scars gave a better correlation with slight overestimation of the non-transmural scar by 3.23% of the LV. Since the endocardial injections should target non-transmural infarct areas, higher correlation between the two images in that region is desirable.

Comparison of our results with literature data

The need to localize the arrhythmogenic focus for ablation during catheter-based electrophysiological procedure prompted several research groups to develop hybrid software that analyzes the 3D images of both NOGA maps and cMRI-LE. Fusion of cMRI with electroanatomical mapping of the LV proved to be successful with a registration error of 3.8 ± 0.6 mm [22], with visual mismatches between the NOGA scars and LE in cMRI, particularly in patients with inferior infarction [22]. To enhance the accuracy of the electroanatomical mapping relative to cMRI-LE for the determination of myocardial scars with a presumed arrhythmogenic focus, different cut-off values were tested: 1.5 mV for non-transmural scars and 0.5 mV for dense scars [22]; 1.0 mV [28], 1.3 mV [23], 1.54 mV [24], 1.55 mV [26], and 1.9 mV [27] for bipolar maps; and 5.8 mV [23], 6.52 mV [24], 6.9 mV [18], 6.78 mV [26], 6.7 mV [27], and 5.1 mV [28] for unipolar maps. This reflects the uncertainty of finding the arrhythmogenic focus with electroanatomical mapping alone and emphasizes the visual mismatch between the two images in certain cases. In contrast with these studies, the sample size in our animal study was much larger ($n = 60$), but we did not use fusion software. Instead, we compared the 2D maps of the NOGA images with the 3D LE and 2D transmural map of the cMRI. Nevertheless, we did not search for a single focus but rather for an area with reduced viability.

Limitations

We did not use local linear shortening maps of the NOGA for delineating of the hibernating myocardium characterized by preserved viability and decreased segmental wall motion [12], because of the lower accuracy of the local linear shortening map and higher discordance with cMRI [9] regarding the segmental wall motion abnormalities. We overlaid the two images in order to determine the overlapping accuracies, while other research groups used 3D fusion software. Accordingly, our method has several shortcomings in the technique used. The study reports comparisons of 2D transmural cMRIs and NOGA bipolar maps as well as comparisons of the 2D projection of the NOGA-derived infarct size and the 3D cMRI-LE-derived infarct size. However, both imaging modalities for quantitatively determining infarct size use

standardized image processing functions of the software and are widely used.

We are aware that there are ongoing efforts to fuse 3D NOGA endocardial maps and cardiac MRIs to determine the similarities of infarct location and extent. Although numerous percutaneous intramyocardial therapy studies are currently underway with the aim of determining the optimal injection location, currently there is no commercially available 3D MRI-NOGA fusion software. The comparisons of cMRI and NOGA polar maps published previously lack some of the refinements we used, such as comparison of the transmural map with the bipolar map and calculation of the overlapping ratio.

Unfortunately, we could not perform 3D volumetric co-registration of the compared modalities, as currently we do not have an image-processing tool with which to conduct such a comparison. The spatial correspondence was ensured by (1) similar selection of the basal and apical slice positions and (2) similar orientation of the bull's eye maps. The definition of sector orientation was based on manual selection of the right ventricular insertion point (sector 0) on the most basal MRI slice of the left ventricular myocardium. A real value of the fusion of the off-line cMRI-LE and on-table NOGA endocardial mapping would be the real-time display of the actual catheter position and location of the intramyocardial therapy on the reconstructed hybrid (cMRI and NOGA) image; which software is currently not available.

We have included the NOGA-derived volumetric measurements. The similarities between the NOGA-derived and cMRI-derived end-diastolic and end-systolic volume and calculated stroke volume and ejection fraction (Tables 2 and 3) ensure the acquisition of the entire LV map of the NOGA procedure and also ensure that the two images are comparable.

The use of 2SD method of cMRI-LE might overestimate the infarct size, as compared with the 5SD or "full width at half maximum" (FWHM) method. In our experience, it has not been the case that the 5SD method better reflects the infarct size compared to the 2SD approach, and there are data in the literature that show a higher correlation coefficient for the 2SD approach than the 5SD approach [33]. The FWHM method might correlate better with post-mortem measurements, but this

approach has not yet been implemented into the software we used for our data analysis. Based on the different sampling modes and standardized segmentation of both MRI (17 segments divided into 6 basal, 6 mid and 5 apical segments) and NOGA (9 segments divided into 4 basal, 4 mid and 1 apex segments), direct comparison of segmental mean values to search for a mathematical cut-off for unipolar and bipolar values based on MRI cut-off values would require extensive digital processing and adaptation of both images. However, we correlated the unipolar and bipolar voltage values and calculated different bipolar voltage cut-offs using ROC analysis. Additionally, we have determined the optimal bipolar cut-offs using iterative thresholding and calculated the transmural and non-transmural infarct areas using 3 cut-offs and compared these results with those of the cMRI-LE data. However, we did not search unipolar voltage threshold values based on cMRI-LE images because voltage maps correspond to myocardial viability and cMRI is not the first-choice imaging method for viability assessment. Extensive research has been performed to establish cut-offs for viable, non-viable, and hibernating myocardium using imaging technologies such as myocardial scintigraphy and positron emission tomography [9]. We used these literature-based cut-off values to calculate infarct size.

Conclusions

Our results demonstrate the usefulness of unipolar and bipolar maps generated using real-time electroanatomical mapping for targeted intramyocardial regenerative therapy. NOGA mapping showed good concordance with the off-line gold standard, cMRI-LE imaging. NOGA mapping may be useful in patients with contraindications for cMRI who require targeted intramyocardial regenerative therapy.

Author Contributions

Conceived and designed the experiments: NP AJ ME SH MG. Performed the experiments: NP AJ ME SH MG. Analyzed the data: NP AJ ME GS PW MZ HJA GM MG. Contributed reagents/materials/analysis tools: AJ PW GS MZ. Wrote the paper: NP MG.

References

- Freyman T, Polin G, Osman H, Crary J, Lu M, et al. (2006) A quantitative, randomized study evaluating three methods of mesenchymal stem cell delivery following myocardial infarction. *Eur Heart J* 27: 1114–22.
- Perin EC, Silva GV, Assad JAR, Vela D, Buja LM, et al. (2008) Comparison of intracoronary and transendocardial delivery of allogeneic mesenchymal cells in a canine model of acute myocardial infarction. *J Mol Cell Cardiol* 44: 486–495.
- Dib N, Khawaja H, Varner S, McCarthy M, Campbell A (2011) Cell therapy for cardiovascular disease: a comparison of methods of delivery. *J Cardiovasc Transl Res* 4: 177–81.
- Vrtovec B, Poglajen G, Lezaic L, Sever M, Socan A, et al. (2013) Comparison of transendocardial and intracoronary CD34+ cell transplantation in patients with nonischemic dilated cardiomyopathy. *Circulation* 128(11 Suppl 1): S42–9.
- Constantine G, Shan K, Flamm SD, Sivananthan MU (2004) Role of MRI in clinical cardiology. *Lancet* 363: 2162–71.
- Poon M, Fuster V, Fayad Z (2002) Cardiac magnetic resonance imaging: a "one-stop-shop" evaluation of myocardial dysfunction. *Curr Opin Cardiol* 17: 663–70.
- Ben-Haim SA, Osadchy D, Schuster I, Gepstein L, Hayam G, et al. (1996) Nonfluoroscopic, in vivo navigation and mapping technology. *Nat Med* 2: 1393–5.
- Gepstein L, Hayam G, Shpun S, Ben-Haim SA (1997) Hemodynamic evaluation of the heart with a nonfluoroscopic electromechanical mapping technique. *Circulation* 96: 3672–80.
- Gyöngyösi M, Dib N (2011) Diagnostic and prognostic value of 3D NOGA mapping in ischemic heart disease. *Nat Rev Cardiol* 8: 393–404.
- Psaltis PJ, Worthley SG (2009) Endoventricular electromechanical mapping—the diagnostic and therapeutic utility of the NOGA XP Cardiac Navigation System. *J Cardiovasc Transl Res* 2: 48–62.
- Kornowski R, Hong MK, Leon MB (1998) Comparison between left ventricular electromechanical mapping and radionuclide perfusion imaging for detection of myocardial viability. *Circulation* 98: 1837–41.
- Gyöngyösi M, Khorsand A, Sochor H, Sperker W, Strehblow C, et al. (2005) Characterization of hibernating myocardium with NOGA electroanatomic endocardial mapping. *Am J Cardiol* 95: 722–8.
- Gyöngyösi M, Sochor H, Khorsand A, Gepstein L, Glogar D (2001) Online myocardial viability assessment in the catheterization laboratory via NOGA electroanatomic mapping: quantitative comparison with thallium-201 uptake. *Circulation* 104: 1005–11.
- Callans DJ, Ren JF, Michele J, Marchlinski FE, Dillon SM (1999) Electroanatomic left ventricular mapping in the porcine model of healed anterior myocardial infarction. Correlation with intracardiac echocardiography and pathological analysis. *Circulation* 100: 1744–50.
- Fuchs S, Hendel RC, Baim DS, Moses JW, Pierre A, et al. (2001) Comparison of endocardial electromechanical mapping with radionuclide perfusion imaging to assess myocardial viability and severity of myocardial ischemia in angina pectoris. *Am J Cardiol* 87: 874–80.
- Keck A, Hertting K, Schwartz Y, Kitzing R, Weber M, et al. (2002) Electromechanical mapping for determination of myocardial contractility and viability. A comparison with echocardiography, myocardial single-photon emission computed tomography, and positron emission tomography. *J Am Coll Cardiol* 40: 1067–74.
- Sheehan FH, Bolson EL, McDonald JA, Reisman M, Koch KC, et al. (2002) Method for three-dimensional data registration from disparate imaging modalities in the NOGA Myocardial Viability Trial. *IEEE Trans Med Imaging* 21: 1264–70.
- Perin EC, Silva GV, Sarmento-Leite R, Sousa AL, Howell M, et al. (2002) Assessing myocardial viability and infarct transmural extent with left ventricular

- electromechanical mapping in patients with stable coronary artery disease: validation by delayed-enhancement magnetic resonance imaging. *Circulation* 106: 957–61.
19. Wiggers H, Botker HE, Søgaard P, Kallot A, Hermansen F, et al. (2003) Electromechanical mapping versus positron emission tomography and single photon emission computed tomography for the detection of myocardial viability in patients with ischemic cardiomyopathy. *J Am Coll Cardiol* 41: 843–8.
 20. Graf S, Gyöngyösi M, Khorsand A, Nekolla SG, Pirich C, et al. (2004) Electromechanical properties of the perfusion/metabolism mismatch: comparison of nonfluoroscopic electroanatomic mapping with ¹⁸F-FDG PET imaging. *J Nucl Med* 45: 1611–8.
 21. Wolf T, Gepstein L, Dror U, Hayam G, Shofti R, et al. (2001) Detailed endocardial mapping accurately predicts the transmural extent of myocardial infarction. *J Am Coll Cardiol* 37: 1590–7.
 22. Wijnmaalen AP, van der Geest RJ, van Huls van Taxis CF, Siebelink HM, et al. (2011) Head-to-head comparison of contrast-enhanced magnetic resonance imaging and electroanatomical voltage mapping to assess post-infarct scar characteristics in patients with ventricular tachycardias: real-time image integration and reversed registration. *Eur Heart J* 32: 104–14.
 23. Desjardins B, Crawford T, Good E, Oral H, Chugh A, et al. (2009) Infarct architecture and characteristics on delayed enhanced magnetic resonance imaging and electroanatomic mapping in patients with postinfarction ventricular arrhythmia. *Heart Rhythm* 6: 644–51.
 24. Codreanu A, Odille F, Aliot E, Marie PY, Magnin-Poull I, et al. (2008) Electroanatomic characterization of post-infarct scars comparison with 3-dimensional myocardial scar reconstruction based on magnetic resonance imaging. *J Am Coll Cardiol* 52: 839–842.
 25. Gupta S, Desjardins B, Baman T, Ilg K, Good E, et al. (2012) Delayed-enhanced MR scar imaging and intraprocedural registration into an electro-anatomical mapping system in post-infarction patients. *JACC Cardiovasc Imaging* 5: 207–10.
 26. Desjardins B, Yokokawa M, Good E, Crawford T, Latchamsetty R, et al. (2013) Characteristics of intramural scar in patients with nonischemic cardiomyopathy and relation to intramural ventricular arrhythmias. *Circ Arrhythm Electrophysiol* 6: 891–7.
 27. Spears DA, Suszko AM, Dalvi R, Crean AM, Ivanov J, et al. (2012) Relationship of bipolar and unipolar electrogram voltage to scar transmural and composition derived by magnetic resonance imaging in patients with nonischemic cardiomyopathy undergoing VT ablation. *Heart Rhythm* 9: 1837–46.
 28. Tokuda M, Tedrow UB, Inada K, Reichlin T, Michaud GF, et al. (2013) Direct comparison of adjacent endocardial and epicardial electrograms: implications for substrate mapping. *J Am Heart Assoc.* 2: e000215.
 29. van Slochteren FJ, Teske AJ, van der Spoel TI, Koudstaal S, Doevendans PA, et al. (2012) Advanced measurement techniques of regional myocardial function to assess the effects of cardiac regenerative therapy in different models of ischaemic cardiomyopathy. *Eur Heart J Cardiovasc Imaging* 13: 808–18.
 30. Heiberg E, Sjögren J, Ugander M, Carlsson M, Engblom H, et al. (2010) Design and validation of Segment—freely available software for cardiovascular image analysis. *BMC Medical Imaging* 10: 1–13.
 31. Holland PW, Welsch RE (1977) Robust Regression Using Iteratively Reweighted Least-Squares. *Communications in Statistics: Theory and Methods*, A6, pp.813–827.
 32. Cohen J (1988) *Statistical power analysis for the behavioral sciences* (2nd ed.). Hillsdale, NJ: Lawrence Erlbaum Associates
 33. Amado LC, Gerber BL, Gupta SN, Rettmann DW, Szarf G, et al. (2004) Accurate and objective infarct sizing by contrast-enhanced magnetic resonance imaging in a canine myocardial infarction model. *J Am Coll Cardiol* 44: 2383–9.

**4.2. LONG-ACTING BENEFICIAL EFFECT OF PERCUTANEOUSLY
INTRAMYOCARDIALLY DELIVERED SECRETOME OF APOPTOTIC
PERIPHERAL BLOOD CELLS ON PORCINE CHRONIC ISCHEMIC LEFT
VENTRICULAR DYSFUNCTION**



Long-acting beneficial effect of percutaneously intramyocardially delivered secretome of apoptotic peripheral blood cells on porcine chronic ischemic left ventricular dysfunction



Noemi Pavo^a, Matthias Zimmermann^b, Dietmar Pils^c, Michael Mildner^d, Zsolt Petrás^e, Örs Petneházy^e, János Fuzik^a, András Jakab^f, Christian Gabriel^g, Wolfgang Sipos^h, Gerald Maurer^a, Mariann Gyöngyösi^{a,1}, Hendrik Jan Ankersmit^{b,i,*,1}

^a Department of Cardiology, Medical University of Vienna, Austria

^b Department of Thoracic Surgery, Medical University of Vienna, Austria

^c Department of Obstetrics and Gynecology – Molecular Oncology Group, Medical University of Vienna, Austria

^d Department of Dermatology, Medical University of Vienna, Austria

^e Institute of Diagnostic Imaging and Radiation Oncology, University of Kaposvar, Hungary

^f Department of Biomedical Imaging and Image-guided Therapy, Medical University of Vienna, Austria

^g RedCrossTransfusion Service for Upper Austria, Linz, Austria

^h Clinical Department for Farm Animals and Herd Management, University of Veterinary Medicine, Vienna, Austria

ⁱ Christian Doppler Laboratory for Cardiac and Thoracic Diagnosis and Regeneration, Vienna, Austria

ARTICLE INFO

Article history:

Received 23 November 2013

Accepted 20 December 2013

Available online 16 January 2014

Keywords:

Cell-free regeneration therapy

Gene expression

Immunomodulation

Myocardial infarction

Remodeling

Animal model

ABSTRACT

The quantity of cells with paracrine effects for use in myocardial regeneration therapy is limited. This study investigated the effects of catheter-based endomyocardial delivery of secretome of 2.5×10^9 apoptotic peripheral blood mononuclear cells (APOSEC) on porcine chronic post-myocardial infarction (MI) left ventricular (LV) dysfunction and on gene expression. Closed-chest reperfused MI was induced in pigs by 90-min occlusion followed by reperfusion of the mid-LAD (day 0). At day 30, animals were randomized to receive porcine APOSEC ($n = 8$) or medium solution (control; $n = 8$) injected intramyocardially into the MI border zone using 3D NOGA guidance. At day 60, cardiac MRI with late enhancement and diagnostic NOGA (myocardial viability) were performed. Gene expression profiling of the infarct core, border zone, and normal myocardium was performed using microarray analysis and confirmed by quantitative real-time PCR. Injection of APOSEC significantly decreased infarct size ($p < 0.05$) and improved cardiac index and myocardial viability compared to controls. A trend towards higher LV ejection fraction was observed in APOSEC vs. controls ($45.4 \pm 5.9\%$ vs. $37.4 \pm 8.9\%$, $p = 0.052$). Transcriptome analysis revealed significant downregulation of caspase-1, tumor necrosis factor and other inflammatory genes in APOSEC-affected areas. rtPCR showed higher expression of myogenic factor Mefc2 ($p < 0.05$) and downregulated caspase genes ($p < 0.05$) in APOSEC-treated pigs. In conclusion, overexpression of MEF2c and repression of caspase was related to decreased infarct size and improved cardiac function in secretome-treated animals. Altered gene expression 1-month post-APOSEC treatment proved the long-acting effects of cell-free therapy with paracrine factors.

© 2014 The Authors. Published by Elsevier Ltd. Open access under [CC BY license](http://creativecommons.org/licenses/by/4.0/).

* Corresponding author. Christian Doppler Laboratory for Cardiac and Thoracic Diagnosis and Regeneration, Department of Thoracic Surgery, Medical University of Vienna, Waehringer Guertel 43 18-20, A-1090 Vienna, Austria. Tel.: +43 1 40400 6777 (office), +43 1 40400 6857 (lab); fax: +43 1 40400 6977.

E-mail address: hendrik.ankersmit@meduniwien.ac.at (H.J. Ankersmit).

¹ H.J. Ankersmit and M. Gyöngyösi share the last authorship.

1. Introduction

Although great effort has been made to replace infarcted myocardium with regenerative cells, the current methods have shown marginal efficacy in clinical applications [1–5]. According to the ‘dying stem cell’ hypothesis, regenerative stem cells are already undergoing apoptosis even as they are being delivered into the ischemic myocardium [4]. Thus, the best way to attenuate infarction may be to induce immunomodulatory mechanisms in a

paracrine manner [5–8]. We have shown previously that the secretome of apoptotic peripheral blood cells (APOSEC), which is derived from large numbers of easily-obtainable peripheral blood mononuclear cells (PBMCs), can be used to therapeutically regenerate the myocardium after acute ischemic injury [9–12].

The optimal mode of delivering reparative cells or substances into the ischemic myocardium (i.e. intracoronary or percutaneous intramyocardial delivery) is still a matter of debate. Intracoronary delivery of cells increases the risk of temporary occlusion of the infarct-related artery and requires active migration of the cells from the vessel lumen to the injured tissue site [13]. The inherent disadvantages of cell therapy include the obvious limitations of the relatively small number of autologous adult cells that are available and the relatively large injection volume of the cells, especially for intramyocardial application [14,15]. Using APOSEC, which contains a mixture of cytokines and growth factors, might avoid the disadvantages of cell-based therapies and be more feasible while also enhancing therapeutic efficiency.

Due to the early death of many regenerative cells when injected into the necrotic core, intramyocardial regenerative therapies instead target the infarct border zone, which shows signs of hibernating myocardium. Interestingly, some reports have described the metabolic, proteomic, and genomic differences between the infarct core and remote (normal) myocardium, but there is no genomic information about this special border zone of infarction

[16,17]. Furthermore, no studies have investigated the effects of secretome-based therapies on gene expression in the core and border zone of myocardial infarction (MI).

We hypothesized that percutaneous intramyocardial delivery of APOSEC would be safe and effective in a clinically relevant porcine model of chronic left ventricular (LV) dysfunction after MI. We further hypothesized that the trophic effect of APOSEC could cause structural changes, leading to improved hemodynamic function post-MI via altered gene expression. In our experiments we have injected APOSEC or placebo locally intramyocardially into the border zone of infarction using the catheter-based 3D NOGA-guided intramyocardial application method and investigated the LV function, infarct size and gene expression of the ischemic injured myocardium.

2. Materials and methods

2.1. Porcine model of acute MI and APOSEC production

This study used a porcine closed-chest reperfused acute MI model. Domestic pigs ($n = 22$) underwent percutaneous 90-min balloon occlusion of the mid-left anterior descending coronary artery (LAD) followed by reperfusion (Fig. 1 and Supplementary Materials and Methods). APOSEC was produced from pig PBMCs (Supplementary Materials and Methods). Animal investigations were carried out in accordance with the “Position of the American Heart Association on Research Animal Use,” as adopted by the AHA on November 11, 1984. The study was approved by the Ethics Committee on Animal Experimentation at the University of Kaposvar, Hungary.

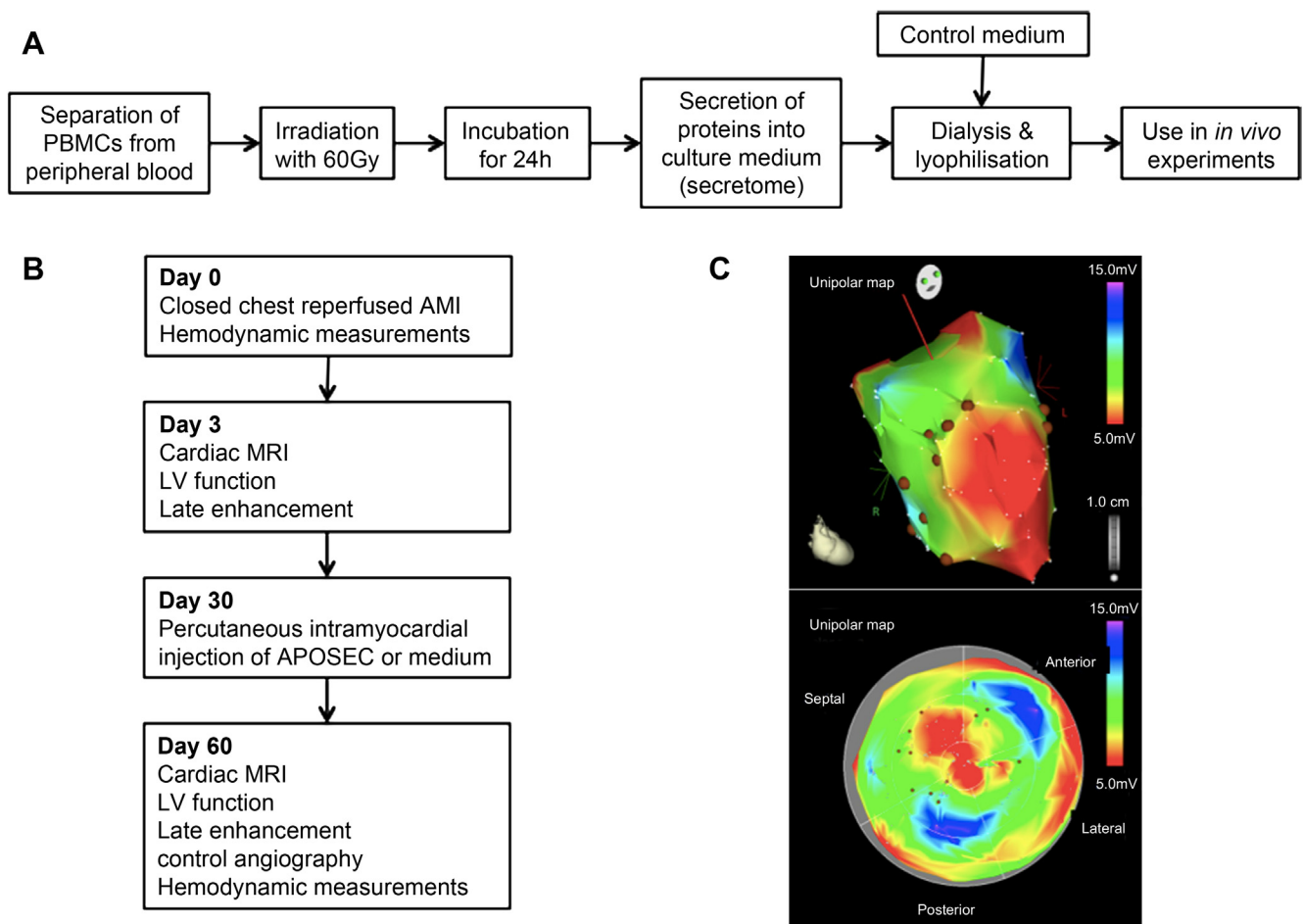


Fig. 1. Study design. A. Schematic showing how APOSEC is prepared from peripheral blood mononuclear cells (PBMCs). B. Study design. C. 3D views of the left ventricle derived by NOGA endocardial mapping and NOGA-guided injection into the border zone of chronic infarction. Brown dots mark the locations of the intramyocardial injections in the border zone of infarction. Color-coded 3D image (upper) were converted to a 2D polar map (below). Red represents non-viable infarcted myocardium, while green and yellow indicated the border zone of infarction. Normal viable myocardium is colored blue and purple.

2.2. Percutaneous intramyocardial delivery of APOSEC or medium solution using 3D NOGA guidance

One month after MI (day 30; development of scar and LV remodeling; Fig. 1), the animals were sedated, intubated, and the patency of the infarct-related artery was confirmed by coronary angiography. LV hemodynamic parameters were measured via pigtail catheters. NOGA endocardial mapping was performed using a percutaneous NOGA Star catheter (Cordis, Johnson & Johnson, Miami Lakes, FL, USA) as described previously [18]. After creation of the 3D shape of the LV infarction, the diagnostic NOGA Star catheter was replaced by a NOGA MyoStar injection catheter (Cordis, Johnson & Johnson). The pigs were randomized to receive either APOSEC (derived from 2.5×10^9 PBMCs, resuspended in 4 ml physiologic saline, 300- μ l aliquots) or medium as a control (resuspended lyophilized Cell Growth medium) in 11 ± 1 locations of the border zone of infarction using 3D NOGA-guided percutaneous intramyocardial delivery. The animals were allowed to recover. At 60 days post-infarction (30 days post-injection), control coronary angiography and NOGA endocardial mapping were performed while the pigs were under general anesthesia.

2.3. Cardiac magnetic resonance imaging (MRI)

Cardiac MRI with late enhancement (LE) was performed 3 days and 60 days after the reperused acute MI procedure using a 1.5-T clinical scanner (Avanto, Siemens, Erlangen, Germany) with a phased-array coil and a vector ECG system (Supplementary Materials and Methods). The LV end-diastolic (EDV) and end-systolic (ESV) volumes, ejection fraction (EF), and infarct size were measured (Supplemental Materials and Methods) [19].

2.4. LV hemodynamic measurements

LV hemodynamic measurements were performed via pigtail catheter and included systolic aortic pressure, LV systolic and end-diastolic pressures (EDP), LV contractility expressed as dp/dt and $dp/dt/P$, and LV end-diastolic stiffness (LV EDP/EDV).

2.5. Myocardial viability, infarct transmural and regional functional assessment by NOGA

Using the 12-segment polar map analysis principles, the mean unipolar, bipolar, and local linear shortening values (UPV, BiP, and LLS, respectively) of the injected areas were calculated and reported as mV or %, respectively.

2.6. Histology

The hearts were explanted at day 60 and sliced, and representative specimens of normal tissue and of the border zone and infarcted areas were fixed in 10% neutral buffered formalin, embedded in paraffin, sectioned, and stained for hematoxylin-eosin, angiogenic marker of CD31 and stem cell factor CD117 (Supplemental Materials and Methods).

2.7. Gene expression analysis using RNA microarrays and real-time PCR (rtPCR)

Tissue samples for RNA extraction were obtained directly from the infarct core, border zone, and remote myocardium and stored in RNAlater (Qiagen, Germany) at -20°C . Total RNA was isolated from tissue samples using the RNeasy Microarray Tissue Mini Kit (Qiagen, Germany). RNA quality was checked on RNA Nano chips using the Agilent 2100 Bioanalyzer platform (Agilent Technologies).

2.7.1. RNA microarrays

Microarray gene analysis was performed by Miltenyi (Miltenyi Biotec GmbH, Germany) (Supplementary Materials and Methods). The fluorescence signals of the hybridized Agilent Microarrays were measured using Agilent's Microarray Scanner System (Agilent Technologies) and analyzed using Agilent Feature Extraction Software (FES).

Raw hybridization values were loaded into R (GNU R) using the R-package limma (v3.14.4) [20,21]. Microarray data have been uploaded to the Gene Expression Omnibus database (<http://www.ncbi.nlm.nih.gov/geo/query/acc.cgi?acc=GSE47397>). Biological interpretation of significant gene lists was performed using the Database for Annotation, Visualization and Integrated Discovery (DAVID) v6 [22]. Data were reported in annotational clusters or as single gene expression, heat maps, and Venn diagrams.

2.7.2. rtPCR of selected genes

The mRNA of myocardial probes of all 3 regions from both groups of pigs was reverse transcribed to cDNA (Qiagen, Germany) and expression was quantified by rtPCR (Applied Biosystems 7500 Real-Time PCR System, Life Technologies, USA). The primers for the target sequences were designed using Primer3 software (http://primer3.wi.mit.edu/primer3web_help.htm; Microsynth, Switzerland) (Supplemental Table 1). The expression rates of the target genes were normalized to the geometric means of the housekeeping genes GAPDH, HPRT1, and PPIA, which were selected as endogenous controls due to their stable expression. The relative gene expression level was calculated using the ΔCt method (i.e. expression level

relative to an endogenous control). The expression changes were calculated relative to expression levels in the normal myocardium of the same animal.

2.8. Statistics

Continuous data of the two groups of pigs are reported as mean \pm standard deviation. Differences between the groups were tested using the Student's *t* test for continuous variables and the χ^2 test for categorical variables. A difference was considered statistically significant at $p < 0.05$. Data analyses and interpretations were performed by an experienced observer who was blinded to the randomization and to all study results. Statistical analysis was performed using SPSS 18.0 (SPSS Inc, USA) software.

For gene array analysis, to test for all comparisons (i.e. differences between regions of interest: normal, border, and infarct and APOSEC vs. control) a linear model for each gene was fitted and the estimated coefficients and standard errors for these contrasts were computed. Subsequently, moderated *t*-statistics, moderated *F*-statistics, and the log-odds of differential expression were calculated by empirical Bayes shrinkage of the standard errors towards a common value. False discovery rates (FDR) below 5% were considered statistically significant for each comparison. Higher FDR cut-offs were used for some contrasts, especially for the use of the gene lists for biological interpretation. Unsupervised hierarchical clustering was performed with the Euclidean distance as the distance function and the Ward algorithm in R, using centered and scaled log₂ expression values. Principal Component Analysis (PCA) was also performed for centered and scaled values.

3. Results

3.1. Effect of APOSEC on infarct size and hemodynamics

Six pigs died during the reperused MI procedure ($n = 5$) or 2 days later ($n = 1$). The remaining 16 pigs were randomized to the APOSEC group ($n = 8$) or to the control group ($n = 8$).

Figs. 2 and 3 show the 3-day and final MRI data. Compared to control animals, the APOSEC-treated animals had significantly smaller infarcts ($13.92 \pm 1.34\%$ vs. $21.58 \pm 2.09\%$, $p < 0.05$) and a significantly higher cardiac index (4.40 ± 3.94 l/min/m² vs. 3.07 ± 2.35 l/min/m², $p < 0.05$). There was also a trend towards a higher EF ($45.4 \pm 5.9\%$ vs. $37.4 \pm 8.0\%$, $p = 0.052$) and significant changes in LV EF from baseline to follow-up (FUP) in the APOSEC-treated vs. control animals. The area at risk as measured by MRI at day 3 was similar in the two groups ($46 \pm 9\%$ vs. $45 \pm 10\%$ of the entire LV myocardium).

The baseline, pre-injection, and post-injection hemodynamic data was not different between the groups (data not shown). Significantly lower EDP and end-diastolic stiffness was measured in the APOSEC group at the final FUP (Fig. 3). Infarct transmural, as assessed by MRI and NOGA bipolar maps, showed smaller transmural infarctions in the APOSEC-treated pigs (Fig. 2). The APOSEC-treated animals had significantly higher UPV and BiP values for the treated area with a trend towards higher LLS (Fig. 4).

3.2. Angiogenesis and homing of endogenous c-kit positive cells in the border zone of experimental MI

There was a significant increase in the number of CD31+ cells in the APOSEC group in the border zone of infarction, indicating enhanced angiogenesis (Fig. 5). The CD31+ cell density per DAPI positive cells in the infarct and border zone were $15.3 \pm 1.9\%$ vs. $12.6 \pm 4.5\%$ and $19.9 \pm 1.8\%$ vs. $11.3 \pm 3.2\%$ in the APOSEC vs. controls. Significantly ($p < 0.05$) higher numbers of CD117+ cells were found in infarct core ($2.0 \pm 0.9\%$ vs. $0.6 \pm 0.7\%$) and border area ($3.0 \pm 1.4\%$ vs. $0.9 \pm 0.8\%$) in APOSEC-pigs suggesting enhanced accumulation of endogenous cardiac stem cells as compared with medium-treated animals.

3.3. Gene expression differences between APOSEC- and medium-treated animals

Differential gene expression of infarcted, border zone, and remote myocardium in the chronic failing hearts before treatment is

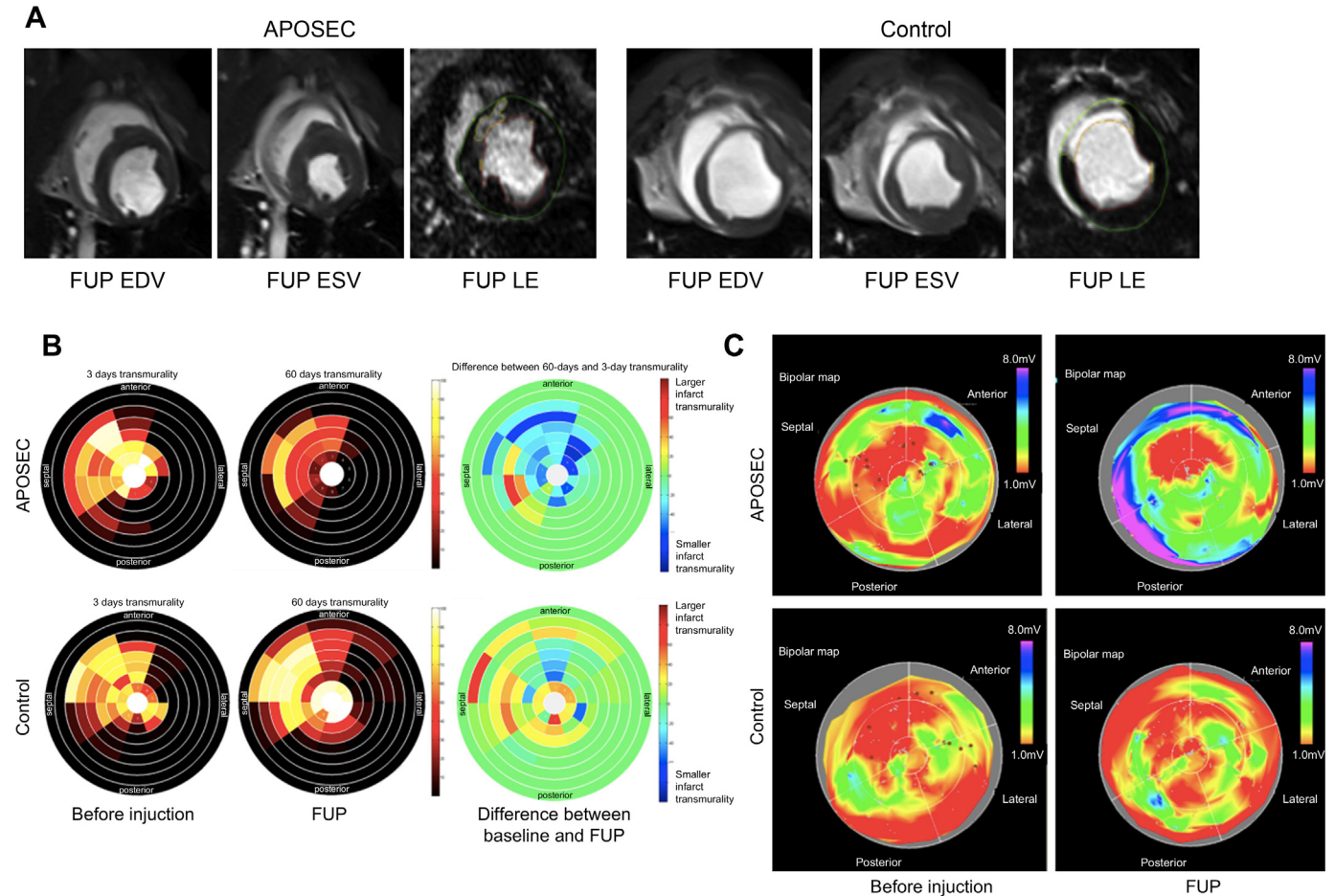


Fig. 2. Left ventricular function and infarct transmuralty assessed by MRI and NOGA. **A.** Short axis views of follow-up (FUP) late enhancement (LE) magnetic resonance images show end-diastolic (EDV) and end-systolic (ESV) contours with LE 30 days after percutaneous intramyocardial injection of APOSEC or medium solution. Note the reduced ventricular volumes and infarct area in an APOSEC-treated pig. **B.** Bull's eye plots of LE-MRI data demonstrating treatment effects in representative APOSEC-treated (top row) and medium-treated (control) pigs (bottom row). Note that segmental infarct transmuralty is reduced in the FUP images of an APOSEC-treated pig, while slight enlargement of the infarct area is seen in a medium solution-treated pig. The following segments are affected: middle anterior, middle anteroseptal, apical anterior, and apical septal. Left and middle panels: segmental infarct transmuralty in 3-day and 30 days after injection (FUP, day-60) MR images. Transmuralty was measured as the percentage of the LE area (i.e. the scar) relative to the volume of the corresponding myocardial segment. Right panels: treatment effects as visualized by differences between FUP and day-3 segmental measurements. Positive values refer to growing segmental infarct transmuralty (red) while negative values indicate reduced infarct transmuralty (blue). **C.** Bull's eye plots of NOGA bipolar (transmuralty) maps at baseline (injection) and FUP corresponding to the MRI polar plots (B) in the same APOSEC- and control pigs. Red represents greater infarct transmuralty.

shown in the [Supplemental Results](#). PCA and hierarchical clustering of the gene expression patterns of the corresponding myocardial areas in APOSEC- and medium-treated animals revealed 10 genes in the infarct core and 23 genes in the globally treated areas (infarct core and border zone) that showed significantly different expression compared to remote myocardium ([Fig. 6](#), [Table 1](#)). Systematic and integrative gene analysis using DAVID Bioinformatics Resources identified and classified only a portion of the significantly up and downregulated genes (11 of 23 genes, 47.8%). Due to the expression of single genes in several pathways, these genes could not be classified into unique clusters. There was significant downregulation of apoptosis-, inflammation-, and lipid metabolism-associated genes. This included repression of caspase-1 (apoptosis-related cysteine peptidase and interleukin 1-beta-convertase), tumor necrosis factor alpha (TNF-alpha), stromal derived factor (SDF)2-like protein 1 (endoplasmic reticulum stress-inducible gene), arachidonate 15-lipoxygenase (lipid metabolism), uroplakin 1B (coding a transmembrane protein), claudin 3 (tight junction protein), and other genes that were not characterized further.

Using less-stringent criteria (FDR <10%), additional 53 genes were detected that showed different expression levels in the APOSEC group vs. the control group. Of these, 24 genes were

identified by the functional annotation analysis ([Table 1](#)). Six of the 24 genes were overexpressed, while 18 were repressed.

The APOSEC-affected myocardial area showed upregulation of insulin-like growth factor (an angiogenic growth factor), Kruppel-like factor (a regulator of vascular tone and homeostasis and an anti-atherogenic), myozenin (a gamma-filamin and alpha-actinin-binding protein in skeletal muscles), and a gene similar to glyceronephosphate O-acyltransferase (thought to protect cells from oxidative stress). In contrast, some of the downregulated genes belonged to the inflammatory and immune system superfamily: killer cell lectin-like receptor subfamily K, cystatin F, ectonucleoside triphosphate diphosphohydrolase 1, CD2, complement component 1 q subcomponent, A-chain, C-X-C motif ligand 9 and 10, C-type lectin domain family 5, member A, CD247, and beta-2 microglobulin. Other downregulated genes included some involved in lipid metabolism (a scavenger receptor for phosphatidylserine and oxidized low density lipoprotein), a histocompatibility antigen (MHC class II DR-alpha), a structural matrix protein (ameloblastin), and other less well characterized genes (suppression-inducing transmembrane adapter 1).

If FDR <20% was used (data available at the GEO homepage), additional annotated overexpressed genes in the border area of

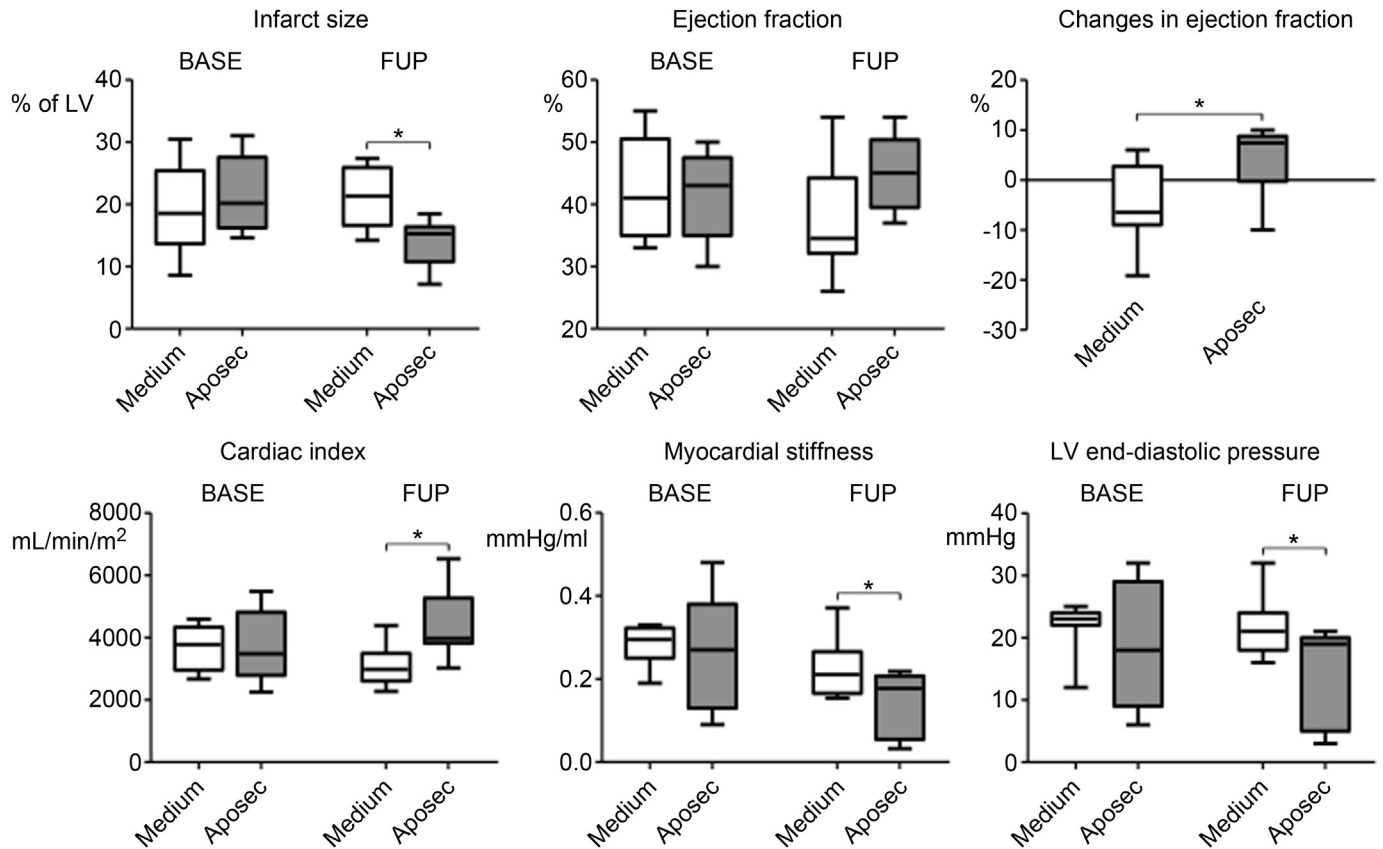


Fig. 3. MRI results. Ejection fraction (EF) at day 3 (BASE) and at day 60 (follow-up; FUP) showing a significant increase in EF at FUP in the APOSEC-treated pigs ($n = 8$) compared to the control pigs ($n = 8$). The APOSEC-treated pigs showed significantly smaller infarct size and better cardiac indexes. There was significantly lower end-diastolic pressure and end-diastolic stiffness in the APOSEC-treated group. * $p < 0.05$.

APOSEC-treated animals belonged to 42 clusters (an additional 686 genes). These clusters included genes involved in purine metabolism (phosphodiesterase 3A, 4A, and 4B, pyruvate kinase), in the cell cycle (e.g. fuzzy/cell division cycle 20 related 1), in the calcium signaling pathway (adrenergic beta-1 receptor, nitric oxide synthase 2, inducible, calmodulin), and in regulation of the actin cytoskeleton (fibronectin receptor, vinculin/cell adhesion related gene/). The clusters also included other cardiac-related genes, such as myocardin (important for cardiomyocyte survival and maintenance), GATA-binding protein 4 (transcription factor needed for normal heart development), and adrenergic beta-1 receptor. The main clusters of downregulated genes in the border zone of the APOSEC-treated animals included genes responsible for toll-like receptor pathways (CD40 molecule, CD86 molecule, chemokine ligands, interleukin-1 receptor-associated kinase 4, and toll-like receptor 3 and 7, which are responsible for the innate immune response and mediation of ischemic/reperfusion injury), and genes involved in cardiomyopathy (transforming growth factor beta).

3.4. rtPCR

rtPCR analysis of mRNA expression in the border zone of infarction in the APOSEC-treated animals confirmed that there was significant overexpression of the cardiac myogenesis and vascular development gene, myocyte-specific enhancer factor 2C (MEF2c), and repression of the apoptosis regulator caspase-3 (Fig. 6). In the border zone, there was a trend towards higher expression ($p < 0.1$) of angiogenic regulatory factor hypoxia-inducible factor 1-alpha and transcription factor GATA-4 in the APOSEC group compared

with the control group. There were no significant differences between the groups in terms of the expressions of genes involved in stem cell homing (CXCR12), the transcription factor myogenin, and the extracellular matrix metalloproteinase-9 and transforming growth factor beta.

4. Discussion

Here we demonstrated that 3D NOGA-guided injection of APOSEC is safe, feasible, and effective. APOSEC injection was associated with an enhanced vascular density and homing of c-kit+ endogenous stem cells in the peri-infarct and infarcted area, with a reduction of infarct size, and with a significant increase in LV EF contractile function. Gene profiling analysis of the APOSEC-treated myocardial areas revealed that there was downregulation of inflammatory and apoptotic genes. Post-hoc validation of gene expression by rtPCR showed higher expression levels of myogenic factor and *Mefc2* and robust downregulation of apoptosis regulator caspase-3.

We previously showed that similar to the secretome of mesenchymal stem cells (MSCs) [23], APOSEC contains anti-apoptotic and regenerative factors that promote angiogenesis and myocardial repair [11,12]. In contrast to MSCs, PBMCs contain different types of mononuclear cells. However, one big advantage of PBMCs is that the available autologous cells are numerous. Even if ex vivo cell culture expansion of MSCs might provide sufficient quantities of secretome, the biological characteristics of the MSC secretome depend on the number of passage of the cells with possibility to chromosome variability after passage 4, and on the cell donor, making it difficult to standardize secretome production

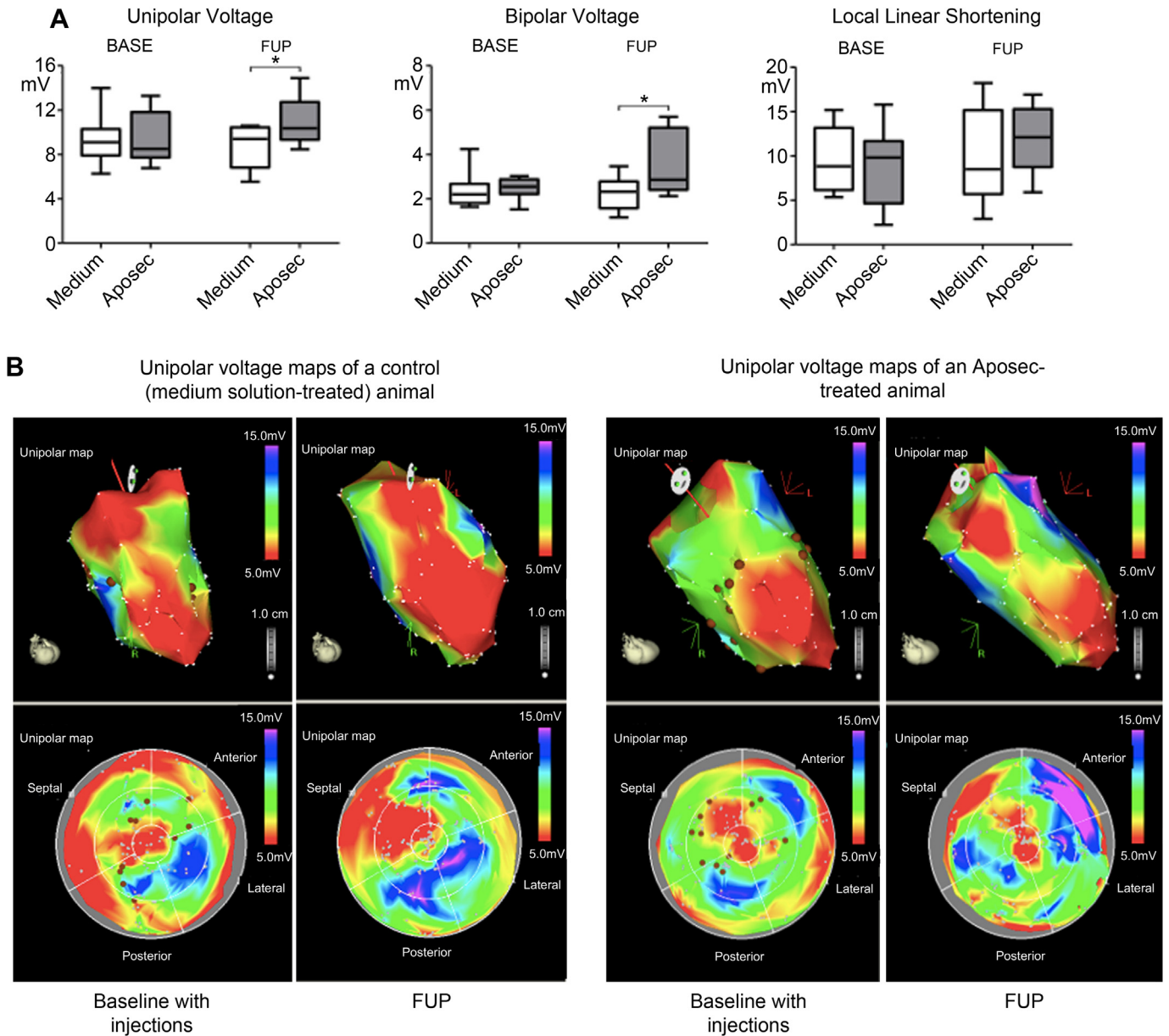


Fig. 4. NOGA results and representative NOGA images. A. Baseline (BASE) and follow-up (FUP) unipolar voltage (an index of myocardial viability) of the injected area of APOSEC- and medium-treated (control) pigs. At FUP (day-60), the APOSEC group had significantly higher unipolar voltage values (left) and bipolar voltage (index of infarct transmuralty) values. There were trends towards higher local linear shortening voltage values (an index of segmental wall motion) at FUP. B. Representative NOGA images show the injection points around the infarcted area in APOSEC- and medium-treated pigs. The infarcted area is visibly smaller at FUP in the APOSEC-pigs, indicating that ventricular remodeling was reduced in these animals. Color coding is as defined in Fig. 1.

in large amount. Notably, a pre-defined mixture of known regenerative factors did not exert effects that were similar to those of the naturally derived secretome [23].

Our experiments investigated changes in the gene expression profile of the host tissue (ischemically injured myocardial cells) after direct contact with the injected mixture of paracrine factors (APOSEC). Even if reparative cells in cell-based therapies that are delivered to the ischemic area produce numerous signaling molecules, such as matrix proteins and anti-inflammatory and angiogenic substances, the host tissue response is the crucial factor in myocardial tissue regeneration.

Changes in gene expression in ischemic cells depend on the severity of the injury. Interestingly, APOSEC mainly caused gene silencing in the pro-inflammatory cascade along with, to a lesser extent, some gene induction. However, it is important to note that

almost half of the downregulated genes, and none of the upregulated genes, had currently known functions. These latter genes might belong to metabolic, angiogenic, or myogenic functional clusters that cause synergistic regenerative processes as demonstrated by infarct size reduction and prevention of ventricular remodeling.

4.1. APOSEC induces long-lasting differences in gene expression

Although the studies were exploratory, previous analyses of the gene expression profiles of chronically infarcted, reperfused, and remodeled ischemic myocardium identified functional uni- or bimodal genes with known functions [24–30]. The published data, which are mostly from studies conducted in rodent MI models, are heterogeneous in terms of the number and type of differentially-

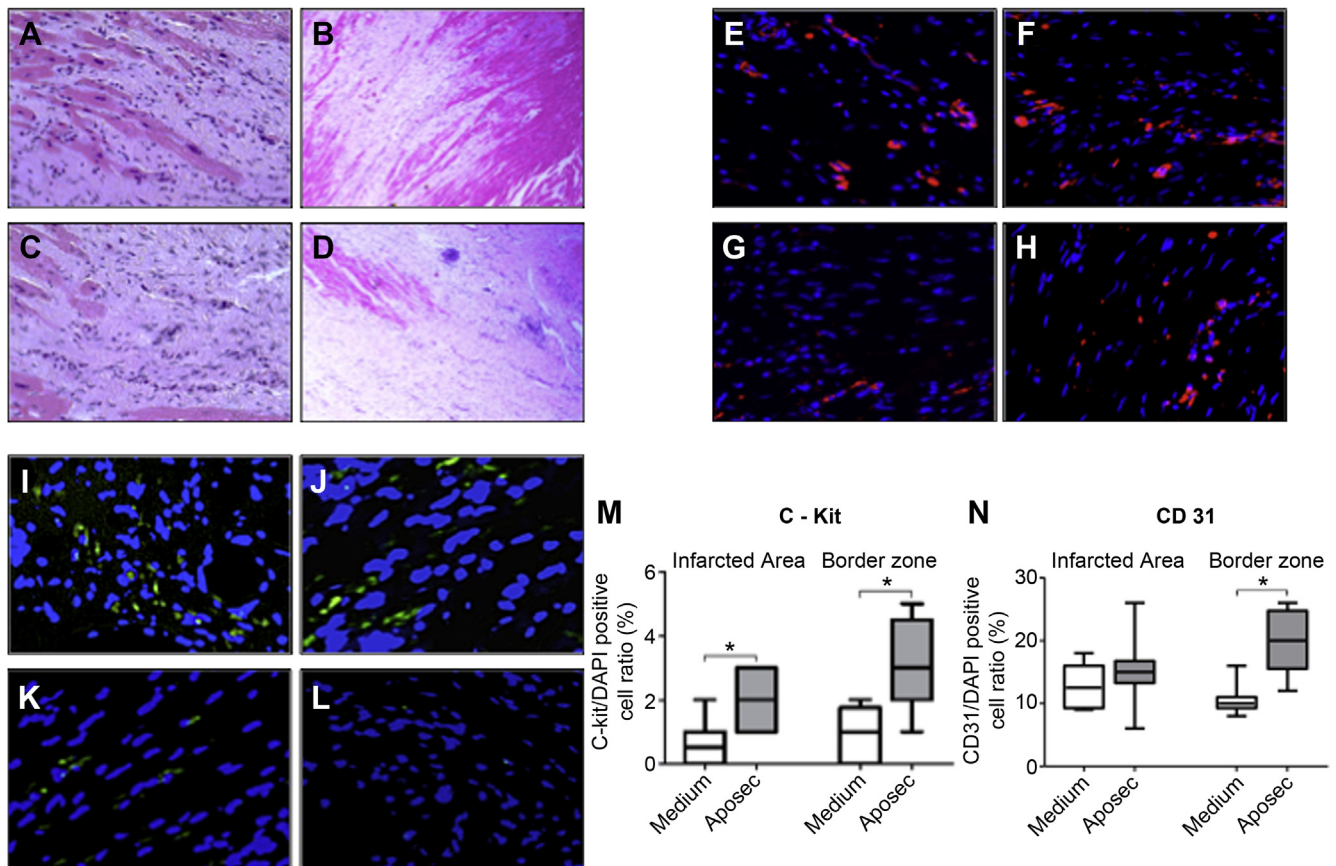


Fig. 5. Angiogenic effect of APOSEC. A–D. H&E stained porcine myocardium 60 days after induction of myocardial infarction and treated with intramyocardial injection of APOSEC or medium (infarct core A and C, /40 \times magnification/, and border zone of infarction B and D, /10 \times magnification/, respectively). E–H. Immunofluorescence CD31+ staining of the infarct core (E and G) and border areas (F and H) of an APOSEC or medium-treated pig, respectively. Red indicates CD31+ cells, counterstaining with DAPI. I–L. CD117 (c-kit+) immunofluorescence staining of the infarct core (I and K) and border areas (J and L) of an APOSEC or medium-treated pig, respectively. Green color represents CD117+ cells, counterstained with DAPI. M and N. APOSEC-treated pigs show a higher density of CD31+ and CD117+ cells both in infarct core and border areas, indicating enhanced level of microvascularization and homing of endogenous c-kit+ cardiac stem cells (* p < 0.05).

expressed genes. To our knowledge, this is the first report on gene expression profiles in closed-chest reperfused MI and also the first report to describe molecular biological changes in remote and infarcted myocardium and in the border zone of infarction (Supplemental Discussion).

Locally injected APOSEC contains paracrine factors proven to be anti-inflammatory, leading to repression of active pro-inflammatory genes, such as genes coding for TNF-alpha, SDF2-like protein 1, and caspase-1. However, several genes that showed significantly changed expression are currently not assigned to known function. The expansion of the FDR <5% cut-off to a FDR <10% cut-off gave more information about changes in gene expression in APOSEC-treated areas. Specifically, this less-stringent cut-off identified several relevant genes with altered expression. There was upregulation of angiogenic factors and other vascular tone and homeostasis regulators and repression of pro-inflammatory genes such as complement components and histocompatibility antigens.

4.2. Comparison with literature data

In contrast to the large animal model of reperfused MI used here, Jameel et al. surgically ligated the first and second diagonal branches of LAD of mini-swine and immediately injected 50 million bone marrow-derived multipotent progenitor cells [31]. This surgical cell transplantation resulted in a marked improvement in EF (51.2% vs. 35.7%) and in a decrease in infarct size (4.6% vs. 8.6%) at the 4-month FUP in treated vs. control groups, respectively,

without engraftment of the cells. Gene expression analysis revealed 41 downregulated and 11 upregulated genes in the cell transplantation group; the authors attributed these changes to the paracrine effects of the injected cells. There was also downregulation of genes in the inflammatory pathway, similar to what was seen in our experiments. The differences between the gene expression pathways identified in the two studies may due to the use of different MI models and treatments as well as to the presence of different paracrine mediators.

Similar to the MSC secretome [23], the secretome of apoptotic PBMCs (i.e. APOSEC) has the potential to block apoptosis and local inflammation, enhancing neoangiogenesis and limiting infarct expansion and remodeling. Through overexpression of regulatory genes at the FDR <10% level, such as Kruppel-like factor and myozenin, it is possible that APOSEC acts to restore vascular and muscle homeostasis. We did not see changes in any genes that are known to contribute to endogenous regeneration via the mobilization and homing of cardiac or bone marrow stem cells, such as genes coding for SDF-1 or for chemotactic cytokines. There is also the question of the importance of isolated gene expression i.e. expression of genes that are not functionally related to each other or that are in different pathways. However, small changes in the function of a key gene can act as a signal that triggers a biologically relevant effect.

rtPCR of selected genes confirmed the significant repression of the apoptosis regulator caspase-3. The increase in expression of hypoxia-inducible factor 1-alpha and GATA-4 in the border zone of

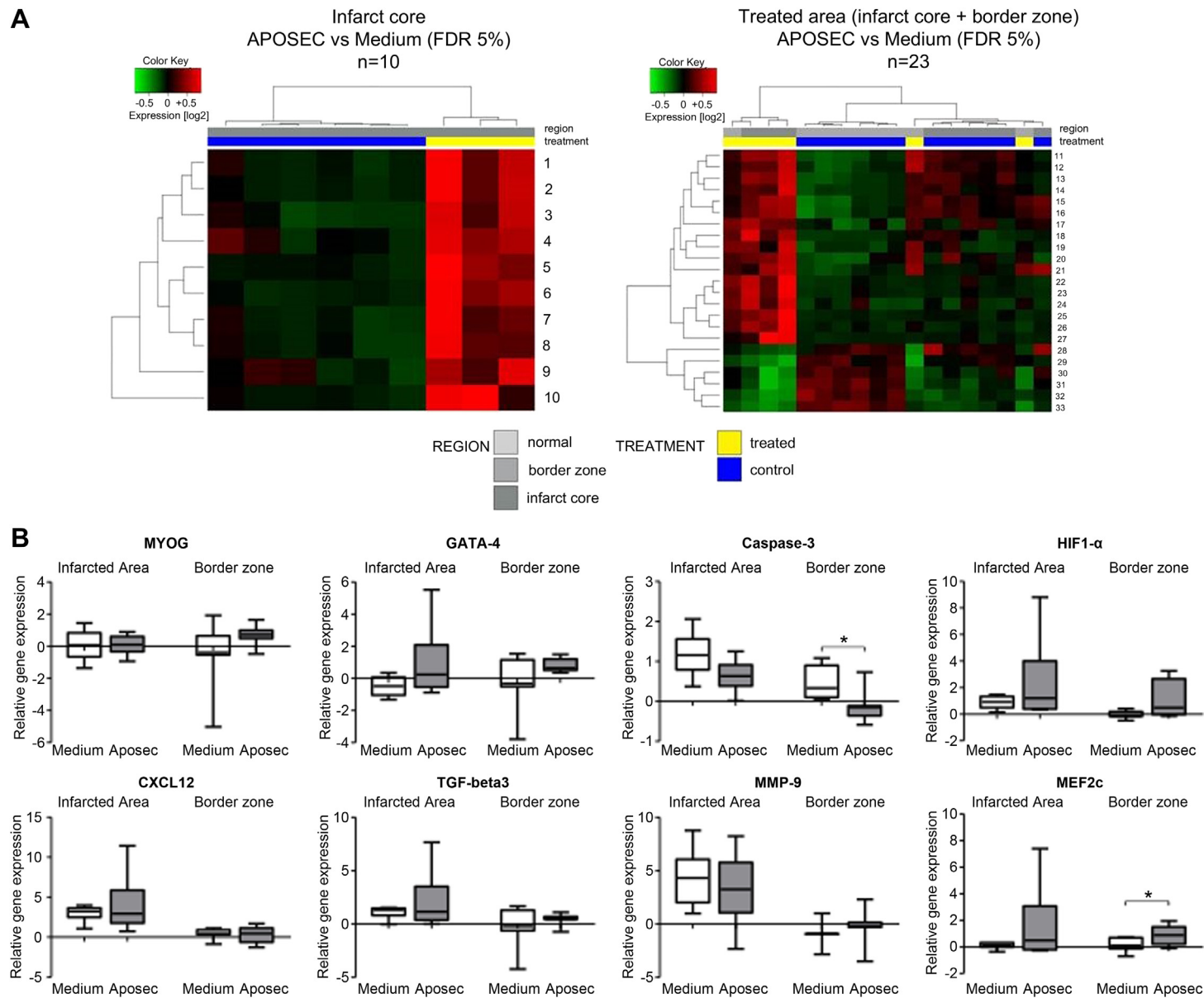


Fig. 6. Gene array analysis of differential expression of gene clusters in APOSEC-treated and medium-treated pigs in the infarct core and treated region (infarct core and border zone). A. Comparison of genes with significantly different expression levels [false discovery rate (FDR) 5%] in infarct (left) and treated regions (right; infarct core and border zone) of APOSEC- and medium-treated pigs (clustered and reported as a heat map). Name of genes: 1 = similar to LOC513955 protein; 2 = CD209 molecule; 3 = n.i.; 4 = claudin 3; 5 = n.i.; 6 = similar to trichohyalin; 7 = arachidonate 15-lipoxygenase; 8 = epididymal secretory protein; 9 = CD209 molecule; 10 = uroplakin 1B; 11 = n.i.; 12 = n.i.; 13 = n.i.; 14 = similar to trichohyalin; 15 = similar to Uncharacterized protein CXorf21 homolog; 16 = n.i.; 17 = caspase 1, apoptosis-related cysteine peptidase (interleukin 1. beta. convertase); 18 = n.i.; 19 = n.i.; 20 = tumor necrosis factor (ligand) superfamily member 13b; 21 = similar to Stromal cell-derived factor 2-like protein 1 precursor (SDF2-like protein 1) (PWP1-interacting protein 8); 22 = similar to LOC513955 protein; 23 = arachidonate 15-lipoxygenase; 24 = n.i.; 25 = epididymal secretory protein; 26 = uroplakin 1B; 27 = n.i.; 28 = n.i.; 29 = n.i.; 30 = n.i.; 31 = claudin 3; 32 = similar to Protein S100-A2 (S100 calcium-binding protein A2) (Protein S-100L); 33 = n.i. n.i. = not identified genes. B. Results of real-time PCR analysis of the expression of selected genes in APOSEC- and medium-treated pigs: HIF1- α : hypoxia-inducible factor 1- α ; MMP-9: matrix metalloproteinase-9, CXCL12: chemokine (C_X_C motif) ligand-12; MEF2c: myocyte-specific enhancer factor 2c; MYOG: myogenin; GATA-4: zinc finger transcription factor that binds to the DNA sequence "GATA"-4; TGF- β 3: transforming growth factor- β 3. Y axis: expression level normalized to gene expression of the normal myocardium. Each group: $n = 8$. * $p < 0.05$.

Table 1
Up and downregulated genes of the infarct core and combined treated (infarct core and border zone) areas in the APOSEC-treated animals.

Systematic name	Log fold changes	Adjusted P value	Name of gene	Regulation in APOSEC group
Infarct core FDR5%				
NM_001129972	-1.426	0.029	CD209 molecule	Down
NM_213931	-3.367	0.038	Arachidonate 15-lipoxygenase	Down
ENSSSCT00000010283	-0.675	<0.001	Similar to LOC513955 protein	Down
NM_001160075	-0.798	<0.001	Claudin 3	Down
ENSSSCT00000013027	-2.047	0.005	n.i.	Down
NM_001123212	-1.081	0.001	Uroplakin 1B	Down
TC533994	-1.573	0.043	n.i.	Down
ENSSSCT00000008105	-1.249	0.016	Epididymal secretory protein	Down
XM_001927650	-0.847	0.002	Similar to trichohyalin	Down
Combined treated areas FDR5%				
NM_214162	-1.887	0.029	Caspase 1-apoptosis-related cysteine peptidase (interleukin 1-beta-convertase)	Down
NM_001097498	-0.753	0.015	Tumor necrosis factor (ligand) superfamily member 13b	Down
ENSSSCT00000010283	-0.815	0.003	Similar to LOC513955 protein	Down
NM_001160075	-0.949	0.005	Claudin 3	Down
ENSSSCT00000013346	-1.18	0.007	Similar to uncharacterized protein CXorf21 homolog	Down
NM_001123212	-1.287	0.01	Uroplakin 1B	Down
ENSSSCT00000011046	-1.623	0.014	Similar to stromal cell-derived factor 2-like protein 1 precursor (SDF2-like protein 1) (PWP1-interacting protein 8)	Down
ENSSSCT00000007208	-2.936	0.015	Similar to Protein S100-A2 (S100 calcium-binding protein A2) (Protein S-100L)	Down
ENSSSCT00000008105	-1.249	0.016	Epididymal secretory protein	Down
XM_001927650	-0.908	0.022	Similar to trichohyalin	Down
NM_213931	-3.367	0.038	Arachidonate 15-lipoxygenase	Down
TC520240	-1.61	0.047	n.i.	Down
ENSSSCT00000013027	-2.617	0.013	n.i.	Down
AK233548	-1.097	0.015	n.i.	Down
ENSSSCT00000011046	-1.297	0.015	n.i.	Down
AK230687	-2.509	0.015	n.i.	Down
ENSSSCT00000011934	-1.895	0.016	n.i.	Down
A_72_P409998	0.929	0.007	n.i.	Up
TC601625	1.154	0.013	n.i.	Up
TC591961	0.592	0.015	n.i.	Up
TC540937	2.522	0.015	n.i.	Up
TC526711	3.032	0.029	n.i.	Up
AK232497	2.857	0.04	n.i.	Up
Combined treated areas FDR between 5% and 10%				
NM_214037	-1.42	0.093	Ameloblastin	Down
DQ845172	-1.5	0.097	Beta-2-microglobulin	Down
NM_213990	-1.51	0.093	C-type lectin domain family 5, member A	Down
NM_213776	-1.26	0.093	CD2 molecule	Down
NM_214155	-1.18	0.093	CD247 molecule	Down
NM_001008691	-3.35	0.093	Chemokine (C-X-C motif) ligand 10	Down
NM_001114289	-3.97	0.097	Chemokine (C-X-C motif) ligand 9	Down
NM_001003924	-1.89	0.093	Complement component 1, q subcomponent, A-chain	Down
NM_214153	-1.32	0.093	Ectonucleoside triphosphate diphosphohydrolase 1	Down
NM_214000	-0.95	0.008	Haptoglobin	Down
NM_213813	-2.46	0.063	Killer cell lectin-like receptor subfamily K, member 1	Down
NM_001097415	-0.81	0.089	Lymphocyte antigen 86	Down
NM_001113706	-1.64	0.093	MHC class II DR-alpha	Down
NM_213811	-2.36	0.076	Scavenger receptor for phosphatidylserine and oxidized low density lipoprotein	Down
ENSSSCT00000007803	-1.72	0.081	Similar to cystatin F	Down
AK232017	-2.63	0.097	Similar to signaling threshold-regulating transmembrane adapter 1 precursor (suppression-inducing transmembrane adapter 1) (SHP2-interacting transmembrane adapter protein) (gp30/40)	Down
NM_001001632	-1.45	0.08	Tropomyosin 3	Down
NM_213883	3.05	0.063	Insulin-like growth factor 2 (somatomedin A)	Up
NM_001134346	1.41	0.093	Kruppel-like factor 11	Up
NM_001025222	1.39	0.097	Myozenin 1	Up
ENSSSCT00000007708	0.92	0.093	Prion protein	Up
ENSSSCT00000011141	1.01	0.093	Similar to glyceronephosphate O-acyltransferase	Up
AY609888	0.67	0.081	Similar to NAD(P) dependent steroid dehydrogenase-like	Up
AY609888	0.78	0.097	Similar to NAD(P) dependent steroid dehydrogenase-like	Up

Further not identified genes at FDR 5-10%: downregulated: EW261758, NM_001243319, AK397775, DN121339, TC533994, TC544302, L21161, ENSSSCT00000000690, NM_001161643, ENSSSCT00000005170, A_72_P418159, A_72_P418159, AK394244, TC594134, TC569821, CK451290, TC608152, AK230519, TC591665, TC544851, NM_001256770, TC555560, ENSSSCT00000017072, A_72_P773461, TC611786, AK239173; and **upregulated in APOSEC-treated animals:** TC543654, TC614889, BX923234, AK349090.

FDR: false discovery rate, n.i.: not identified genes.

infarction showed trend towards higher expression in APOSEC-treated animals. MEF2c expression was induced and showed significant overexpression in the gene array when FDR <20% was used.

4.3. Limitations

Control animals received local intramyocardial injections of medium solution, therefore the gene expression might be different from that in non-treated infarcted animals. Therefore it is not appropriate to conduct a direct comparison of our “medium-solution-treated” control group with literature data that describe gene patterns in rodent ischemic/reperfusion hearts [30] or in rodent or pig chronic ischemia/infarction models using placebo, sham operation or no treatment in control animals [25–28,31].

Macroscopic identification of the real border zone of the infarction at day 60 that corresponds to the injected area at day 30 is crucial for obtaining valuable information from the experiments. In this study, localizing the LAD segment close to the origin of the second diagonal branch where the occlusion was made previously and identifying the margin of the infarcted area proved technically feasible. In addition, the differences in the gene expression profiles in the normal, border, and infarct areas confirmed that these areas were sampled correctly.

5. Conclusions

APOSEC attenuates chronic myocardial ischemia-induced ventricular remodeling in a clinically relevant large animal model. Specifically, APOSEC induced long-lasting differences in gene expression that led to silencing of genes involved in apoptosis and inflammation. The gene profiling results identified genes that represent targets for anti-remodeling and anti-ischemic therapy.

Conflict of interest

The authors declare competing financial interests. The Medical University of Vienna has a claimed financial interest (patent number EP2201954, WO2010070105-A1, filed 18 Dec 2008). HJA is a shareholder of Aposcience AG, which owns the rights to commercialize APOSEC for therapeutic use.

Funding

This study was funded by the Christian Doppler Research Association (Vienna, Austria), Aposcience AG (Vienna, Austria), the Ludwig Boltzmann Institute, and the Medical University of Vienna.

Appendix A. Supplementary data

Supplementary data related to this article can be found at <http://dx.doi.org/10.1016/j.biomaterials.2013.12.071>.

References

- [1] Orlic D, Kajstura J, Chimenti S, Limana F, Jakoniuk I, Quaini F, et al. Mobilized bone marrow cell repair the infarcted heart, improving function and survival. *Proc Natl Acad Sci USA* 2001;98:10344–9.
- [2] Jeevanantham V, Butler M, Saad A, Abdel-Latif A, Zuba-Surma EK, Dawn B. Adult bone marrow cell therapy improves survival and induces long-term improvement in cardiac parameters: a systematic review and meta-analysis. *Circulation* 2012;126:551–6.
- [3] Martín-Rendon E, Brunskill S, Dorée C, Hyde C, Watt S, Mathur A, et al. Stem cell treatment for acute myocardial infarction. *Cochrane Database Syst Rev* 2008;(4):CD006536.
- [4] Thum T, Bauersachs J, Poole-Wilson PA, Volk HD, Anker SD. The dying stem cell hypothesis: immune modulation as a novel mechanism for progenitor cell therapy in cardiac muscle. *J Am Coll Cardiol* 2005;46:1799–802.
- [5] Saas P, Bonnefoy F, Kury-Paulin S, Kleinclauss F, Perrche S. Mediators involved in the immunomodulatory effects of apoptotic cells. *Transplantation* 2007;84(Suppl. 1):31–4.
- [6] Gneccchi M, Zang Z, Ni A, Dzau VJ. Paracrine mechanisms in adult stem cell signaling and therapy. *Circ Res* 2008;103:1204–19.
- [7] Korf-Klingebiel M, Kempf T, Sauer T, Brinkmann E, Fischer P, Meyer GP, et al. Bone marrow cells are a rich source of growth factors and cytokines: implications for cell therapy trials after myocardial infarction. *Eur Heart J* 2008;29:2851–8.
- [8] Di Santo S, Yang Z, Wyler von Ballmoos M, Voelzmann J, Diehm N, Baumgartner I, et al. Novel cell free strategy for therapeutic angiogenesis: in vitro generated conditioned medium can replace progenitor cell transplantation. *PLoS One* 2009;4:e5643.
- [9] Lichtenauer M, Mildner M, Baumgartner A, Hasun M, Werba G, Beer L, et al. Intravenous and intramyocardial injection of apoptotic white blood cell suspensions prevents ventricular remodeling by increasing elastin expression in cardiac scar tissue after myocardial infarction. *Basic Res Cardiol* 2011;106:645–55.
- [10] Ankersmit HJ, Hoetzenecker K, Dietl W, Soleiman A, Horvat R, Wolfsberger M, et al. Irradiated cultured apoptotic peripheral blood mononuclear cells regenerate infarcted myocardium. *Eur J Clin Invest* 2009;39:445–56.
- [11] Lichtenauer M, Mildner M, Hoetzenecker K, Zimmermann M, Podesser BK, Sipos W, et al. Secretome of apoptotic peripheral blood cells (APOSEC) confers cytoprotection to cardiomyocytes and inhibits tissue remodeling after acute myocardial infarction: a preclinical study. *Basic Res Cardiol* 2011;106:1283–97.
- [12] Hoetzenecker K, Zimmermann M, Hoetzenecker W, Schweiger T, Kollmann D, Mildner M, et al. Mononuclear cell secretome protects from experimental autoimmune myocarditis. *Eur Heart J* 2013 Jan 14. <http://dx.doi.org/10.1093/eurheartj/ehs459>.
- [13] Freyman T, Polin G, Osman H, Crary J, Lu M, Cheng L, et al. A quantitative, randomized study evaluating three methods of mesenchymal stem cell delivery following myocardial infarction. *Eur Heart J* 2006;27:1114–22.
- [14] Dixon JA, Gorman RC, Stroud RE, Bouges S, Hirotsugu H, Gorman 3rd JH, et al. Mesenchymal cell transplantation and myocardial remodeling following myocardial infarction. *Circulation* 2009;120(Suppl. 11):S220–9.
- [15] Cheng Y, Yi G, Conditt GB, Sheehy A, Kolodgie FD, Tellez A, et al. Catheter based endomyocardial delivery of mesenchymal precursor cells using 3D echo guidance improves cardiac function in a chronic myocardial injury ovine model. *Cell Transplant* 2013;22:2299–309.
- [16] Xiang F, Shi Z, Guo X, Qiu Z, Chen X, Huang F, et al. Proteomic analysis of myocardial tissue from the border zone during early stage post-infarct remodeling in rats. *Eur J Heart Fail* 2011;13:254–63.
- [17] Yndestad A, Neurauder CG, Oie E, Forstrøm RJ, Vinge LE, Eide L, et al. Up-regulation of myocardial DNA base excision repair activities in experimental heart failure. *Mutat Res* 2009;666:32–8.
- [18] Gyöngyösi M, Dib N. Diagnostic and prognostic value of 3D NOGA mapping in ischemic heart disease. *Nat Rev Cardiol* 2011;8:393–404.
- [19] Heiberg E, Sjögren J, Ugander M, Carlsson M, Engblom H, Arheden H. Design and validation of segment – a freely available software for cardiovascular image analysis. *BMC Med Imaging* 2010;10:1–13.
- [20] Core team. R: A language and environment for statistical computing. Vienna, Austria: R Foundation for Statistical Computing; 2012. <http://www.R-project.org/>.
- [21] Smyth GK. *limma: Linear Models for Microarray Data*. In: Gentleman R, Carey V, Huber W, Irizarry R, Dudoit S, editors. *Bioinformatics and computational biology solutions using R and bioconductor*. New York: Springer; 2005. pp. 397–420.
- [22] Huang da W, Sherman BT, Lempicki RA. Systematic and integrative analysis of large gene lists using DAVID bioinformatics resources. *Nat Protoc* 2009;4:44–57.
- [23] Ranganath SH, Levy O, Inamdar MS, Karp JM. Harnessing the mesenchymal stem cell secretome for the treatment of cardiovascular disease. *Cell Stem Cell* 2012;10:244–58.
- [24] Ertel A, Tozeren A. Human and mouse switch-like genes share common transcriptional regulatory mechanisms for bimodality. *BMC Genomics* 2008;9:628.
- [25] Jin H, Yang R, Awad TA, Wang F, Li W, Williams SP, et al. Effects of early angiotensin-converting enzyme inhibition on cardiac gene expression after acute myocardial infarction. *Circulation* 2001;103:736–42.
- [26] Sehl PD, Tai JT, Hillan KJ, Brown LA, Goddard A, Yang R, et al. Application of cDNA microarrays in determining molecular phenotype in cardiac growth, development, and response to injury. *Circulation* 2000;101:1990–9.
- [27] Stanton LW, Garrard LJ, Damm D, Garrick BL, Lam A, Kapoun AM, et al. Altered patterns of gene expression in response to myocardial infarction. *Circ Res* 2000;86:939–45.
- [28] Song GY, Wu YJ, Yang YJ, Li JJ, Zhang HL, Pei HJ, et al. The accelerated post-infarction progression of cardiac remodeling is associated with genetic changes in an untreated streptozotocin-induced diabetic rat model. *Eur J Heart Fail* 2009;11:911–21.
- [29] Prat-Vidal C, Gálvez-Montón C, Nonell L, Puigdecant E, Astier L, Solé F, et al. Identification of temporal and region-specific myocardial gene expression patterns in response to infarction in swine. *PLoS One* 2013;8:e54785.
- [30] Roy S, Khanna S, Kuhn DE, Rink C, Williams WT, Zweier JL, et al. Transcriptome analysis of the ischemia-reperfusion remodeling myocardium: temporal changes in inflammation and extracellular matrix. *Physiol Genomics* 2006;25:364–74.
- [31] Jameel MN, Li Q, Mansoor A, Qiang X, Sarver A, Wang X, et al. Long-term functional improvement and gene expression changes after bone marrow-derived multipotent progenitor cell transplantation in myocardial infarction. *Am J Physiol Heart Circ Physiol* 2010;298:H1348–56.

Supplemental Information

Pavo et al.

Long-acting beneficial effect of percutaneously intramyocardially delivered secretome of apoptotic peripheral blood cells on porcine chronic ischemic left ventricular dysfunction

Supplemental Results

Differential gene expression in the infarcted, border zone, and remote myocardium in a chronic failing heart animal model

There were a total of 8,135 genes that showed significantly different expression in the infarct core vs. normal areas; of these, 1,751 (21.5%) genes were identified with the DAVID software, and 1,108 of the genes had known functions. There were a total of 6,020 genes that showed significantly different expression in the infarct core vs. the border zone; of these, 1,356 (22.5%) genes were identified with the DAVID software, and 873 of the genes had known functions. Supplemental Tables 2 and 3 list the functional annotation clusters of genes with significantly different expression in the infarct core vs. the remote myocardium and also in the border zone vs. the infarct core.

Supplemental Figure 1 shows the hierarchical clustering (heat maps) of the up- and downregulated genes in the infarct core vs. the remote myocardium and in the border zone vs. the infarct core. Most of the genes that were downregulated in the infarct core vs. the remote myocardium were clustered into metabolic pathways, such as mitochondrial and oxidative phosphorylation pathways. Other clusters of structural genes were also identified, such as genes involved in membrane-related ion transport pathways and cardiac muscle contraction pathways (ATPase, cytochrome, voltage-dependent calcium-channels, tropomyosin 1, and troponin I). Most of the genes that were upregulated in the infarct core vs. in remote tissue were classified as degradation enzymes, such as proteases or peptidases.

The border zone of infarction differed from the infarct core in that there were several

genes in metabolic clusters that were significantly upregulated (Supplemental Table 3 and Fig. 1), including mitochondrial, structural organelle membrane, and cardiac muscle contraction gene clusters (somewhat similar to the normal myocardium) (Supplemental Fig. 1).

Supplemental Discussion

Genetic alterations in the infarcted myocardium

Although the studies were exploratory, previous analyses of the gene expression profiles of chronically infarcted, reperfused, and remodeled ischemic myocardium identified functional uni- or bimodal genes (24) with known function. The published data, which were mostly from studies conducted in rodent AMI models, are heterogeneous in terms of the number and type of differentially expressed genes.

In a rodent model of chronic AMI without reperfusion, 37 genes showed differential expression compared with the non-affected myocardium of sham-operated rats (25) at 8-weeks FUP. The authors also reported the time-dependent expression of 12 genes post-AMI (26). In contrast, Stanton et al. described 731 cDNA clones with time-dependent, altered expression after partial surgical ligation of the left coronary tree in rats. These clones were classified into several clusters, including cell signaling, protein expression, gene expression, metabolism, cell/organism defense, cell division, and structure and motility clusters (27). In diabetic rats, chronic coronary occlusion resulted in the upregulation of 770 genes and the downregulation of 451 genes compared with non-diabetic rats with the same coronary procedure; unfortunately, the report did not mention the level of significance for the differentially expressed genes (28). In pigs, chronic surgical coronary occlusion of the left circumflex coronary artery resulted in the identification of more than 1000 genes that showed time-dependent differential expression. These genes were classified into several clusters and canonical pathways, such as cardiogenesis and apoptosis (29).

Compared with sham-operated rats, reperfusion after 30-min occlusion of the LAD induced the expression of 119 and 590 genes 2- and 7-days post-ischemia/reperfusion, respectively, and downregulated the expression of 38 and 286 genes, respectively, at 5% FDR (30). Hierarchical cluster images represented 3 major categories: extracellular matrix, apoptosis, and inflammation.

In our study, chronic ischemic LV dysfunction in pigs was induced using catheter-based, reperfused AMI, which mimics primary percutaneous coronary intervention in human AMI. This led to the differential expression of 1,108 genes in the infarcted vs. the remote myocardium and also to the identification of 873 genes with differential expression in the border zone vs. the infarcted core. To our knowledge, this is the first report of gene expression profiling of closed-chest reperfused AMI that describes the molecular biological changes between remote and infarcted myocardium and the border zone of infarction. The differences in gene expression profiles between the infarct core and the border areas were associated with metabolic gene clusters, structural organelle membrane genes, and cardiac muscle contraction genes, thus confirming the survival potential of cells in this ischemic infarct-adjacent area.

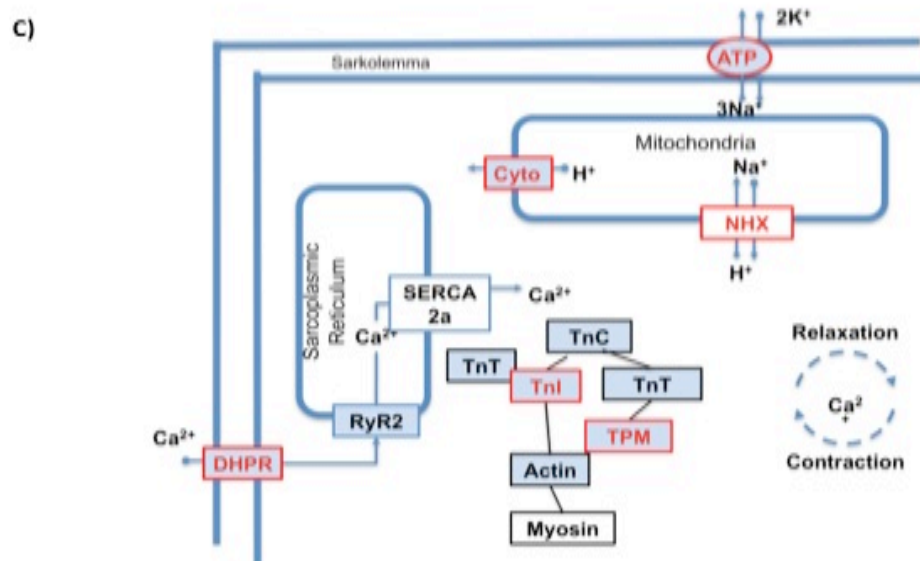
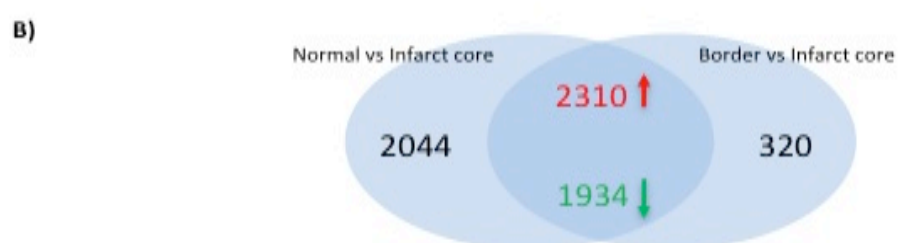
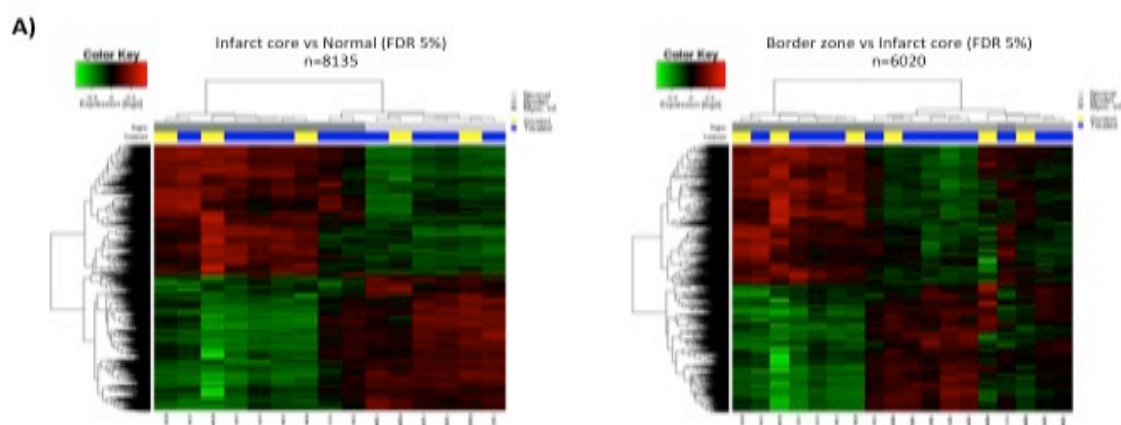
Interestingly, we found several genes that were overexpressed in the infarct core (“dead” cells) compared with cells in the remote healthy area. This highlights the ongoing endogenous regenerative potential of apoptotic/necrotic cells to restore living cell morphology and function.

Supplemental Figure

Gene expression differences between infarct core and border zone in chronic ischemic left ventricular dysfunction

- A. Functional annotation hierarchical clustering of the genes (heat maps) upregulated (red) and downregulated (green) in the infarct core compared to remote myocardium (left) and in the border zone compared to infarct core (right). Columns represent different samples from the remote myocardium, border zone and myocardial infarction, while rows represent different genes. Scaled and centered \log_2 -expression values are displayed in green and red according to the color scale on the top.
- B. Venn diagram illustrates the number of common (intersection of circles) or unique identified genes in the comparisons of normal (N) vs. infarcted and border zone (B) vs. infarcted areas. All common genes are similarly up- (red) or downregulated (green) in the infarcted myocardium.
- C. Canonical pathway of the muscle contraction genes significantly upregulated (red) in the border zone of infarction as compared to infarct core. TnI: troponin I; TPM: tropomyosin; Cyto: Cytochrome b and c; NHX: Na⁺/H⁺ antiporter; DHPR: dihydropyridine receptor gene; ATP: ATPase Na⁺/K⁺ transporting genes

Supplemental Figure



Supplemental Tables

Supplemental Table 1. Primer list of the rtPCR

Gene	Name	Accession number	Forward sequence (5'-3')	Reverse sequence (5'-3')	Amplicon [bp]	E [%]
HPRT1	Hypoxanthine phosphoribosyltransferase 1	NM_001032376.2	CCC AGC GTC GTG ATT AGT GA	ATC TCG AGC AAG CCG TTC AG	131	89
PPIA	Peptidylprolyl isomerase A (cyclophilin A)	NM_214353.1	GTC TTC TTC GAC ATC GCC GT	TCC TTT CTC CCC AGT GCT CA	120	95
GAPDH	Glyceraldehyde-3-phosphate dehydrogenase	NM_001206359.1	TCC ACC CAC GGC AAG TTC CAC	ATG TTG GCG GGA TCT CGC TCC T	104	109
HIF1alpha	Hypoxia inducible factor 1, alpha subunit	NM_001123124.1	ACC TGA GCC TAA CAG TCC CAG TG	TTC TTT GCC TCT GTG TCT TCA GCA A	114	88
MMP9	Matrix metalloproteinase 9	NM_001038004.1	CGG GAG ACC TAC GAA CCA AT	TTT CTG TCG GTC ATC TCG GC	97	108
CASP3	Caspase 3, apoptosis-related cysteine peptidase	NM_214131.1	GGG ATT GAG ACG GAC AGT GG	TGA ACC AGG ATC CGT CCT TTG	136	95
CxCl12	Chemokine (C-X-C motif) ligand 12	NM_001009580.1	GTG GCA CGG CTG AAG AGC AAC	GGC CCG AGA GAG TGG GAC TGG	112	91
MEF2C	Myocyte enhancer factor 2C	NM_001044540.1	TAA CAT GCC GCC ATC CGC CC	ATC CTC TCG GTC GCT GCC GT	151	97
MYOG	Myogenin (myogenic factor 4)	NM_001012406.1	GCC AGG GGT GCC CAG TGA ATG	ATG ATC CCC TGG GTT GGG GC	94	121
GATA4	GATA binding protein 4	NM_214293.1	AGA AAA CGG AAG CCC AAG AAC	CCA CAC TGC TGG AGT TGC TG	109	95
TGFBR3	Transforming growth factor, beta receptor III	NM_214272.1	ATG GAC CTC TAC ACC ACG GA	CGA GTA CGG GGA GAT GAA GC	153	95

Supplemental Table 2. Up and downregulated gene clusters in the infarct core compared to remote myocardium

Upregulated gene clusters in infarct core vs remote myocardium				
Cluster 1		Enrichment Score: 7,02		
Term	Count	%	Fold Enrichment	Bonferroni
ssc03010:Ribosome	28	3.37	4.08	3.11E-10
ribosomal protein	25	3.00	3.40	7.92E-07
GO:0003735~structural constituent of ribosome	25	3.00	3.17	5.56E-06
GO:0005840~ribosome	25	3.00	2.98	9.37E-06
GO:0006412~translation	26	3.13	2.87	6.61E-05
ribonucleoprotein	23	2.76	3.12	3.69E-05
GO:0005198~structural molecule activity	35	4.21	2.25	3.38E-04
GO:0030529~ribonucleoprotein complex	25	3.00	2.55	4.91E-04
GO:0043232~intracellular non-membrane-bounded organelle	47	5.65	1.74	4.78E-03
GO:0043228~non-membrane-bounded organelle	47	5.65	1.74	4.78E-03
Cluster 2		Enrichment Score: 2.73		
Term	Count	%	Fold Enrichment	Bonferroni
IPR016060:Complement control module	11	1.32	3.59	1.06E-01
Cluster 3		Enrichment Score: 2.72		
Term	Count	%	Fold Enrichment	Bonferroni
GO:0004197~cysteine-type endopeptidase activity	13	1.56	3.88	2.53E-03

GO:0008234~cysteine-type peptidase activity	14	1.68	3.23	1.77E-02
---	----	------	------	----------

Cluster 4 **Enrichment Score: 2.16**

Term	Count	%	Fold Enrichment	Bonferroni
ssc04142:Lysosome	22	2.64	2.64	2.51E-03
thiol protease	12	1.44	3.26	6.40E-02

Cluster 5 **Enrichment Score: 2.03**

Term	Count	%	Fold Enrichment	Bonferroni
ssc04514:Cell adhesion molecules (CAMs)	26	3.13	2.49	1.18E-03
ssc05416:Viral myocarditis	19	2.28	2.64	1.15E-02
ssc04672:Intestinal immune network for IgA production	16	1.92	2.80	2.48E-02

DOWNregulated genes in infarct core vs remote myocardium

Cluster 1 **Enrichment Score: 13.6**

Term	Count	%	Fold Enrichment	Bonferroni
GO:0005739~mitochondrion	64	6.91	3.95	1.90E-27
mitochondrion	55	5.94	3.69	6.37E-20
transit peptide	27	2.92	3.85	5.51E-09
transit peptide:Mitochondrion	27	2.92	3.47	8.37E-08
GO:0031980~mitochondrial lumen	13	1.40	4.05	1.06E-03
GO:0005759~mitochondrial matrix	13	1.40	4.05	1.06E-03

Cluster 2**Enrichment Score: 12.22**

Term	Count	%	Fold Enrichment	Bonferroni
GO:0005739~mitochondrion	64	6.91	3.95	1.90E-27
GO:0044429~mitochondrial part	45	4.86	4.37	8.30E-21
mitochondrion	55	5.94	3.69	6.37E-20
ssc00190:Oxidative phosphorylation	39	4.21	4.22	8.97E-16
GO:0005740~mitochondrial envelope	33	3.56	4.55	3.10E-15
ssc05012:Parkinson's disease	40	4.32	3.98	5.90E-15
GO:0031966~mitochondrial membrane	31	3.35	4.59	1.88E-14
GO:0031975~envelope	35	3.78	3.91	4.32E-13
GO:0031967~organelle envelope	35	3.78	3.91	4.32E-13
GO:0031090~organelle membrane	41	4.43	3.20	1.57E-11
GO:0019866~organelle inner membrane	23	2.48	5.05	2.06E-11
GO:0005743~mitochondrial inner membrane	23	2.48	5.05	2.06E-11
ssc05016:Huntington's disease	36	3.89	3.18	3.33E-09
mitochondrion inner membrane	17	1.84	4.62	1.48E-06
ssc05010:Alzheimer's disease	34	3.67	2.66	4.08E-06
GO:0015077~monovalent inorganic cation transmembrane transporter activity	17	1.84	3.55	4.74E-04
GO:0015078~hydrogen ion transmembrane transporter activity	16	1.73	3.47	1.66E-03
GO:0022890~inorganic cation transmembrane transporter activity	18	1.94	3.05	3.58E-03

Cluster 3**Enrichment Score: 7.13**

Term	Count	%	Fold Enrichment	Bonferroni
------	-------	---	-----------------	------------

GO:0006091~generation of precursor metabolites and energy	37	4.00	3.64	6.74E-12
GO:0015980~energy derivation by oxidation of organic compounds	18	1.94	4.27	6.51E-06
GO:0045333~cellular respiration	17	1.84	4.21	2.79E-05
GO:0022900~electron transport chain	16	1.73	3.26	9.28E-03
GO:0055114~oxidation reduction	44	4.75	1.80	2.13E-02
electron transport	13	1.40	3.22	4.36E-02

Cluster 4 **Enrichment Score: 4.89**

Term	Count	%	Fold Enrichment	Bonferroni
ssc04260:Cardiac muscle contraction	20	2.16	3.58	2.30E-05
GO:0015077~monovalent inorganic cation transmembrane transporter activity	17	1.84	3.55	4.74E-04
GO:0015078~hydrogen ion transmembrane transporter activity	16	1.73	3.47	1.66E-03
GO:0022890~inorganic cation transmembrane transporter activity	18	1.94	3.05	3.58E-03

Cluster 5 **Enrichment Score: 4.17**

Term	Count	%	Fold Enrichment	Bonferroni
GO:0031980~mitochondrial lumen	13	1.40	4.05	1.06E-03
GO:0005759~mitochondrial matrix	13	1.40	4.05	1.06E-03
GO:0031974~membrane-enclosed lumen	18	1.94	2.54	2.94E-02

Cluster 6 **Enrichment Score: 3.86**

Term	Count	%	Fold Enrichment	Bonferroni
------	-------	---	-----------------	------------

GO:0015980~energy derivation by oxidation of organic compounds	18	1.94	4.27	6.51E-06
GO:0045333~cellular respiration	17	1.84	4.21	2.79E-05
ssc00020:Citrate cycle (TCA cycle)	12	1.30	4.43	1.12E-03

Cluster 7**Enrichment Score: 3.55**

Term	Count	%	Fold Enrichment	Bonferroni
GO:0070469~respiratory chain	12	1.30	5.08	9.07E-05
GO:0006119~oxidative phosphorylation	13	1.40	4.36	1.28E-03
oxidative phosphorylation	11	1.19	4.48	3.76E-03
respiratory chain	11	1.19	4.48	3.76E-03
GO:0022900~electron transport chain	16	1.73	3.26	9.28E-03
membrane-associated complex	10	1.08	4.07	3.69E-02
electron transport	13	1.40	3.22	4.36E-02

Cluster 8**Enrichment Score: 2.68**

Term	Count	%	Fold Enrichment	Bonferroni
GO:0046034~ATP metabolic process	13	1.40	4.36	1.28E-03
GO:0006754~ATP biosynthetic process	13	1.40	4.36	1.28E-03
GO:0022890~inorganic cation transmembrane transporter activity	18	1.94	3.05	3.58E-03
GO:0009141~nucleoside triphosphate metabolic process	13	1.40	3.90	7.43E-03
GO:0009142~nucleoside triphosphate biosynthetic process	13	1.40	3.90	7.43E-03
GO:0009144~purine nucleoside triphosphate metabolic process	13	1.40	3.90	7.43E-03

GO:0009145~purine nucleoside triphosphate biosynthetic process	13	1.40	3.90	7.43E-03
GO:0009205~purine ribonucleoside triphosphate metabolic process	13	1.40	3.90	7.43E-03
GO:0009201~ribonucleoside triphosphate biosynthetic process	13	1.40	3.90	7.43E-03
GO:0009206~purine ribonucleoside triphosphate biosynthetic process	13	1.40	3.90	7.43E-03
GO:0009199~ribonucleoside triphosphate metabolic process	13	1.40	3.90	7.43E-03

Enrichment score:	Geometric mean (in 2log scale) of the nominal p-values (not shown) for each GO category in a cluster.
Count:	Number of categories genes
%	Percentage of GO category genes
Fold enrichment:	Fold Enrichment of genes in the blue modules compared to a background list.
P value:	Bonferroni corrected P-value for the enrichment of each GO category

Supplemental Table 3. Up and downregulated gene clusters in the border zone compared to infarct core

Upregulated genes clusters in border zone				
Cluster 1	Enrichment Score: 13.66			
Term	Count	%	Fold Enrichment	Bonferroni
GO:0005739~mitochondrion	60	9.22	4.82	1.16E-30
GO:0044429~mitochondrial part	43	6.61	5.44	1.26E-23
mitochondrion	51	7.83	4.50	5.14E-22
ssc00190:Oxidative phosphorylation	40	6.14	5.85	5.31E-22
ssc05012:Parkinson's disease	39	5.99	5.25	7.04E-19
GO:0005740~mitochondrial envelope	31	4.76	5.56	1.92E-16
GO:0031966~mitochondrial membrane	29	4.45	5.59	2.78E-15
GO:0031967~organelle envelope	33	5.07	4.80	7.82E-15
GO:0031975~envelope	33	5.07	4.80	7.82E-15
ssc05016:Huntington's disease	36	5.53	4.30	1.87E-13
GO:0005743~mitochondrial inner membrane	22	3.38	6.28	1.40E-12
GO:0019866~organelle inner membrane	22	3.38	6.28	1.40E-12
GO:0031090~organelle membrane	37	5.68	3.75	2.68E-12
ssc05010:Alzheimer's disease	33	5.07	3.50	4.70E-09
mitochondrion inner membrane	16	2.46	5.71	3.46E-07
ssc04260:Cardiac muscle contraction	18	2.76	4.36	8.15E-06
GO:0015078~hydrogen ion transmembrane transporter activity	16	2.46	4.50	4.12E-05
GO:0015077~monovalent inorganic cation transmembrane transporter activity	16	2.46	4.33	8.52E-05

GO:0022890~inorganic cation transmembrane transporter activity	17	2.61	3.74	4.53E-04
GO:0004129~cytochrome-c oxidase activity	9	1.38	5.76	6.38E-03
GO:0016676~oxidoreductase activity, acting on heme group of donors, oxygen as acceptor	9	1.38	5.76	6.38E-03
GO:0016675~oxidoreductase activity, acting on heme group of donors	9	1.38	5.76	6.38E-03
GO:0015002~heme-copper terminal oxidase activity	9	1.38	5.76	6.38E-03
Cluster 2	Enrichment Score: 9.21			
Term	Count	%	Fold Enrichment	Bonferroni
GO:0006091~generation of precursor metabolites and energy	36	5.53	4.76	1.59E-15
GO:0015980~energy derivation by oxidation of organic compounds	18	2.76	5.75	3.68E-08
GO:0045333~cellular respiration	17	2.61	5.66	2.17E-07
GO:0022900~electron transport chain	16	2.46	4.38	1.33E-04
GO:0055114~oxidation reduction	40	6.14	2.20	2.32E-04
electron transport	13	2.00	4.24	2.29E-03
Cluster 3	Enrichment Score: 7.13			
Term	Count	%	Fold Enrichment	Bonferroni
transit peptide	25	3.84	4.68	7.86E-10
transit peptide:Mitochondrion	25	3.84	4.08	1.95E-08
GO:0031980~mitochondrial lumen	13	2.00	5.28	5.06E-05
GO:0005759~mitochondrial matrix	13	2.00	5.28	5.06E-05
GO:0031974~membrane-enclosed lumen	18	2.76	3.30	7.33E-04
GO:0070013~intracellular organelle	17	2.61	3.20	2.51E-03

lumen				
GO:0043233~organelle lumen	17	2.61	3.20	2.51E-03
Cluster 4	Enrichment Score: 4.85			
Term	Count	%	Fold Enrichment	Bonferroni
GO:0015980~energy derivation by oxidation of organic compounds	18	2.76	5.75	3.68E-08
GO:0045333~cellular respiration	17	2.61	5.66	2.17E-07
ssc00020:Citrate cycle (TCA cycle)	11	1.69	5.49	5.39E-04
GO:0006732~coenzyme metabolic process	12	1.84	4.60	4.36E-03
GO:0009060~aerobic respiration	9	1.38	5.75	1.22E-02
GO:0051186~cofactor metabolic process	12	1.84	4.18	1.44E-02
Cluster 5	Enrichment Score: 4.24			
Term	Count	%	Fold Enrichment	Bonferroni
GO:0070469~respiratory chain	12	1.84	6.61	4.84E-06
GO:0022900~electron transport chain	16	2.46	4.38	1.33E-04
respiratory chain	11	1.69	5.89	2.49E-04
oxidative phosphorylation	11	1.69	5.89	2.49E-04
electron transport	13	2.00	4.24	2.29E-03
membrane-associated complex	10	1.54	5.35	3.44E-03
GO:0016655~oxidoreductase activity, acting on NADH or NADPH, quinone or similar compound as acceptor	8	1.23	6.25	1.15E-02
nad	13	2.00	3.61	1.78E-02
ubiquinone	7	1.08	6.56	3.19E-02
Cluster 6	Enrichment Score: 3.44			

Term	Count	%	Fold Enrichment	Bonferroni
GO:0006119~oxidative phosphorylation	13	2.00	5.86	3.19E-05
Cluster 7	Enrichment Score: 2.64			
Term	Count	%	Fold Enrichment	Bonferroni
GO:0046034~ATP metabolic process	11	1.69	4.96	5.20E-03
GO:0006754~ATP biosynthetic process	11	1.69	4.96	5.20E-03
GO:0045259~proton-transporting ATP synthase complex	7	1.08	7.71	4.19E-03
Downregulated genes in Border vs AMI				
Cluster 1	Enrichment Score: 2.64			
Term	Count	%	Fold Enrichment	Bonferroni
GO:0005578~proteinaceous extracellular matrix	18	2.55	2.67	1.37E-02
GO:0031012~extracellular matrix	18	2.55	2.60	2.01E-02
Cluster 2	Enrichment Score: 2.34			
Term	Count	%	Fold Enrichment	Bonferroni
GO:0004197~cysteine-type endopeptidase activity	11	1.56	3.92	2.94E-02
ssc04142:Lysosome	19	2.70	2.67	1.30E-02
Cluster 3	Enrichment Score: 2.32			
Term	Count	%	Fold Enrichment	Bonferroni
ssc04514:Cell adhesion molecules (CAMs)	22	3.12	2.46	1.14E-02
ssc04672:Intestinal immune network for IgA production	15	2.13	3.07	1.75E-02

ssc05416:Viral myocarditis	17	2.41	2.77	2.17E-02
Cluster 4	Enrichment Score: 2.3			
Term	Count	%	Fold Enrichment	Bonferroni
signal peptide	86	12.20	1.40	3.29E-02

Enrichment score: Geometric mean (in 2log scale) of the nominal p-values (not shown) for each GO category in a cluster.

Count: Number of categories genes

% Percentage of GO category genes

Fold enrichment: Fold Enrichment of genes in the blue modules compared to a background list.

P value: Bonferroni corrected P-value for the enrichment of each GO category

5. DISCUSSION

First, our data show that NOGA®-derived electroanatomical mapping system is an precise method to navigate well-directed intramyocardial therapy, which makes the NOGA® orientation suitable for intramyocardial reparative substance delivery. Concerning the magnitude of the transmural and non-transmural scarred tissues and myocardial regions with preserved and diminished viability, the findings of NOGA® were similar to those of cMRI-LE. However, the accurateness of the NOGA® images relies essentially on the quantity and quality of the measured points used to create the 3D map. Troubles in reaching some areas with the mapping catheter due to anatomical structures within the left ventricular cavity such as the papillary muscles or episodes of ventricular tachyarrhythmias by way of touching susceptible ischemic areas could lead to unsatisfactory sampling and imperfect mapping.

Intramyocardial injections of regenerative substances target the non-transmural infarcted area or territories with diminished viability, or viable myocardium with reduced segmental wall motion of the LV. Considering our data, both the unipolar and bipolar voltage maps revealed broader zones of interest than cMRI, with an over-assessment of the infarct size by just 2.82% of the complete LV endocardial surface in unipolar voltage mapping, and by 6.82% of the LV by bipolar mapping. These estimates seem acceptable for performing safe and accurate ando-or intramyocardial procedures, considering that there is no general agreement on definitions and cut-off values of viability and transmurality in the related literature, neither for cMRI nor for NOGA® imaging. Also, regenerative material or cells transferred into the region neighboring the non-transmural infarction hold a worthy chance of being retained, remaining functional, and migrating to or even inside the ischemia affected zone, so that in sum a broader area might be exposed for an effective and simultaneously safe therapy.

The extent of unhealthy myocardial regions correlated well between the unipolar and bipolar polar mapping images. Nevertheless, the extent of the myocardial infarction and the border area derived from unipolar maps was systematically higher than the extent of the transmural and non-transmural areas measured on the bipolar maps. Since the core infarction area may include both transmural and non-transmural necrotic myocardial regions, the infarct core and the border area (i.e. extension of infarction) do not automatically correspond to the transmural and non-transmural ischemia (i.e. the infarction severity), which could explain our observations.

Second, we showed that 3D NOGA-navigated injection of the novel regenerative therapy APOSEC is definitively safe as well as feasible and effective. Intramyocardial therapy of APOSEC was related to an increased density of capillaries and the homing of endogenous stem cells of the c-kit+ type in the infarcted area and the neighboring zone of infarction,

associated with a decrease of infarction size, and an enhancement of LV contractile function. Parallel to these clinical relevant observations transcriptomics analysis revealed a downregulation of genes involved in inflammatory and apoptotic pathways of the APOSEC-treated heart tissue regions. The confirmation of altered gene expression by rtPCR indicated enhanced expression levels of *Mefc2* and a strong downregulation of caspase-3, an apoptosis regulator.

In previous experiments we reported, that analogously to the secretome of MSCs,¹⁶⁸ APOSEC contains anti-apoptotic and reparative substances that are able to promote myocardial angiogenesis and repair.^{155,157} Regenerative cells used for cell-based therapies that are supplied to the area of ischemia similarly generate various signaling molecules, for example matrix proteins and anti-inflammatory and angiogenic factors. Nevertheless, the response of the host myocardial tissue remains the crucial contributing factor for the attempt of regenerating the ischemia-attacked myocardial tissue. Therefore we aimed to investigate transcriptomics changes of the host myocardial tissue (i.e. ischemically injured myocardial cells) following direct interaction with the intramyocardially delivered paracrine factors (APOSEC). APOSEC was competent to induce durable transcriptomic alterations. It is critical to note, that roughly 50% of the significantly downregulated genes, and none of the significantly upregulated genes, are presently linked to known functions. The pathways involving these genes could belong to metabolic, angiogenic, or myogenic functional clusters that trigger synergistic reparative processes as proven by infarct size reduction and the prevention of ventricular remodeling.

To the best of our knowledge, this report is the first describing transcriptomic analyses in closed-chest MI with reperfusion and also the first report to portray molecular biological alterations in remote and infarcted myocardial tissue and in the neighboring zone of infarction. Our model led to the differential expression of 1,108 genes in the infarcted vs. the remote myocardium and also to the identification of 873 genes with differential expression in the border zone vs. the infarcted core. Until now, published data derive mostly from rodent MI models, with heterogeneous results regarding the number and type of differentially-expressed genes. The analyses of remodeled ischemic myocardium after reperfused myocardial infarction identified functional unimodal or bimodal genes with recognized functions.¹⁶⁹⁻¹⁷⁵ Surgical ligation of the first or second diagonal vessels of LAD of mini-swine and immediate injection of 50×10^6 bone marrow-originated multipotent progenitor cells led to a distinct enhancement in EF (51.2% vs. 35.7%) and in a reduction of size of infarction (4.6% vs. 8.6%) 4-month after cell-procedure in verum vs. placebo groups, respectively, yet without engraftment of the cells.¹⁷⁶ Transcriptomics analysis showed 11 upregulated and 41 downregulated genes in the cell injection group, with downregulation of inflammatory

pathways, which the authors attributed to paracrine effect of the delivered cells; which data underline and also confirm the importance of the cell-free therapy.

5.1. Limitations

While there are ongoing labors to use 3D fusion software to bring together information from both 3D NOGA endocardial maps and cardiac MRIs, we overlaid the two images due to lack of commercially accessible 3D MRI-NOGA software with fusion of the two images. Furthermore we refrained from using the maps of the local linear shortening of the NOGA® for allocation of the hibernating myocardium, which is can be distinguished by preserved viability but reduced segmental wall motion,¹⁷⁷ because of the lower precision of the method and the reported discrepancies with cMRI regarding abnormalities in segmental wall motion.¹⁶⁵ Also, the usage of 2SD method of cMRI-LE might overrate the infarct size compared to the 5SD or “full width at half maximum” (FWHM) method. In our experience, the 5SD analysis method is not superior in identifying the infarct size compared to the 2SD approach, and there are reports that indicate a higher coefficient of correlation for the 2SD method than the 5SD analysis.¹⁷⁸

In the APOSEC study, locally performed intramyocardial injections of medium solution in the control animals group, might affect gene expression compared to the placebo-treated infarcted animals, which doesn't allow an exact comparison of our “medium-solution-treated” placebo control group with literature data in similar experiments. Moreover, myocardial samples at day 60 were obtained through macroscopic identification of the injection site, a procedure that is crucial to obtain valuable information. Technically, the localization of the previously occluded LAD segment close to the origin of the second diagonal vessel and identification of the border of the infarcted area turned out to be feasible. Correct sampling was also underlined by confirmed differential gene expression of these samples.

5.2. Conclusions

NOGA mapping displayed a good congruency with the gold standard off-line method, namely the cMRI-LE imaging. The NOGA® system could be profitable in patients in whom cMRI is contraindicated and who need guided intramyocardial reparative therapy. 3D guided injections of APOSEC with NOVA navigation proved to be safe, as well as feasible and effective. APOSEC reduced the ventricular remodeling attributed to chronic myocardial ischemia in a large animal model, that is clinically relevant. Particularly, APOSEC stimulated long-lasting alterations in gene expression profiles that resulted in silencing of genes involved in inflammation and apoptosis. Transcriptomics analysis identifies genes that might represent novel targets for anti-remodeling as well as anti-ischemic therapy.

6. REFERENCES

1. Pavo N, Charwat S, Nyolczas N, et al. Cell therapy for human ischemic heart diseases: critical review and summary of the clinical experiences. *Journal of molecular and cellular cardiology* 2014;75:12-24.
2. Dargie H. Heart failure post-myocardial infarction: a review of the issues. *Heart* 2005;91 Suppl 2:ii3-6; discussion ii31, ii43-8.
3. Beltrami AP, Barlucchi L, Torella D, et al. Adult cardiac stem cells are multipotent and support myocardial regeneration. *Cell* 2003;114:763-76.
4. Chiu RC, Zibaitis A, Kao RL. Cellular cardiomyoplasty: myocardial regeneration with satellite cell implantation. *The Annals of thoracic surgery* 1995;60:12-8.
5. Quaini F, Urbanek K, Beltrami AP, et al. Chimerism of the transplanted heart. *The New England journal of medicine* 2002;346:5-15.
6. Laflamme MA, Myerson D, Saffitz JE, Murry CE. Evidence for cardiomyocyte repopulation by extracardiac progenitors in transplanted human hearts. *Circulation research* 2002;90:634-40.
7. Frangogiannis NG, Mendoza LH, Ren G, et al. MCSF expression is induced in healing myocardial infarcts and may regulate monocyte and endothelial cell phenotype. *American journal of physiology Heart and circulatory physiology* 2003;285:H483-92.
8. Kajstura J, Leri A, Finato N, Di Loreto C, Beltrami CA, Anversa P. Myocyte proliferation in end-stage cardiac failure in humans. *Proceedings of the National Academy of Sciences of the United States of America* 1998;95:8801-5.
9. Beltrami AP, Urbanek K, Kajstura J, et al. Evidence that human cardiac myocytes divide after myocardial infarction. *The New England journal of medicine* 2001;344:1750-7.
10. Bergmann O, Bhardwaj RD, Bernard S, et al. Evidence for cardiomyocyte renewal in humans. *Science* 2009;324:98-102.
11. Pouzet B, Vilquin JT, Hagege AA, et al. Intramyocardial transplantation of autologous myoblasts: can tissue processing be optimized? *Circulation* 2000;102:III210-5.
12. Smits PC, van Geuns RJ, Poldermans D, et al. Catheter-based intramyocardial injection of autologous skeletal myoblasts as a primary treatment of ischemic heart failure: clinical experience with six-month follow-up. *Journal of the American College of Cardiology* 2003;42:2063-9.
13. Dib N, Diethrich EB, Campbell A, et al. Endoventricular transplantation of allogenic skeletal myoblasts in a porcine model of myocardial infarction. *Journal of endovascular therapy : an official journal of the International Society of Endovascular Specialists* 2002;9:313-9.
14. Menasche P. Stem cell therapy for heart failure: are arrhythmias a real safety concern? *Circulation* 2009;119:2735-40.
15. Orlic D, Kajstura J, Chimenti S, et al. Mobilized bone marrow cells repair the infarcted heart, improving function and survival. *Proceedings of the National Academy of Sciences of the United States of America* 2001;98:10344-9.
16. Orlic D, Kajstura J, Chimenti S, et al. Bone marrow cells regenerate infarcted myocardium. *Nature* 2001;410:701-5.
17. Orlic D, Hill JM, Arai AE. Stem cells for myocardial regeneration. *Circulation research* 2002;91:1092-102.
18. Kocher AA, Schuster MD, Szabolcs MJ, et al. Neovascularization of ischemic myocardium by human bone-marrow-derived angioblasts prevents cardiomyocyte apoptosis, reduces remodeling and improves cardiac function. *Nature medicine* 2001;7:430-6.
19. Luth ES, Jun SJ, Wessen MK, Liadaki K, Gussoni E, Kunkel LM. Bone marrow side population cells are enriched for progenitors capable of myogenic differentiation. *Journal of cell science* 2008;121:1426-34.
20. Urbich C, Heeschen C, Aicher A, Dernbach E, Zeiher AM, Dimmeler S. Relevance of monocytic features for neovascularization capacity of circulating endothelial progenitor cells. *Circulation* 2003;108:2511-6.

21. Badorff C, Brandes RP, Popp R, et al. Transdifferentiation of blood-derived human adult endothelial progenitor cells into functionally active cardiomyocytes. *Circulation* 2003;107:1024-32.
22. Strauer BE, Brehm M, Zeus T, et al. Repair of infarcted myocardium by autologous intracoronary mononuclear bone marrow cell transplantation in humans. *Circulation* 2002;106:1913-8.
23. Assmus B, Schachinger V, Teupe C, et al. Transplantation of Progenitor Cells and Regeneration Enhancement in Acute Myocardial Infarction (TOPCARE-AMI). *Circulation* 2002;106:3009-17.
24. Gu X, Xie Y, Gu J, et al. Repeated intracoronary infusion of peripheral blood stem cells with G-CSF in patients with refractory ischemic heart failure--a pilot study. *Circulation journal : official journal of the Japanese Circulation Society* 2011;75:955-63.
25. Li ZQ, Zhang M, Jing YZ, et al. The clinical study of autologous peripheral blood stem cell transplantation by intracoronary infusion in patients with acute myocardial infarction (AMI). *International journal of cardiology* 2007;115:52-6.
26. Kang HJ, Kim HS, Zhang SY, et al. Effects of intracoronary infusion of peripheral blood stem-cells mobilised with granulocyte-colony stimulating factor on left ventricular systolic function and restenosis after coronary stenting in myocardial infarction: the MAGIC cell randomised clinical trial. *Lancet* 2004;363:751-6.
27. Kang HJ, Lee HY, Na SH, et al. Differential effect of intracoronary infusion of mobilized peripheral blood stem cells by granulocyte colony-stimulating factor on left ventricular function and remodeling in patients with acute myocardial infarction versus old myocardial infarction: the MAGIC Cell-3-DES randomized, controlled trial. *Circulation* 2006;114:1145-51.
28. Schachinger V, Assmus B, Britten MB, et al. Transplantation of progenitor cells and regeneration enhancement in acute myocardial infarction: final one-year results of the TOPCARE-AMI Trial. *Journal of the American College of Cardiology* 2004;44:1690-9.
29. Bartunek J, Vanderheyden M, Vandekerckhove B, et al. Intracoronary injection of CD133-positive enriched bone marrow progenitor cells promotes cardiac recovery after recent myocardial infarction: feasibility and safety. *Circulation* 2005;112:1178-83.
30. Assmus B, Honold J, Schachinger V, et al. Transcoronary transplantation of progenitor cells after myocardial infarction. *The New England journal of medicine* 2006;355:1222-32.
31. Assmus B, Fischer-Rasokat U, Honold J, et al. Transcoronary transplantation of functionally competent BMCs is associated with a decrease in natriuretic peptide serum levels and improved survival of patients with chronic postinfarction heart failure: results of the TOPCARE-CHD Registry. *Circulation research* 2007;100:1234-41.
32. Tendera M, Wojakowski W, Ruzylo W, et al. Intracoronary infusion of bone marrow-derived selected CD34+CXCR4+ cells and non-selected mononuclear cells in patients with acute STEMI and reduced left ventricular ejection fraction: results of randomized, multicentre Myocardial Regeneration by Intracoronary Infusion of Selected Population of Stem Cells in Acute Myocardial Infarction (REGENT) Trial. *European heart journal* 2009;30:1313-21.
33. Quyyumi AA, Waller EK, Murrow J, et al. CD34(+) cell infusion after ST elevation myocardial infarction is associated with improved perfusion and is dose dependent. *American heart journal* 2011;161:98-105.
34. Povsic TJ, Junge C, Nada A, et al. A phase 3, randomized, double-blinded, active-controlled, unblinded standard of care study assessing the efficacy and safety of intramyocardial autologous CD34+ cell administration in patients with refractory angina: design of the RENEW study. *American heart journal* 2013;165:854-61 e2.
35. Rehman J. Bone marrow tinctures for cardiovascular disease: lost in translation. *Circulation* 2013;127:1935-7.
36. Makino S, Fukuda K, Miyoshi S, et al. Cardiomyocytes can be generated from marrow stromal cells in vitro. *The Journal of clinical investigation* 1999;103:697-705.
37. !!! INVALID CITATION !!! 37.
38. Lee JW, Lee SH, Youn YJ, et al. A randomized, open-label, multicenter trial for the safety and efficacy of adult mesenchymal stem cells after acute myocardial infarction. *Journal of Korean medical science* 2014;29:23-31.

39. Heldman AW, DiFede DL, Fishman JE, et al. Transendocardial mesenchymal stem cells and mononuclear bone marrow cells for ischemic cardiomyopathy: the TAC-HFT randomized trial. *Jama* 2014;311:62-73.
40. Hare JM, Traverse JH, Henry TD, et al. A randomized, double-blind, placebo-controlled, dose-escalation study of intravenous adult human mesenchymal stem cells (prochymal) after acute myocardial infarction. *Journal of the American College of Cardiology* 2009;54:2277-86.
41. Hare JM, Fishman JE, Gerstenblith G, et al. Comparison of allogeneic vs autologous bone marrow-derived mesenchymal stem cells delivered by transendocardial injection in patients with ischemic cardiomyopathy: the POSEIDON randomized trial. *Jama* 2012;308:2369-79.
42. Hosoda T, Rota M, Kajstura J, Leri A, Anversa P. Role of stem cells in cardiovascular biology. *Journal of thrombosis and haemostasis : JTH* 2011;9 Suppl 1:151-61.
43. Huang NF, Li S. Mesenchymal stem cells for vascular regeneration. *Regenerative medicine* 2008;3:877-92.
44. Okura H, Matsuyama A, Lee CM, et al. Cardiomyoblast-like cells differentiated from human adipose tissue-derived mesenchymal stem cells improve left ventricular dysfunction and survival in a rat myocardial infarction model. *Tissue engineering Part C, Methods* 2010;16:417-25.
45. Houtgraaf JH, den Dekker WK, van Dalen BM, et al. First experience in humans using adipose tissue-derived regenerative cells in the treatment of patients with ST-segment elevation myocardial infarction. *Journal of the American College of Cardiology* 2012;59:539-40.
46. Perin EC, Sanz-Ruiz R, Sanchez PL, et al. Adipose-derived regenerative cells in patients with ischemic cardiomyopathy: The PRECISE Trial. *American heart journal* 2014;168:88-95 e2.
47. Hida N, Nishiyama N, Miyoshi S, et al. Novel cardiac precursor-like cells from human menstrual blood-derived mesenchymal cells. *Stem cells* 2008;26:1695-704.
48. Bockeria L, Bogin V, Bockeria O, et al. Endometrial regenerative cells for treatment of heart failure: a new stem cell enters the clinic. *Journal of translational medicine* 2013;11:56.
49. Bearzi C, Rota M, Hosoda T, et al. Human cardiac stem cells. *Proceedings of the National Academy of Sciences of the United States of America* 2007;104:14068-73.
50. Hosoda T. C-kit-positive cardiac stem cells and myocardial regeneration. *American journal of cardiovascular disease* 2012;2:58-67.
51. Lee ST, White AJ, Matsushita S, et al. Intramyocardial injection of autologous cardiospheres or cardiosphere-derived cells preserves function and minimizes adverse ventricular remodeling in pigs with heart failure post-myocardial infarction. *Journal of the American College of Cardiology* 2011;57:455-65.
52. Brunskill SJ, Hyde CJ, Doree CJ, Watt SM, Martin-Rendon E. Route of delivery and baseline left ventricular ejection fraction, key factors of bone-marrow-derived cell therapy for ischaemic heart disease. *European journal of heart failure* 2009;11:887-96.
53. Wollert KC, Meyer GP, Lotz J, et al. Intracoronary autologous bone-marrow cell transfer after myocardial infarction: the BOOST randomised controlled clinical trial. *Lancet* 2004;364:141-8.
54. Assmus B, Rolf A, Erbs S, et al. Clinical outcome 2 years after intracoronary administration of bone marrow-derived progenitor cells in acute myocardial infarction. *Circulation Heart failure* 2010;3:89-96.
55. Ge J, Li Y, Qian J, et al. Efficacy of emergent transcatheter transplantation of stem cells for treatment of acute myocardial infarction (TCT-STAMI). *Heart* 2006;92:1764-7.
56. Lunde K, Solheim S, Aakhus S, et al. Intracoronary injection of mononuclear bone marrow cells in acute myocardial infarction. *The New England journal of medicine* 2006;355:1199-209.
57. Huikuri HV, Kervinen K, Niemela M, et al. Effects of intracoronary injection of mononuclear bone marrow cells on left ventricular function, arrhythmia risk profile, and restenosis after thrombolytic therapy of acute myocardial infarction. *European heart journal* 2008;29:2723-32.
58. Diederichsen AC, Moller JE, Thayssen P, et al. Effect of repeated intracoronary injection of bone marrow cells in patients with ischaemic heart failure the Danish stem cell study--congestive heart failure trial (DanCell-CHF). *European journal of heart failure* 2008;10:661-7.

59. Roncalli J, Mouquet F, Piot C, et al. Intracoronary autologous mononucleated bone marrow cell infusion for acute myocardial infarction: results of the randomized multicenter BONAMI trial. *European heart journal* 2011;32:1748-57.
60. Assmus B, Walter DH, Seeger FH, et al. Effect of shock wave-facilitated intracoronary cell therapy on LVEF in patients with chronic heart failure: the CELLWAVE randomized clinical trial. *Jama* 2013;309:1622-31.
61. Hirsch A, Nijveldt R, van der Vleuten PA, et al. Intracoronary infusion of mononuclear cells from bone marrow or peripheral blood compared with standard therapy in patients after acute myocardial infarction treated by primary percutaneous coronary intervention: results of the randomized controlled HEBE trial. *European heart journal* 2011;32:1736-47.
62. Traverse JH, Henry TD, Ellis SG, et al. Effect of intracoronary delivery of autologous bone marrow mononuclear cells 2 to 3 weeks following acute myocardial infarction on left ventricular function: the LateTIME randomized trial. *Jama* 2011;306:2110-9.
63. Gyongyosi M, Lang I, Dettke M, et al. Combined delivery approach of bone marrow mononuclear stem cells early and late after myocardial infarction: the MYSTAR prospective, randomized study. *Nature clinical practice Cardiovascular medicine* 2009;6:70-81.
64. Tse HF, Thambar S, Kwong YL, et al. Prospective randomized trial of direct endomyocardial implantation of bone marrow cells for treatment of severe coronary artery diseases (PROTECT-CAD trial). *European heart journal* 2007;28:2998-3005.
65. Mansour S, Roy DC, Bouchard V, et al. One-Year Safety Analysis of the COMPARE-AMI Trial: Comparison of Intracoronary Injection of CD133 Bone Marrow Stem Cells to Placebo in Patients after Acute Myocardial Infarction and Left Ventricular Dysfunction. *Bone marrow research* 2011;2011:385124.
66. Chen SL, Fang WW, Ye F, et al. Effect on left ventricular function of intracoronary transplantation of autologous bone marrow mesenchymal stem cell in patients with acute myocardial infarction. *The American journal of cardiology* 2004;94:92-5.
67. Losordo DW, Schatz RA, White CJ, et al. Intramyocardial transplantation of autologous CD34+ stem cells for intractable angina: a phase I/IIa double-blind, randomized controlled trial. *Circulation* 2007;115:3165-72.
68. Gyongyosi M, Hemetsberger R, Wolbank S, et al. Imaging the migration of therapeutically delivered cardiac stem cells. *JACC Cardiovascular imaging* 2010;3:772-5.
69. Wang S, Cui J, Peng W, Lu M. Intracoronary autologous CD34+ stem cell therapy for intractable angina. *Cardiology* 2010;117:140-7.
70. Zohnhofer D, Dibra A, Koppa T, et al. Stem cell mobilization by granulocyte colony-stimulating factor for myocardial recovery after acute myocardial infarction: a meta-analysis. *Journal of the American College of Cardiology* 2008;51:1429-37.
71. Ripa RS, Jorgensen E, Wang Y, et al. Stem cell mobilization induced by subcutaneous granulocyte-colony stimulating factor to improve cardiac regeneration after acute ST-elevation myocardial infarction: result of the double-blind, randomized, placebo-controlled stem cells in myocardial infarction (STEMMI) trial. *Circulation* 2006;113:1983-92.
72. Kajstura J, Rota M, Whang B, et al. Bone marrow cells differentiate in cardiac cell lineages after infarction independently of cell fusion. *Circulation research* 2005;96:127-37.
73. Zohnhofer D, Ott I, Mehilli J, et al. Stem cell mobilization by granulocyte colony-stimulating factor in patients with acute myocardial infarction: a randomized controlled trial. *Jama* 2006;295:1003-10.
74. Bui QT, Gertz ZM, Wilensky RL. Intracoronary delivery of bone-marrow-derived stem cells. *Stem cell research & therapy* 2010;1:29.
75. Malliaras K, Marban E. Cardiac cell therapy: where we've been, where we are, and where we should be headed. *British medical bulletin* 2011;98:161-85.
76. Nygren JM, Jovinge S, Breitbart M, et al. Bone marrow-derived hematopoietic cells generate cardiomyocytes at a low frequency through cell fusion, but not transdifferentiation. *Nature medicine* 2004;10:494-501.
77. Terada N, Hamazaki T, Oka M, et al. Bone marrow cells adopt the phenotype of other cells by spontaneous cell fusion. *Nature* 2002;416:542-5.

78. Engelmann MG, Theiss HD, Hennig-Theiss C, et al. Autologous bone marrow stem cell mobilization induced by granulocyte colony-stimulating factor after subacute ST-segment elevation myocardial infarction undergoing late revascularization: final results from the G-CSF-STEMI (Granulocyte Colony-Stimulating Factor ST-Segment Elevation Myocardial Infarction) trial. *Journal of the American College of Cardiology* 2006;48:1712-21.
79. Leone AM, Galiuto L, Garramone B, et al. Usefulness of granulocyte colony-stimulating factor in patients with a large anterior wall acute myocardial infarction to prevent left ventricular remodeling (the rigenera study). *The American journal of cardiology* 2007;100:397-403.
80. Stamm C, Westphal B, Kleine HD, et al. Autologous bone-marrow stem-cell transplantation for myocardial regeneration. *Lancet* 2003;361:45-6.
81. Menasche P, Hagege AA, Vilquin JT, et al. Autologous skeletal myoblast transplantation for severe postinfarction left ventricular dysfunction. *Journal of the American College of Cardiology* 2003;41:1078-83.
82. Siminiak T, Kalawski R, Fiszer D, et al. Autologous skeletal myoblast transplantation for the treatment of postinfarction myocardial injury: phase I clinical study with 12 months of follow-up. *American heart journal* 2004;148:531-7.
83. Dib N, McCarthy P, Campbell A, et al. Feasibility and safety of autologous myoblast transplantation in patients with ischemic cardiomyopathy. *Cell transplantation* 2005;14:11-9.
84. Francis DP, Mielewczik M, Zargaran D, Cole GD. Autologous bone marrow-derived stem cell therapy in heart disease: discrepancies and contradictions. *International journal of cardiology* 2013;168:3381-403.
85. Jeevanantham V, Butler M, Saad A, Abdel-Latif A, Zuba-Surma EK, Dawn B. Adult bone marrow cell therapy improves survival and induces long-term improvement in cardiac parameters: a systematic review and meta-analysis. *Circulation* 2012;126:551-68.
86. Nowbar AN, Mielewczik M, Karavassilis M, et al. Discrepancies in autologous bone marrow stem cell trials and enhancement of ejection fraction (DAMASCENE): weighted regression and meta-analysis. *Bmj* 2014;348:g2688.
87. Lipinski MJ, Biondi-Zoccai GG, Abbate A, et al. Impact of intracoronary cell therapy on left ventricular function in the setting of acute myocardial infarction: a collaborative systematic review and meta-analysis of controlled clinical trials. *Journal of the American College of Cardiology* 2007;50:1761-7.
88. Wen Y, Meng L, Ding Y, Ouyang J. Autologous transplantation of blood-derived stem/progenitor cells for ischaemic heart disease. *International journal of clinical practice* 2011;65:858-65.
89. Reffelmann T, Kloner RA. Intracoronary blood- or bone marrow-derived cell transplantation in patients with ischemic heart disease. *Regenerative medicine* 2009;4:709-19.
90. de Jong R, Houtgraaf JH, Samiei S, Boersma E, Duckers HJ. Intracoronary stem cell infusion after acute myocardial infarction: a meta-analysis and update on clinical trials. *Circulation Cardiovascular interventions* 2014;7:156-67.
91. Gyongyosi M, Wojakowski W, Lemarchand P, et al. Meta-Analysis of Cell-based CaRdiac stUdiEs (ACCRUE) in patients with acute myocardial infarction based on individual patient data. *Circulation research* 2015;116:1346-60.
92. Kovacic JC, Fuster V. Cell therapy for patients with acute myocardial infarction: ACCRUed evidence to date. *Circulation research* 2015;116:1287-90.
93. Behfar A, Terzic A. Derivation of a cardiopoietic population from human mesenchymal stem cells yields cardiac progeny. *Nature clinical practice Cardiovascular medicine* 2006;3 Suppl 1:S78-82.
94. Gupta MK, Walthall JM, Venkataraman R, et al. Combinatorial polymer electrospun matrices promote physiologically-relevant cardiomyogenic stem cell differentiation. *PloS one* 2011;6:e28935.
95. Venugopal JR, Prabhakaran MP, Mukherjee S, Ravichandran R, Dan K, Ramakrishna S. Biomaterial strategies for alleviation of myocardial infarction. *Journal of the Royal Society, Interface / the Royal Society* 2012;9:1-19.

96. Seif-Naraghi SB, Salvatore MA, Schup-Magoffin PJ, Hu DP, Christman KL. Design and characterization of an injectable pericardial matrix gel: a potentially autologous scaffold for cardiac tissue engineering. *Tissue engineering Part A* 2010;16:2017-27.
97. Green EM, Lee RT. Proteins and small molecules for cellular regenerative medicine. *Physiological reviews* 2013;93:311-25.
98. Silvestre JS, Menasche P. The Evolution of the Stem Cell Theory for Heart Failure. *EBioMedicine* 2015;2:1871-9.
99. Gnecchi M, He H, Liang OD, et al. Paracrine action accounts for marked protection of ischemic heart by Akt-modified mesenchymal stem cells. *Nature medicine* 2005;11:367-8.
100. Gallina C, Turinetto V, Giachino C. A New Paradigm in Cardiac Regeneration: The Mesenchymal Stem Cell Secretome. *Stem cells international* 2015;2015:765846.
101. Hodgkinson CP, Bareja A, Gomez JA, Dzau VJ. Emerging Concepts in Paracrine Mechanisms in Regenerative Cardiovascular Medicine and Biology. *Circulation research* 2016;118:95-107.
102. Gnecchi M, He H, Noiseux N, et al. Evidence supporting paracrine hypothesis for Akt-modified mesenchymal stem cell-mediated cardiac protection and functional improvement. *FASEB journal : official publication of the Federation of American Societies for Experimental Biology* 2006;20:661-9.
103. Takahashi M, Li TS, Suzuki R, et al. Cytokines produced by bone marrow cells can contribute to functional improvement of the infarcted heart by protecting cardiomyocytes from ischemic injury. *American journal of physiology Heart and circulatory physiology* 2006;291:H886-93.
104. Ohnishi S, Yanagawa B, Tanaka K, et al. Transplantation of mesenchymal stem cells attenuates myocardial injury and dysfunction in a rat model of acute myocarditis. *Journal of molecular and cellular cardiology* 2007;42:88-97.
105. Baraniak PR, McDevitt TC. Stem cell paracrine actions and tissue regeneration. *Regenerative medicine* 2010;5:121-43.
106. Djouad F, Charbonnier LM, Bouffi C, et al. Mesenchymal stem cells inhibit the differentiation of dendritic cells through an interleukin-6-dependent mechanism. *Stem cells* 2007;25:2025-32.
107. Spaggiari GM, Abdelrazik H, Becchetti F, Moretta L. MSCs inhibit monocyte-derived DC maturation and function by selectively interfering with the generation of immature DCs: central role of MSC-derived prostaglandin E2. *Blood* 2009;113:6576-83.
108. Ortiz LA, Dutreil M, Fattman C, et al. Interleukin 1 receptor antagonist mediates the antiinflammatory and antifibrotic effect of mesenchymal stem cells during lung injury. *Proceedings of the National Academy of Sciences of the United States of America* 2007;104:11002-7.
109. Zhang QZ, Su WR, Shi SH, et al. Human gingiva-derived mesenchymal stem cells elicit polarization of m2 macrophages and enhance cutaneous wound healing. *Stem cells* 2010;28:1856-68.
110. Kim J, Hematti P. Mesenchymal stem cell-educated macrophages: a novel type of alternatively activated macrophages. *Experimental hematology* 2009;37:1445-53.
111. Dayan V, Yannarelli G, Billia F, et al. Mesenchymal stromal cells mediate a switch to alternatively activated monocytes/macrophages after acute myocardial infarction. *Basic research in cardiology* 2011;106:1299-310.
112. Santini MP, Tsao L, Monassier L, et al. Enhancing repair of the mammalian heart. *Circulation research* 2007;100:1732-40.
113. Burchfield JS, Iwasaki M, Koyanagi M, et al. Interleukin-10 from transplanted bone marrow mononuclear cells contributes to cardiac protection after myocardial infarction. *Circulation research* 2008;103:203-11.
114. Kardami E, Banerji S, Doble BW, et al. PKC-dependent phosphorylation may regulate the ability of connexin43 to inhibit DNA synthesis. *Cell communication & adhesion* 2003;10:293-7.
115. Hinrichsen R, Haunso S, Busk PK. Different regulation of p27 and Akt during cardiomyocyte proliferation and hypertrophy. *Growth factors* 2007;25:132-40.

116. Zhao YY, Sawyer DR, Baliga RR, et al. Neuregulins promote survival and growth of cardiac myocytes. Persistence of ErbB2 and ErbB4 expression in neonatal and adult ventricular myocytes. *The Journal of biological chemistry* 1998;273:10261-9.
117. Bersell K, Arab S, Haring B, Kuhn B. Neuregulin1/ErbB4 signaling induces cardiomyocyte proliferation and repair of heart injury. *Cell* 2009;138:257-70.
118. Ohnishi S, Yasuda T, Kitamura S, Nagaya N. Effect of hypoxia on gene expression of bone marrow-derived mesenchymal stem cells and mononuclear cells. *Stem cells* 2007;25:1166-77.
119. Xu X, Xu Z, Xu Y, Cui G. Effects of mesenchymal stem cell transplantation on extracellular matrix after myocardial infarction in rats. *Coronary artery disease* 2005;16:245-55.
120. Stanley WC, Recchia FA, Lopaschuk GD. Myocardial substrate metabolism in the normal and failing heart. *Physiological reviews* 2005;85:1093-129.
121. Gneccchi M, He H, Melo LG, et al. Early beneficial effects of bone marrow-derived mesenchymal stem cells overexpressing Akt on cardiac metabolism after myocardial infarction. *Stem cells* 2009;27:971-9.
122. Nagaya N, Fujii T, Iwase T, et al. Intravenous administration of mesenchymal stem cells improves cardiac function in rats with acute myocardial infarction through angiogenesis and myogenesis. *American journal of physiology Heart and circulatory physiology* 2004;287:H2670-6.
123. Kinnaird T, Stabile E, Burnett MS, et al. Local delivery of marrow-derived stromal cells augments collateral perfusion through paracrine mechanisms. *Circulation* 2004;109:1543-9.
124. Kamihata H, Matsubara H, Nishiue T, et al. Implantation of bone marrow mononuclear cells into ischemic myocardium enhances collateral perfusion and regional function via side supply of angioblasts, angiogenic ligands, and cytokines. *Circulation* 2001;104:1046-52.
125. Dzau VJ, Gneccchi M, Pachori AS, Morello F, Melo LG. Therapeutic potential of endothelial progenitor cells in cardiovascular diseases. *Hypertension* 2005;46:7-18.
126. Markel TA, Wang Y, Herrmann JL, et al. VEGF is critical for stem cell-mediated cardioprotection and a crucial paracrine factor for defining the age threshold in adult and neonatal stem cell function. *American journal of physiology Heart and circulatory physiology* 2008;295:H2308-14.
127. Bolli R, Chugh AR, D'Amario D, et al. Cardiac stem cells in patients with ischaemic cardiomyopathy (SCIPIO): initial results of a randomised phase 1 trial. *Lancet* 2011;378:1847-57.
128. Chugh AR, Beache GM, Loughran JH, et al. Administration of cardiac stem cells in patients with ischemic cardiomyopathy: the SCIPIO trial: surgical aspects and interim analysis of myocardial function and viability by magnetic resonance. *Circulation* 2012;126:S54-64.
129. Mourkioti F, Rosenthal N. IGF-1, inflammation and stem cells: interactions during muscle regeneration. *Trends in immunology* 2005;26:535-42.
130. Engels MC, Rajarajan K, Feistritz R, et al. Insulin-like growth factor promotes cardiac lineage induction in vitro by selective expansion of early mesoderm. *Stem cells* 2014;32:1493-502.
131. Nakanishi C, Yamagishi M, Yamahara K, et al. Activation of cardiac progenitor cells through paracrine effects of mesenchymal stem cells. *Biochemical and biophysical research communications* 2008;374:11-6.
132. Wen Z, Zheng S, Zhou C, Yuan W, Wang J, Wang T. Bone marrow mesenchymal stem cells for post-myocardial infarction cardiac repair: microRNAs as novel regulators. *Journal of cellular and molecular medicine* 2012;16:657-71.
133. Scalbert E, Bril A. Implication of microRNAs in the cardiovascular system. *Current opinion in pharmacology* 2008;8:181-8.
134. Fasanaro P, Greco S, Ivan M, Capogrossi MC, Martelli F. microRNA: emerging therapeutic targets in acute ischemic diseases. *Pharmacology & therapeutics* 2010;125:92-104.
135. Ohtani K, Dimmeler S. Control of cardiovascular differentiation by microRNAs. *Basic research in cardiology* 2011;106:5-11.
136. Meder B, Keller A, Vogel B, et al. MicroRNA signatures in total peripheral blood as novel biomarkers for acute myocardial infarction. *Basic research in cardiology* 2011;106:13-23.

137. Bostjancic E, Zidar N, Glavac D. MicroRNA microarray expression profiling in human myocardial infarction. *Disease markers* 2009;27:255-68.
138. Greco S, Gorospe M, Martelli F. Noncoding RNA in age-related cardiovascular diseases. *Journal of molecular and cellular cardiology* 2015;83:142-55.
139. Barile L, Lionetti V, Cervio E, et al. Extracellular vesicles from human cardiac progenitor cells inhibit cardiomyocyte apoptosis and improve cardiac function after myocardial infarction. *Cardiovascular research* 2014;103:530-41.
140. Segers VF, Tokunou T, Higgins LJ, MacGillivray C, Gannon J, Lee RT. Local delivery of protease-resistant stromal cell derived factor-1 for stem cell recruitment after myocardial infarction. *Circulation* 2007;116:1683-92.
141. Lui KO, Zangi L, Chien KR. Cardiovascular regenerative therapeutics via synthetic paracrine factor modified mRNA. *Stem cell research* 2014;13:693-704.
142. Vunjak-Novakovic G, Lui KO, Tandon N, Chien KR. Bioengineering heart muscle: a paradigm for regenerative medicine. *Annual review of biomedical engineering* 2011;13:245-67.
143. Gojo S, Kyo S. Cardiac regenerative medicine: cellular therapy and tissue engineering. *Circulation journal : official journal of the Japanese Circulation Society* 2009;73 Suppl A:A61-7.
144. Jawad H, Lyon AR, Harding SE, Ali NN, Boccaccini AR. Myocardial tissue engineering. *British medical bulletin* 2008;87:31-47.
145. Segers VF, Van Riet I, Andries LJ, et al. Mesenchymal stem cell adhesion to cardiac microvascular endothelium: activators and mechanisms. *American journal of physiology Heart and circulatory physiology* 2006;290:H1370-7.
146. Thum T, Bauersachs J, Poole-Wilson PA, Volk HD, Anker SD. The dying stem cell hypothesis: immune modulation as a novel mechanism for progenitor cell therapy in cardiac muscle. *Journal of the American College of Cardiology* 2005;46:1799-802.
147. von Harsdorf R, Poole-Wilson PA, Dietz R. Regenerative capacity of the myocardium: implications for treatment of heart failure. *Lancet* 2004;363:1306-13.
148. Geng YJ. Molecular mechanisms for cardiovascular stem cell apoptosis and growth in the hearts with atherosclerotic coronary disease and ischemic heart failure. *Annals of the New York Academy of Sciences* 2003;1010:687-97.
149. Frangogiannis NG. The inflammatory response in myocardial injury, repair, and remodelling. *Nature reviews Cardiology* 2014;11:255-65.
150. Gnecci M, Zhang Z, Ni A, Dzau VJ. Paracrine mechanisms in adult stem cell signaling and therapy. *Circulation research* 2008;103:1204-19.
151. Haider T, Hoftberger R, Ruger B, et al. The secretome of apoptotic human peripheral blood mononuclear cells attenuates secondary damage following spinal cord injury in rats. *Experimental neurology* 2015;267:230-42.
152. Altmann P, Mildner M, Haider T, et al. Secretomes of apoptotic mononuclear cells ameliorate neurological damage in rats with focal ischemia. *F1000Research* 2014;3:131.
153. Kober J, Gugerell A, Schmid M, et al. Wound Healing Effect of Conditioned Media Obtained From Adipose Tissue on Human Skin Cells: A Comparative in Vitro Study. *Annals of plastic surgery* 2014.
154. Mildner M, Hacker S, Haider T, et al. Secretome of peripheral blood mononuclear cells enhances wound healing. *PloS one* 2013;8:e60103.
155. Hoetzenecker K, Zimmermann M, Hoetzenecker W, et al. Mononuclear cell secretome protects from experimental autoimmune myocarditis. *European heart journal* 2015;36:676-85.
156. Hoetzenecker K, Assinger A, Lichtenauer M, et al. Secretome of apoptotic peripheral blood cells (APOSEC) attenuates microvascular obstruction in a porcine closed chest reperfused acute myocardial infarction model: role of platelet aggregation and vasodilation. *Basic research in cardiology* 2012;107:292.
157. Lichtenauer M, Mildner M, Hoetzenecker K, et al. Secretome of apoptotic peripheral blood cells (APOSEC) confers cytoprotection to cardiomyocytes and inhibits tissue remodelling after acute myocardial infarction: a preclinical study. *Basic research in cardiology* 2011;106:1283-97.
158. Lichtenauer M, Mildner M, Baumgartner A, et al. Intravenous and intramyocardial injection of apoptotic white blood cell suspensions prevents ventricular remodelling by

increasing elastin expression in cardiac scar tissue after myocardial infarction. *Basic research in cardiology* 2011;106:645-55.

159. Ankersmit HJ, Hoetzenecker K, Dietl W, et al. Irradiated cultured apoptotic peripheral blood mononuclear cells regenerate infarcted myocardium. *European journal of clinical investigation* 2009;39:445-56.

160. Beer L, Seemann R, Ristl R, et al. High dose ionizing radiation regulates micro RNA and gene expression changes in human peripheral blood mononuclear cells. *BMC genomics* 2014;15:814.

161. Beer L, Zimmermann M, Mitterbauer A, et al. Analysis of the Secretome of Apoptotic Peripheral Blood Mononuclear Cells: Impact of Released Proteins and Exosomes for Tissue Regeneration. *Scientific reports* 2015;5:16662.

162. Heiberg E, Sjogren J, Ugander M, Carlsson M, Engblom H, Arheden H. Design and validation of Segment--freely available software for cardiovascular image analysis. *BMC medical imaging* 2010;10:1.

163. Wijnmaalen AP, van der Geest RJ, van Huls van Taxis CF, et al. Head-to-head comparison of contrast-enhanced magnetic resonance imaging and electroanatomical voltage mapping to assess post-infarct scar characteristics in patients with ventricular tachycardias: real-time image integration and reversed registration. *European heart journal* 2011;32:104-14.

164. Wolf T, Gepstein L, Dror U, et al. Detailed endocardial mapping accurately predicts the transmural extent of myocardial infarction. *Journal of the American College of Cardiology* 2001;37:1590-7.

165. Gyongyosi M, Dib N. Diagnostic and prognostic value of 3D NOGA mapping in ischemic heart disease. *Nature reviews Cardiology* 2011;8:393-404.

166. Tokuda M, Tedrow UB, Inada K, et al. Direct comparison of adjacent endocardial and epicardial electrograms: implications for substrate mapping. *Journal of the American Heart Association* 2013;2:e000215.

167. Huang da W, Sherman BT, Lempicki RA. Systematic and integrative analysis of large gene lists using DAVID bioinformatics resources. *Nature protocols* 2009;4:44-57.

168. Ranganath SH, Levy O, Inamdar MS, Karp JM. Harnessing the mesenchymal stem cell secretome for the treatment of cardiovascular disease. *Cell stem cell* 2012;10:244-58.

169. Ertel A, Tozeren A. Human and mouse switch-like genes share common transcriptional regulatory mechanisms for bimodality. *BMC genomics* 2008;9:628.

170. Jin H, Yang R, Awad TA, et al. Effects of early angiotensin-converting enzyme inhibition on cardiac gene expression after acute myocardial infarction. *Circulation* 2001;103:736-42.

171. Sehl PD, Tai JT, Hillan KJ, et al. Application of cDNA microarrays in determining molecular phenotype in cardiac growth, development, and response to injury. *Circulation* 2000;101:1990-9.

172. Stanton LW, Garrard LJ, Damm D, et al. Altered patterns of gene expression in response to myocardial infarction. *Circulation research* 2000;86:939-45.

173. Song GY, Wu YJ, Yang YJ, et al. The accelerated post-infarction progression of cardiac remodelling is associated with genetic changes in an untreated streptozotocin-induced diabetic rat model. *European journal of heart failure* 2009;11:911-21.

174. Prat-Vidal C, Galvez-Monton C, Nonell L, et al. Identification of temporal and region-specific myocardial gene expression patterns in response to infarction in swine. *PloS one* 2013;8:e54785.

175. Roy S, Khanna S, Kuhn DE, et al. Transcriptome analysis of the ischemia-reperfused remodeling myocardium: temporal changes in inflammation and extracellular matrix. *Physiological genomics* 2006;25:364-74.

176. Jameel MN, Li Q, Mansoor A, et al. Long-term functional improvement and gene expression changes after bone marrow-derived multipotent progenitor cell transplantation in myocardial infarction. *American journal of physiology Heart and circulatory physiology* 2010;298:H1348-56.

177. Gyongyosi M, Khorsand A, Sochor H, et al. Characterization of hibernating myocardium with NOGA electroanatomic endocardial mapping. *The American journal of cardiology* 2005;95:722-8.

178. Amado LC, Gerber BL, Gupta SN, et al. Accurate and objective infarct sizing by contrast-enhanced magnetic resonance imaging in a canine myocardial infarction model. *Journal of the American College of Cardiology* 2004;44:2383-9.